ROCK PROPERTIES, SEISMIC MODELING, AND 3C SEISMIC ANALYSIS IN THE BAKKEN SHALE, NORTH DAKOTA

_____

A Thesis Presented to

The Faculty of the Department of Earth and Atmospheric Sciences

University of Houston

_____

In Partial Fulfillment

of the Requirements for the Degree

Master of Science

_____

By

Andrea Gloreinaldy Paris Castellano

August 2017

ROCK PROPERTIES, SEISMIC MODELING, AND 3C SEISMIC ANALYSIS IN THE BAKKEN SHALE, NORTH DAKOTA

_____

Andrea Gloreinaldy Paris Castellano

APPROVED:

_____

Dr. Robert R. Stewart, Chairman
Dept. of Earth and Atmospheric Sciences

_____

Dr. John P. Castagna
Dept. of Earth and Atmospheric Sciences

_____

Dr. Richard Verm
Geokinetics Inc.

_____

Dean, College of Natural Sciences and Mathematics

ROCK PROPERTIES, SEISMIC MODELING, AND 3C SEISMIC ANALYSIS IN THE BAKKEN SHALE, NORTH DAKOTA

An Abstract of a Thesis

Presented to

The Faculty of the Department of Earth and Atmospheric Sciences

University of Houston

In Partial Fulfillment

of the Requirements for the Degree

Master of Science

By

Andrea Gloreinaldy Paris Castellano

August 2017

Abstract

A solid understanding of the factors that affect the seismic velocity and the amplitude variation with offset (AVO) is imperative for a reliable interpretation of seismic data and related prospect de-risking. To understand the relationship between rock properties and their elastic response (i.e. velocity and density), petrophysical properties, rock-physics, seismic modeling, and fluid substitution are analyzed. Seismic inversions and statistical predictions of rock properties are integrated to delimit prospective intervals and areas with high total organic carbon (TOC) content within the Bakken Formation, North Dakota. The shale intervals can be recognized by cross-plotting well logs velocities versus density. The hydrocarbon potential is observed on logs as low densities, high gamma-ray response, low P and S-wave velocities, and high neutron porosities. Organic-rich intervals with TOC content higher than 10 wt. % deviate from the ones that have lower TOC in the density domain, and exhibit slightly lower velocities, lower densities (< 2.3 g/cc), and a generally higher shale content (> 40%). Within the study area, Well V-1 shows the highest TOC content, especially at the Upper Bakken depths with approximately 50% of clay volume. TOC is considered to be the principal factor affecting changes in density and P and S-wave velocities in the Bakken shales. Vp/Vs ranges between 1.65 and 1.75. Synthetic seismic data are generated using the anisotropic version of Zoeppritz equations including estimated Thomsen parameters. For the tops of Upper

and Lower Bakken, the amplitude becomes less negative with offset showing a negative intercept and a positive gradient which correspond to an AVO Class IV. A comparison between PP and PP-PS joint inversions shows that the P-impedance error decreases by 14% when incorporating the converted-wave information in the inversion process. A statistical approach using multi-attribute analysis and neural networks allows to delimit the zones of interest in terms of P-impedance, density, TOC content, and brittleness. The inverted and predicted results show fair correlations with the original well logs. The integration between well-log analysis, rock-physics, seismic modeling, constrained inversions and statistical predictions contribute in identifying the vertical distribution of good reservoir quality areas within the Bakken Formation.

Contents

Abstract **iv**

Contents **vi**

List of Figures **ix**

List of Tables **xxi**

1. Introduction **1**

1.1. The problem……..2

1.2. Objectives……..3

1.3. Anisotropy in shales……....4

1.4. Anisotropy in AVO modeling……5

1.5. Bakken Shale……..……..…….7

1.5.1. Geological background…..……..…… 10

1.5.2. The Bakken Formation……..13

1.6. Dataset overview…..…….16

1.6.1. Software……...……...17

2. Well-log analysis and petrophysical properties 21

2.1. Shale volume estimation……...24

2.2. TOC estimation…….. 31

2.3. Cross-plot analysis……43

2.4. Brittleness estimation…… 55

3. AVO seismic modeling and fluid substitution 62

3.1. Interval properties from log data…….63

3.2. AVO seismic modeling……..74

3.3. Fluid substitution……...81

4. Seismic inversion 87

4.1. PP seismic interpretation……..90

4.1.1. Well-to-seismic tie and seismic resolution……90

4.2. Post-stack inversion…….....95

4.2.1. Initial models...……..98

4.2.2. Inversion analysis……103

4.3. PP-PS post-stack joint inversion……..…110

4.3.1. PP and PS joint interpretation……112

4.3.2. PP-PS registration……... 115

4.3.3. Low-frequency models and joint inversion analysis……...…119

4.4. Statistical estimation of inverted properties……..134

4.5. Identification of high-TOC and brittle zones within the Bakken Formation...….143

5. Conclusions, recommendations, and future work 154

5.1. Recommendations and future work……...…159

References 161

List of Figures

Figure 1.1: Comparison between oil production (above) and new-well oil production per rig (below) of different shale oil plays in the U.S. from July 2016 to July 2017. (EIA Drilling Productivity Report, June 2017). 8

Figure 1.2: Map showing the Williston Basin Province, Bakken Total Petroleum System (TPS), and the Bakken Formation Assessment Units (AUs). Major structural features are also shown. Inset map shows the location of the Bakken TPS. (Modified from Du, 2015). 11

Figure 1.3: Stratigraphic column of the Williston Basin showing formations and major sequences. The red rectangle indicates the three main formations for this study. (Modified from KED Interests LLC, 2017). 12

Figure 1.4: Gamma Ray, density, compressional and shear-wave velocities and Thomsen's weak anisotropy parameters logs from the Bakken Petroleum System (Mississippian Lodgepole Formation, the Devonian-Mississippian Bakken Formation, and the Devonian Three Forks Formation. 14

Figure 1.5: Processing workflows used for the generation of the PP and PS seismic data. 16

Figure 1.6: Comparison between the PP and PS stacked sections in their native times. The yellow polygon encloses the target interval: around 1,700 ms (PP time) and around 3,200 ms (PS time). 18

Figure 1.7: Base map showing the location of the wells available. 652 CDP. Coordinates are not plotted due to confidentiality. 19

Figure 1.8: Base map showing the location of the vertical well in the vicinity of the 2D line of the Red Sky 2D-3C survey. 652 CDP. Coordinates are not plotted due to confidentiality. 20

Figure 2.1: Bakken Formation isopach map showing thickness changes within the Bakken. The thickness of the Bakken Formation in the study area decreases toward the approximate location of the 2D seismic survey (black rectangle), from west to east. Coordinates are not plotted due to confidentiality. (Modified from Crews, 2015). 24

Figure 2.2: GR vs. Corrected Spectral GR for Well B, color-coded by formation. The correlation between both GR responses allows an adequate linear fit of 0.981. The linear empirical relationship is used to calculate the corrected GR for uranium in the Well V-1. 26

Figure 2.3: Well V-1 logs. From left to right, total GR, the corrected GR for uranium and its normalized readings (thick black curve), neutron porosity and density, density porosity and the comparison between the estimated shale volumes ($VshGRn, VshNPHI, VshPHI$). Shale volumes calculated with the three methods follow the separation trend between NPHI and RHOZ except in the dolomitic Three Forks Formation. Since the high-density porosity reading in the Upper and Lower Bakken is due primarily to organic matter rather than porosity, values of shale volume in these two members are considered underestimated. $VshGRn$ and $VshNPHI$ are taken as better representations of the relative volume fraction of shales in the formation of interest. 30

Figure 2.4: Well V-1 logs. From left to right, total GR and the normalized corrected GR (GRn), neutron porosity and density, P-wave sonic, and the superposition of the deep resistivity and the GRn curves. The cross-over between resistivity and gamma-ray readings (in yellow) is indicative of high TOC content. 32

Figure 2.5: Estimation of the TOC from the Passey (1990) Method for the Well V-1. From left to right, total and normalized GR, deep resistivity, neutron porosity, P-wave sonic, density logs, and the comparison between their respective estimated values of TOC content. The inorganic Three Forks Formation was taken as the baseline for $\Delta logR$ calculation in Passey's formulation. Note how the curves approach to each other at the base of the Three Forks Formation in the second track. 35

Figure 2.6: Comparison between the TOC estimations at the well B and well V-1. From left to right (In the well B), total gamma-ray (GR), density (RHOZ), sonic porosity

(SPHI), and the comparison between the TOC curves from Vernik and Landis (1996), and Schmoker and Hester (1983). From left to right (In the well V-1), total and normalized GR, deep resistivity (AT90), neutron porosity (NPHI), P-wave sonic (DT) and density (RHOZ) logs, the comparison between the estimated values of TOC by the Passey (1990), Vernik and Landis (1996) and Schmoker and Hester (1983) methods, and the resistivity (AT90)-density (RHOZ) overlay for $\Delta logR$ calculation, where areas highlighted in purple correspond to high organic-matter zones. 39

Figure 2.7: Organic-carbon content (wt.%) of the upper member of Bakken Formation. Contour interval is 1.0%. The red rectangle shows the location of the wells B and V-1. Note the increase of TOC values in East direction inside the study area. Coordinates are not plotted due to confidentiality. (Modified from Schmoker and Hester, 1983). 41

Figure 2.8: Organic-carbon content (wt.%) of the lower member of Bakken Formation. Contour interval is 1.0%. The red rectangle shows the location of the wells B and V-1. Note the increase of TOC values in East direction inside the study area. Coordinates are not plotted due to confidentiality. (Modified from Schmoker and Hester, 1983). 42

Figure 2.9: Vs vs. (a) Vs_slow and (b) Vs_fast cross-plots for well A, B, C, and D, color-coded by formation. The correlation between Vs and both the Vs slow and fast components allows an adequate linear fit of 0.98. 44

Figure 2.10: Vp vs. Vs cross-plot for Well A, B, C, D, and Well V-1, color-coded by (a) formation and (b) GR. Note how both, Upper and Lower Bakken shales deviate from the Castagna's mudrock line (Castagna et al., 1985) towards lower velocities which can be caused by oil saturation and especially TOC content. The correlation between Vp and Vs allows an adequate linear fit of 0.957..... 46

Figure 2.11: Density vs. Vp cross-plot for Well A, B, C, D, and Well V-1, color-coded by (a) formation and (b) GR. Note how both, Upper and Lower Bakken organic-rich shales can be easily identified in the density domain with values lower than 2.5 g/cc. 47

Figure 2.12: Density vs. Vp cross-plots for the Bakken Formation, including the wells A, B, C, D, and V-1. Cross-plots are color-coded by (a) TOC from Schmoker and Hester (1983), (b) Vclay, (c) unit and (d) well. The high-TOC interval correlates to low densities, high velocities, and variable clay content. The "hot" Upper and Lower Bakken Shales units are enclosed in the gray and black polygons of high

TOC, respectively. Vp is a good lithological indicator for these two units, showing a general decrease in their values as clay content decreases. TOC seems to be the principal factor affecting changes in density and P-wave velocity in these wells. 49

Figure 2.13: Density vs. Vs cross-plots for the Bakken Formation, including the wells A, B, C, D, and V-1. Cross-plots are color-coded by (a) TOC from Schmoker and Hester (1983), (b) Vclay, (c) unit and (d) well. The high-TOC interval correlates to low densities, high velocities, and variable clay content. The "hot" Upper and Lower Bakken Shales units are enclosed in the gray and black polygons of high TOC, respectively. Vs is a good lithological indicator for these two units, showing a general decrease in their values as clay content decreases. TOC seems to be the principal factor affecting changes in density and S-wave velocity in these wells. 50

Figure 2.14: Density vs. Vp/Vs cross-plots for the Bakken Formation, including the wells A, B, C, D, and V-1. Cross-plots are color-coded by (a) TOC from Schmoker and Hester (1983) empirical method, (b) Vclay, (c) unit and (d) well. The high-TOC interval correlates to low densities and a Vp/Vs that ranges between 1.65 and 1.75. The "hot" Upper and Lower Bakken Shales units are enclosed in the gray and black polygons with TOC values higher than 14 wt.% and 10 wt.%, respectively. 52

Figure 2.15: Density vs. acoustic impedance (AI) cross-plots for the Bakken Formation, including the wells A, B, C, D, and V-1. Cross-plots are color-coded by (a) TOC from Schmoker and Hester (1983) empirical method, (b) Vshale, (c) unit and (d) well. The high-TOC interval correlates to low densities, high velocities and a high-clay content greater than 0.5. The "hot" Upper and Lower Bakken Shales units are enclosed in the gray and black polygons with TOC values higher than 14 wt.% and 10 wt.%, respectively. Acoustic impedance is also a good lithological indicator for these two units with a cutoff value of 20,000 g/cc*ft/s. 53

Figure 2.16: Acoustic impedance vs. Poisson's ratio (a), and $\lambda\rho$ vs. $\mu\rho$ (b) cross-plots of the Bakken Formation, colored by unit. Both "hot" Upper and Lower Bakken units (gray and black) cannot be easily discriminated in any of these domains. 55

Figure 2.17: Poisson's ratio vs. E (a), and Poisson's ratio vs. Eϱ (b) cross-plots of the Bakken Formation colored by unit. Notice the similarity between cluster points. A new domain $E\rho/\nu$ can be used as a brittleness indicator for the Bakken shale members. Brittle-shale zones and high-ductile zones in the red and blue

rectangles, respectively. The Lower Bakken is generally less brittle than the Upper Bakken and the Middle Bakken shows points with moderate brittleness. 58

Figure 2.18: Well section through Well B and Well V-1, showing a comparison between the brittleness indexes (fourth track) derived using Rickman's formulation (blue curve) and $E\rho/\nu$ (red curve). The fifth track shows the $E\rho$ calculation for reference. 59

Figure 2.19: Comparison between Well B and Well V-1 logs. From left to right, gamma-ray, uranium, mineral volumes (Shale in green, clay in brown, and quartz in yellow), density, TOC and total porosity, P and S-wave velocities, P and S-wave impedances, and Vp/Vs. Both the Upper and Lower Bakken show high clay content, high total porosities, and high TOC content. Upper Bakken has more brittle material content (e.g. quartz) than Lower Bakken and it could be more prone to open and maintain fractures during hydraulic fracturing. 61

Figure 3.1: Estimation of the saturation curves and set for Well V-1. From left to right, total and normalized GR colored by Vshale, density, deep resistivity, oil and water saturation, and the density porosity log colored by the initial fluid saturation. Water saturation (in blue), oil saturation (in green) and gas saturation (in red). 65

Figure 3.2: Vp vs. Vs cross-plots for Well V-1 color-coded by a) Upper and Lower Bakken members and b) middle Bakken member. The cross-plots are used to calibrate the Greenberg-Castagna relation for shales (green line) and sandstones (yellow line). 66

Figure 3.3: Vp vs. Vs cross-plots for Well V-1 color-coded by a) Lodgepole Formation and b) Three Forks Formation. The cross-plots are used to calibrate the Greenberg-Castagna polynomial and lineal regressions for limestones (blue line) and dolomites (purple line). 67

Figure 3.4: Estimation of δ and ε curves for Well A. From left to right, density, Vp and Vs, γ log provided by Hess Corporation, and the δ and ε logs estimated through Havens (2012) formulations. 72

Figure 3.5: PP pre-stack synthetic seismograms for Well A. From left to right, corrected and Backus-averaged density, Vp and Vs logs, calculated and modeled Thomsen's parameters logs, repeated synthetic traces at zero-offset, PP synthetic seismograms using the Vp log and its respective Backus average... 76

Figure 3.6: PS synthetic seismograms for Well A. From left to right, corrected and Backus-averaged density, Vp and Vs logs, calculated and modeled Thomsen's parameters logs, PS synthetic seismograms using the Vs log and its respective Backus average. 76

Figure 3.7: PP pre-stack synthetic seismograms for Well V-1. From left to right, corrected and Backus-averaged density Vp and Vs logs, VTI modeled Thomsen's parameters logs, repeated synthetic traces at zero-offset, PP synthetic seismograms using the Vp log and its respective Backus average. 77

Figure 3.8: PS synthetic seismograms for Well V-1. From left to right, corrected and Backus-averaged density Vp and Vs logs, VTI modeled Thomsen's parameters logs, PS synthetic seismograms using the Vs log and its respective Backus average. 77

Figure 3.9: PP AVA response for the top of the Upper Bakken. The negative intercept and positive gradient correspond to an AVO Class IV. 80

Figure 3.10: PP AVA response for the top of the Lower Bakken. The negative intercept and positive gradient correspond to an AVO Class IV. 80

Figure 3.11: Effect of the Middle Bakken fluid substitution of Well V-1. From left to right, the comparison of the Rho, Vp, Vs resulting from the five fluid substitution cases: 100% Oil, 100% gas, 100% brine. 83

Figure 3.12: Gassmann QC Sw vs. Vp, Vs plots for a) fluid substitution of oil, and b) fluid substitution of gas. Note how in both case scenarios, the higher the hydrocarbon saturation, the lower the Vp. Vs increases when substituting the reservoir with gas and remains constant in case of oil substitution. The density decreases proportionally to the hydrocarbon saturation. 84

Figure 3.13: Comparison between the in situ PP synthetic of well V-1 and all the fluid substitution cases. From left to right: Density, Vp and Vs logs and their corresponding fluid-substituted values, Thomsen's parameters logs and synthetic seismograms for the in situ, 100% brine, 100% gas, and 100% oil cases. 86

Figure 4.1: PP statistical wavelet extracted from the seismic and its corresponding frequency spectrum. The wavelet extraction is performed in a window from 1500 to 2000 ms (a 500 ms window length). The dotted shows a zero-phase angle. 91

Figure 4.2: PP full wavelet extracted from the seismic and its corresponding frequency spectrum. The wavelet extraction is performed in a window from 1500 to 2000 ms (a 500 ms window length). The dotted shows an average phase angle of 14 degrees. 93

Figure 4.3: Well-to-seismic tie of the well V-1. From left to right, tracks show density and P-wave velocity logs, zero-offset synthetic computed with statistical wavelet extracted from the seismic (blue traces), trace extracted from real seismic at the well location (red) and real PP seismic going through the well location with the interpreted horizons for the top of the Lodgepole, Bakken and Three Forks Formations. The correlation coefficient between the synthetic computed with the statistical wavelet and the seismic is 0.756 under the correlation window (yellow lines). 95

Figure 4.4: Model-based post-stack inversion workflow. Modified from the Hampson-Russell manual. 97

Figure 4.5: SW-NE sections of (a) P-impedance (Zp) and (b) S-impedance (Zs) models going through the Well V-1 location. The displayed curves are (a) P-wave velocity (b) S-impedance..... 99

Figure 4.6: SW-NE sections of (a) density and (b) Vp/Vs models going through the Well V-1 location. The displayed curves are (a) density (b) Vp/Vs. 100

Figure 4.7: SW-NE sections of (a) P-impedance (Zp) and (b) S-impedance (Zs) low-frequency models going through the Well V-1 location. The displayed curves are (a) P-wave velocity (b) S-impedance. 101

Figure 4.8: SW-NE sections of (a) density and (b) Vp/Vs low- frequency models going through the Well V-1 location. The displayed curves are (a) density (b) Vp/Vs. 102

Figure 4.9: PP post-stack inversion results for the interest intervals at the Well V-1 location using the low-frequency model. From left to right, tops from logs, inversion result (in red), filtered impedance log from the well (in blue), selected wavelet, synthetic traces calculated from the inversion result (red), original composite traces (black), repeated error trace (red) and picked horizons. There is a very good correlation between the inversion results and the trend of the original logs in the Bakken Formation..... 106

Figure 4.10: PP post-stack inversion results at the Well V-1 location. From left to right, inversion result (in red), filtered impedance log from the well (in blue), selected

wavelet, synthetic traces calculated from the inversion result (red), original composite traces (black), repeated error trace (red) and picked horizons. There is a very good correlation between the inversion results and the original logs. The Bakken members are resolved. 107

Figure 4.11: Difference between the PP seismic and the PP synthetic at the line going through the well location. Note that the amplitude of the traces is almost zero which indicates that the synthetic seismogram and the real seismic are almost identical (error trace equal to 0.208). 108

Figure 4.12: SW-NE inverted sections of (a) filtered P-impedance and (b) high-frequency P-impedance going through the Well V-1 location. The displayed log corresponds to the computed P-impedance log. 109

Figure 4.13: PP-PS joint inversion workflow. (Modified from Ruiz, 2016). 112

Figure 4.14: PP (green) and PS (blue) full wavelets and their corresponding frequency spectra. The PS frequency spectrum shows a higher peak frequency than the PP spectrum but the PP data show bigger bandwidth which translates into better seismic resolution. 113

Figure 4.15: PS data well-to-seismic tie for the well V-1. From left to right, tracks show tops from logs, density, P-wave and S-wave velocity logs, 20° incidence-angle synthetic seismogram computed with statistical wavelet extracted from the seismic (blue traces), trace extracted from real PS seismic at the well location (red) and real PS seismic going through the well location with the interpreted horizons for the top of the Lodgepole, Bakken and Three Forks Formations. The correlation coefficient between the synthetic and the seismic is 0.727 under the correlation window (yellow lines). 114

Figure 4.16: Velocity field model used for the domain conversion. From left to right, P-wave and S-wave RMS and interval velocities, depth-time curve corresponding to the corrected P-wave velocity log (red), the depth-time curve corresponding to the corrected S-wave velocity log (purple). 115

Figure 4.17: Comparison between frequency spectra from the PP seismic data in PP time (blue), the PS seismic data in PS time (green), and the PS seismic data converted to PP time (gray). Note the increase in both bandwidth and dominant frequency of the PS data when converted to PP time. 117

Figure 4.18: PP-PS horizon picking and event registration. PP section on PP time (left), PS section on PP time (right) and their interpreted horizons of the amplitude

trough of interest and the Lodgepole and Three Forks Formations. The inserted curves correspond to the PP and PS synthetic traces at the well V-1 location. 118

Figure 4.19: Cross-plots between the natural logarithm of P-impedance (Zp) and both S-impedance (Zs) and density (ρ) colored by the true vertical depth. The linear regressions of both plots are the background models for the inversion. 120

Figure 4.20: PP-PS post-stack joint-inversion results at the well V-1 location. The initial models, filtered original logs, and the inverted results correspond to the black, blue, and red logs, respectively. Note how the inverted P-impedance, S-impedance, density and Vp/Vs follow the general trend of the Bakken Formation. P-impedance, S-impedance and density inverted results seem to average the original response of Bakken Formation due to the effect of the low-frequency model. 122

Figure 4.21: SW-NE seismic sections of (a) filtered P-impedance low-frequency model and (b) inverted P-impedance going through the Well V-1 location. The displayed logs correspond to the computed P-impedance. 123

Figure 4.22: SW-NE seismic sections of (a) filtered S-impedance low-frequency model and (b) inverted S-impedance going through the Well V-1 location. The displayed logs correspond to the computed S-impedance. 124

Figure 4.23: SW-NE seismic sections of (a) filtered density low-frequency model and (b) inverted density going through the Well V-1 location. The displayed logs correspond to the density log. 125

Figure 4.24: SW-NE seismic sections of (a) filtered Vp/Vs low-frequency model and (b) inverted Vp/Vs going through the Well V-1 location. The displayed logs correspond to the computed Vp/Vs. 126

Figure 4.25: Difference between the PP seismic and the PP synthetic at the line going through the well location. Note that the amplitude of the traces is quite high. The real seismic and the synthetic seismograms are considerably different (error trace equal to 0.391). 128

Figure 4.26: PP-PS post-stack joint-inversion results at the well V-1 location using the PP stacked seismic filtered to the approximate seismic frequency of the PS data. The initial models, filtered original logs, and the inverted results correspond to the black, blue, and red logs, respectively. Note how the inverted P-impedance, S-impedance, density and Vp/Vs follow the general trend of the low-frequency

models instead of capturing the respective well log information in the Bakken Formation. 129

Figure 4.27: Comparison between the PP, PP filtered and PS seismic sections in PP time at the vicinities of the vertical well. From left to right, the PP seismic data, PP seismic data filtered to the approximate seismic frequency of the PS data, the PS seismic data. Note how most of the P-wave data are filtered which indicates that the PS frequency content is not sufficient for the joint inversion. 130

Figure 4.28: PP statistical wavelet extracted from the PP seismic filtered to the approximate frequency of the PS seismic data. The corresponding frequency spectrum is also shown. The wavelet extraction is performed in a window from 1500 to 2000 ms (a 500 ms window length). The dotted shows a zero-phase angle. 131

Figure 4.29: PP seismic amplitude vs. PS seismic amplitude cross-plot of the Bakken Formation interval, colored by PP time. The amplitude values are normalized. There appear to be no relationship between the two of them indicating that a statistical estimation or inversion is a better attribute that could be potentially used as the next step of the PP-PS joint inversion for the thin-beds characterization in the study area. 132

Figure 4.30: Statistical prediction of P-impedance. From left to right, actual P-impedance vs predicted target P-impedance cross-plot, and the P-impedance (Zp) log along with the predicted P-impedance log. The result of using 5 attributes achieves a 97% correlation. 139

Figure 4.31: Statistical prediction of density. From left to right, actual density vs predicted target density cross-plot, and the density (ρ) log along with the predicted density log. The result of using 5 attributes achieves a 98% correlation. 140

Figure 4.32: Vertical distribution of P-impedance by means of statistical prediction. The displayed log is the P-impedance log upscaled to the seismic frequency. Note how the Upper, Middle and Bakken member can be easily identified following the impedance changes. 141

Figure 4.33: Vertical distribution of density by means of statistical prediction. The displayed log is the density log upscaled to the seismic frequency. Note how the Upper, Middle and Bakken member can be easily identified following the changes in density. 142

Figure 4.34: Statistical prediction of brittleness. From left to right, actual brittleness vs predicted target brittleness cross-plot, and the brittleness log along with the predicted brittleness log. The result of using 5 attributes achieves a 98% correlation. 146

Figure 4.35: Statistical prediction of brittleness. From left to right, actual brittleness vs predicted target brittleness cross-plot, and the brittleness log along with the predicted brittleness log. The result of using 5 attributes achieves a 98% correlation. 147

Figure 4.36: Vertical distribution of TOC content by means of statistical prediction. The displayed log is the TOC log upscaled to the seismic frequency. Note how the Upper, Middle and Bakken member can be easily identified following the changes in TOC. The results show excellent correlations with the original log. Even though the Upper, Middle and Lower Bakken members are below seismic resolution, the statistical prediction is picking up the thin intervals with accurate TOC content. 148

Figure 4.37: Vertical distribution of brittleness by means of statistical prediction. The displayed log is the $E\rho/\nu$ log upscaled to the seismic frequency. Note how the Upper, Middle and Bakken member can be easily identified following the changes in brittleness. The results show excellent correlations with the original log. Even though the Upper, Middle and Lower Bakken members are below seismic resolution, the statistical prediction is picking up the thin intervals with accurate brittleness value. 149

Figure 4.38: Vertical distribution of the two organic-rich zones in the density and acoustic impedance domains. Blue zones are characterized by densities ranging between 2.0 to 2.15 g/cc and acoustic impedance lower than 20,000 g/cc*ft/s ("hot" Upper Bakken). Red zones are defined by densities between 2.2 – 2.3 g/cc and acoustic impedance from 20,000 to 25,000 g/cc*ft/s ("hot" Lower Bakken)..... 151

Figure 4.39: Vertical distribution of the two organic-rich zones in the density and Vp/Vs domains. Blue zones are characterized by densities ranging between 2.0 to 2.15 g/cc and Vp/Vs from 1.65 to 1.75 ("hot" Upper Bakken). Red zones are defined by densities between 2.2 – 2.3 g/cc and Vp/Vs from 1.65 to 1.75 ("hot" Lower Bakken)..... 151

Figure 4.40: Vertical distribution of the two organic-rich zones in the density and TOC content domains. Blue zones are characterized by densities ranging between 2.0 to 2.15 g/cc and TOC greater than 14 wt.% ("hot" Upper Bakken). Red zones are

defined by densities between 2.2 – 2.3 g/cc and TOC from 10 to 13 wt.% ("hot" Lower Bakken). 152

Figure 4.41: Vertical distribution of the low-TOC (< 7.5 wt.%) and high-brittle (> 400 GPa*g/cc) zones (in black). 152

Figure 4.42: Density vs. brittleness cross-plot. The selection of data points to highlight the different facies in cross-section is made using cutoffs values of 2.5 g/cc and 400 GPa*g/cc to discriminate the ductile or brittle shales from the rest lithology within the Bakken Formation..... 153

Figure 4.43: Vertical distribution of the brittle facies within the Bakken Formation. 153

List of Tables

Table 2.1: Average TOC values calculated with the Passey (1990) method for the Upper and Lower Bakken shale members using the P-wave sonic (DT), neutron porosity (NPHI) and density (RHOZ) logs in the well V-1. 34

Table 2.2: Average TOC values from core data of the well B, and TOC calculated with the Vernik and Landis (1996) and the Schmoker and Hester (1983) formulations for the Upper and Lower Bakken shale members using the density (RHOZ) logs in both wells B and V-1. The Schmoker's estimation seems to have a better agreement with the core TOC values..... 40

Table 2.3: TOC content and density ranges for the "hot" Upper Bakken and the "hot" Lower Bakken units. Note that the lower the density the bigger the TOC content. The "hot" Upper Bakken unit shows a greater TOC content. 54

Table 3.1: Densities, velocities and Bulk moduli of fluids calculated for the middle Bakken member using the FLAG 2014 models (Han et al., 2014). 64

Table 3.2: Calibrated Greenberg-Castagna empirical Vp-Vs relations for the Lodgepole, Bakken and Three Forks Formations using the log data from Well V-1..... 67

Table 3.3: Mean Vp, Vs, and density values for the Lodgepole, Bakken and Three Forks Formations. These values are calculated from Well V-1. 68

Table 3.4: Mean Vp, Vs, and density values for the Lodgepole, Bakken and Three Forks Formations. These values are calculated from Well A. 68

Table 3.5: Laboratory measurements of anisotropy parameters on the dry samples from Bakken shales with 70 MPa of confining pressure. From Vernik and Liu (1997), and Huang (2016)..... 70

Table 3.6: Mean ε, γ and δ values for the Lodgepole, Bakken and Three Forks Formations. These values are calculated from log data of Well A. 73

Table 3.7: Coefficients for the fitting of the Aki-Richards AVO approximation of the Zoeppritz equation for the Upper and Lower Bakken AVA curves. 81

Table 3.8: Mineral set for the fluid substitution in the middle Bakken Member. The elastic properties of the upper shale are used to define the properties of the constituents of the rock matrix in the Middle Bakken. The values for quartz and calcite, change very little with depth and are laboratory derived, so these are usually left at the default values. 82

Table 4.1: Parameters for the PP statistical and full wavelet extraction at the Well V-1. . 91

Table 4.2: Parameters for the PS statistical wavelet extraction at the Well V-1 112

Table 4.3: Background linear trend coefficients used in the PP-PS post stack joint inversion. 120

Table 4.4: List of attributes used to derive the multi-attribute relationship for P-impedance prediction in the Bakken Formation. 136

Table 4.5: List of attributes used to derive the multi-attribute relationship for density prediction in the Bakken Formation. 136

Table 4.6: Cross-correlation and error values for the P-impedance estimation after the single attribute regression, multi-attribute regression, and PNN. Note that the best correlation of 97% is achieved using the probabilistic neural network. . 137

Table 4.7: Cross-correlation and error values for the density estimation after the single attribute regression, multi-attribute regression, and PNN. Note that the best correlation of 98% is achieved using the probabilistic neural network. 138

Table 4.8: List of attributes used to derive the multi-attribute relationship for TOC prediction in the Bakken Formation. 143

Table 4.9: List of attributes used to derive the multi-attribute relationship for brittleness prediction in the Bakken Formation. 144

Table 4.10: Cross-correlation and error values for the TOC content estimation after the single attribute regression, multi-attribute regression, and PNN. Note that the best correlation of 99% is achieved using the probabilistic neural network. . 144

Table 4.11: Cross-correlation and error values for the brittleness estimation after the single attribute regression, multi-attribute regression, and PNN. Note that the best correlation of 98% is achieved using the probabilistic neural network. 145

Table 4.12: Density, TOC content, Vp/Vs, and acoustic impedance ranges that defined the two organic-rich zones of the Upper Bakken and Lower Bakken in the study area. 150

Chapter 1

Introduction

A major goal of applied seismic research is to understand and predict the seismic response of rock properties from variations of the seismic amplitude. To evaluate the amplitude behavior, different forward modeling processes and comparison techniques may be explored in the oil and gas industry, especially nowadays with the advent of modern oil production from shales through horizontal drilling and hydraulic fracturing. Therefore, the petrophysical and rock-physics analysis for understanding the relationship between rock properties and the elastic response, the evaluation of the AVO response for the anisotropic case, model-based estimations, and statistical predictions of P-impedance, density, Vp/Vs, TOC, and brittleness of the thin members of Bakken Shale; one of the largest oil developments in the U.S., are interesting topics that motivate this study.

1.1 The problem

Even though Bakken shale has been subject to extensive investigation, a better characterization of the anisotropic elastic properties of subsurface formations can improve the match of synthetics with post-stack amplitudes of field data and anisotropy should be taken into account at several stages of the interpretation workflow, from well-to-seismic tying and wavelet estimation to the generation of low frequency or initial models for the inversion process. Although it is widely recognized that anisotropy can have a significant influence in the depth imaging for focusing and positioning of migrated reflection events (Ferla et al., 2014), the effects of anisotropy in seismic data have often been neglected in AVO studies in unconventional prospecting in shales. Additionally, according to Wiley et al., 2014, one of the biggest issues facing exploration and production companies is the application of conventional geological and engineering techniques that have been developed and refined for over a century to unconventional resources that have emerge only within the past decade. In the special case of the Bakken Formation, with a production expected to rise in 2018 (Alford, 2017), better techniques must be employed to assess variations in reservoir and data quality. Hence, due to the small thickness of its inner members and the lack of high frequency multicomponent seismic data, the characterization and location of the best areas to produce hydrocarbon from this shale play are still subject of study and will support its viability for the future.

1.2 Objectives

This study aims to investigate the rock properties of the Bakken shale and how they relate to the elastic response. The cross-plot analysis is also carried out with the main purpose of finding a signature of the density and elastic behavior of the unconventional reservoir of interest. Furthermore, the effect of anisotropy in AVO modeling is taking into account in an attempt to aid the reservoir characterization of the Bakken Shale from surface seismic and well logs and a PP-PS joint inversion followed by a statistical multi-attribute prediction process are conducted to estimate P-impedance, S-impedance, density, and Vp/Vs and to map the vertical distribution of TOC and brittle facies within the thin Bakken members.

The main questions to address here are:

- How do the rock properties of the Bakken Shale relate to the elastic response?
- How does the inclusion of anisotropic AVO modeling affect the PP and PS seismic character?
- Is the PP-PS joint inversion a good approach for delimiting the Bakken formation and its respective members of interest?
- Which approach is most useful for impedance, density, and Vp/Vs prediction in the study area?

1.3 Anisotropy in shales

By contributing to the reduction of risk on angles, amplitude distortion and mispositioning of seismic reflectors, the characterization of seismic anisotropy is crucial for the exploration and development of unconventional reservoirs (Wild, 2011).

The sources of anisotropy in shales are the bedding-parallel alignments of clay mineral as well as kerogen particles in organic-rich shales (intrinsic anisotropy); the azimuthal anisotropy, and the lamination with different stiffness (layering anisotropy) (Yu et al., 2014). Its effects are often significant on both the travel time and amplitudes and they are needed to be taken into account for the accuracy of seismic imaging and inversion.

In seismic analysis of unconventional reservoir, knowledge of the anisotropy in the overburden, which is assumed to be made up of horizontal layering (characterized by VTI anisotropy) is of particular importance when building velocity models. The study of azimuthal variations in the amplitude versus offset (AVO) signature when the wave is reflected from the top or base of the shale enables improved imaging. Additionally, the understanding of how the shear-wave splits into two polarized components with their planes aligned parallel and perpendicular to the anisotropy gives an idea of the strike direction and fracture density of the fractured-layered medium (Wild, 2011).

1.4 Anisotropy in AVO modeling

In anisotropic media, the elastic properties are dependent on the direction of wave propagation (Thomsen, 1986). Transverse isotropy (TI) for compressional waves can be described by three independent parameters: P-wave velocity along the symmetry axis direction, and the dimensionless ε and δ which characterize the magnitude of anisotropy. The fractional difference between horizontal and vertical compressional wave speeds (assuming horizontal bedding) is related to the parameter ε and δ, on the other hand, controls the NMO velocity for horizontal reflectors as well as the small-angle reflection coefficient (Ferla et al., 2014).

In cases of transverse anisotropy, AVO Modeling is affected causing a change in reflectivity and shape modification of the incident wavefront. The Thomsen's dimensionless anisotropic parameters δ and ε can be used to predict AVO effects from anisotropy (Thomsen, 1986). For simple models, when $\delta>0$ or $\varepsilon>0$, AVO effects decrease and when $\delta<0$ or $\varepsilon<0$, AVO effects increase. However, the incident wavefront shape can be significantly affected too. Because the wave travels faster in either the vertical or the horizontal direction, the plane wave and the spherical wave have different travel times and incident angles for anisotropic layers. For both, the Elastic Wave Modeling that calculates spherical wave propagation and the Zoeppritz Modeling that calculates plane wave propagation, the reflection coefficient decreases because of anisotropic effects,

increasing the AVO effect. However, the incident angle becomes smaller than expected for the Elastic Wave model, reducing the AVO effects (Hampson and Russell., 1999).

For AVO and multi-component studies, the following equations and Thomsen's parameters are used.

$$Vp(\theta) = Vp(0°)(1 + \delta sin^2\theta cos\theta + \varepsilon sin^4\theta) \tag{1.1}$$

$$Vsv(\theta) = Vsv(0°)\left[1 + \frac{Vp^2(0°)}{Vsv^2(0°)}(\varepsilon - \delta)sin^2\theta cos^2\theta\right] \tag{1.2}$$

$$\varepsilon = \frac{Vp(90°) - Vp(0°)}{Vp(0°)} \tag{1.3}$$

$$\delta = 4\left[\frac{Vp\ (45°) - Vp(0°)}{Vp(0°)}\right] \tag{1.4}$$

Tsvankin and Thomsen (1994) applied Thomsen's theory to reflection moveout, giving an equation for P-waves in weak anisotropy as:

$$t_x{}^2 = t_0{}^2 + A_2x^2 + \frac{A_4x^4}{1 + (\frac{x}{V_0t_0})^2} \tag{1.5}$$

Where, $A_2 = \frac{1-2\delta}{V_0{}^2}$, $A_4 = \frac{2(\varepsilon-\delta)}{t_0{}^2V_0{}^4}$. The subscript 0 means zero offset, ε and δ are the Thomsen's parameters and the t values are arrival times. A_4 and A_2 equal zero when both Delta and Epsilon equal zero. In this case, the fourth order term disappear and the formula reduces to a normal hyperbolic moveout formula.

After a modification of Thomsen's equation, Ruger (2002) showed that a transversely isotropic term can be added to the Aki-Richards equation through the ε and δ parameters. Ran(θ) is the anisotropic AVO response and Ris(θ) is the isotropic response.

$$Ran(\theta) = Ris(\theta) + \frac{\Delta\delta}{2} sin^2\theta + \frac{\Delta\varepsilon}{2} sin^2\theta tan^2\theta \quad (1.6)$$

1.5 Bakken Shale

The Bakken shale ranks as one of the largest oil developments in the U.S. in the past 40 years. As of June 2017, The Bakken region is the third in terms of oil production after the Permian and Eagle Ford plays (EIA Drilling productivity report, June 2017). It is considered the most important hydrocarbon-bearing rock unit in the Williston Basin making North Dakota second to Texas in producing oil. Approximately 450 million barrels of oil (MMBO) have been produced from the Bakken and Three Forks Formations in the United States since 2008 and mean-undiscovered volumes of 7.4 billion barrels of oil, 6.7 trillion cubic feet of natural gas, and 0.53 billion barrels of natural gas liquids have been valued in its basin (Gaswirth et al., 2013). The U.S. Geological Survey has estimated the Bakken Shale Formation could yield 4.3 billion barrels of oil and estimates from Continental Resources stretch as high as 40 billion barrels according to the education and information source site for the Bakken shale play stakeholders managed by KED Interests, LLC.

Among the different oil shales in the U.S., Bakken Shale is one of the most prolific unconventional resource plays. It accounts for almost the 20 % of the entire oil production (5,348 Mbd in June 2017) with a new-well oil production per rig of 1,152 bbl/d in July 2017 (Figure 1.1).

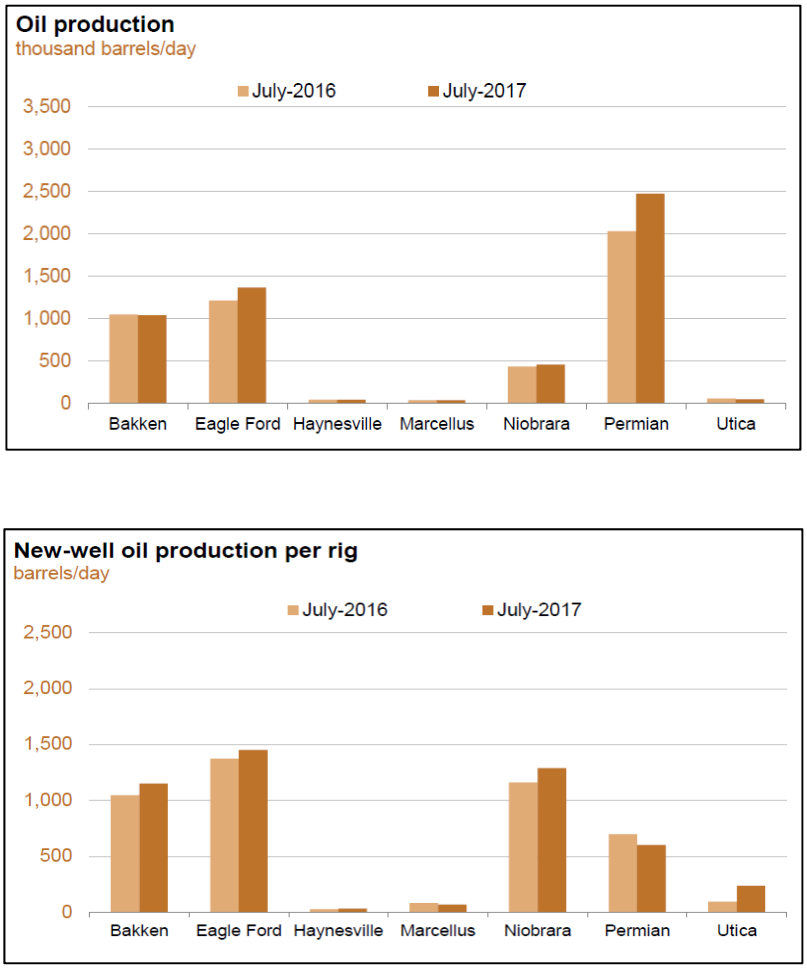

Figure 1.1: Comparison between oil production (above) and new-well oil production per rig (below) of different shale oil plays in the U.S. from July 2016 to July 2017. (EIA Drilling Productivity Report, June 2017).

Hydrocarbon production in the Bakken formation began in 1953 with conventional wells (Crews, 2015) but it was not until the late 1980's when horizontal drilling technology gained widespread acceptance in the oil and gas industry and led to increase production from its thin units (Wiley et al., 2004). The play has single-handedly driven North Dakota's oil production to levels four times higher than previous peaks in the 1980s. It not only boasts the lowest unemployment rate in the country at 3.1% (KED Interests LLC, 2017), but also the existence of highly developed midstream infrastructure and the basin's proximity to major consumer markets in Canada and the United States makes the Bakken one of the most readily exploitable hydrocarbon resources in the world. Operators are able to quickly move hydrocarbons from the ground to the well site to market which added fuel to the Bakken Revolution since late 2014 (Crews, 2015). Transport operations in the 1,200-miles Dakota Access Pipeline and the Energy Transfer Crude Oil Pipeline have already began on June 1st, 2017 carrying Bakken oil from North Dakota to distribution points in Illinois and then to the Gulf Coast. With production in the region expected to rise, some analysts predict that the pipeline system will reach 75% of capacity by year-end 2017. ESAI Energy LLC is one source predicting that Bakken will continue to experience production growth through next year. (Alford, 2017).

1.5.1. Geological background

The Williston Basin is a cratonic basin underlying the northern Great Plains of the northern United States and southern Canada (Figure 1.2). It occupies parts of Saskatchewan and Manitoba in Canada and the states of North Dakota, South Dakota and Montana in the United States (Gerhard et al., 1990). With approximately 345,000 km^2, this elliptical structural depression has its deepest part in the center and due to the long history of deposition of Pre-Pennsylvanian carbonates arranged in sequence packages of varying scales and Post-Mississippian detrital and evaporate deposits, that serves as a source and reservoir rocks, petroleum production is widespread in this basin (Du, 2015).

Containing a stratigraphic section mainly characterized by limestone and evaporates, there are many oil producing zones within the Williston Basin which have been evaluated for at least three stratigraphic units: the Ordovician Winnipeg shales, the Mississippian/Devonian Bakken Formation, and the Pennsylvanian Tyler Formation. Figure 1.3 shows the stratigraphic column of the basin.

Considered to be the major source of petroleum, the area of interest for this study includes the Bakken Formation that is defined as a restricted - shallow water mixed carbonate - clastic sequence deposited over most of the Williston Basin. It consists of three members (Lower, Middle, and Upper) that exhibit an onlapping relationship, and

converge and thin toward the margins or marginal shelf areas of the basin (LeFever et al., 1991).

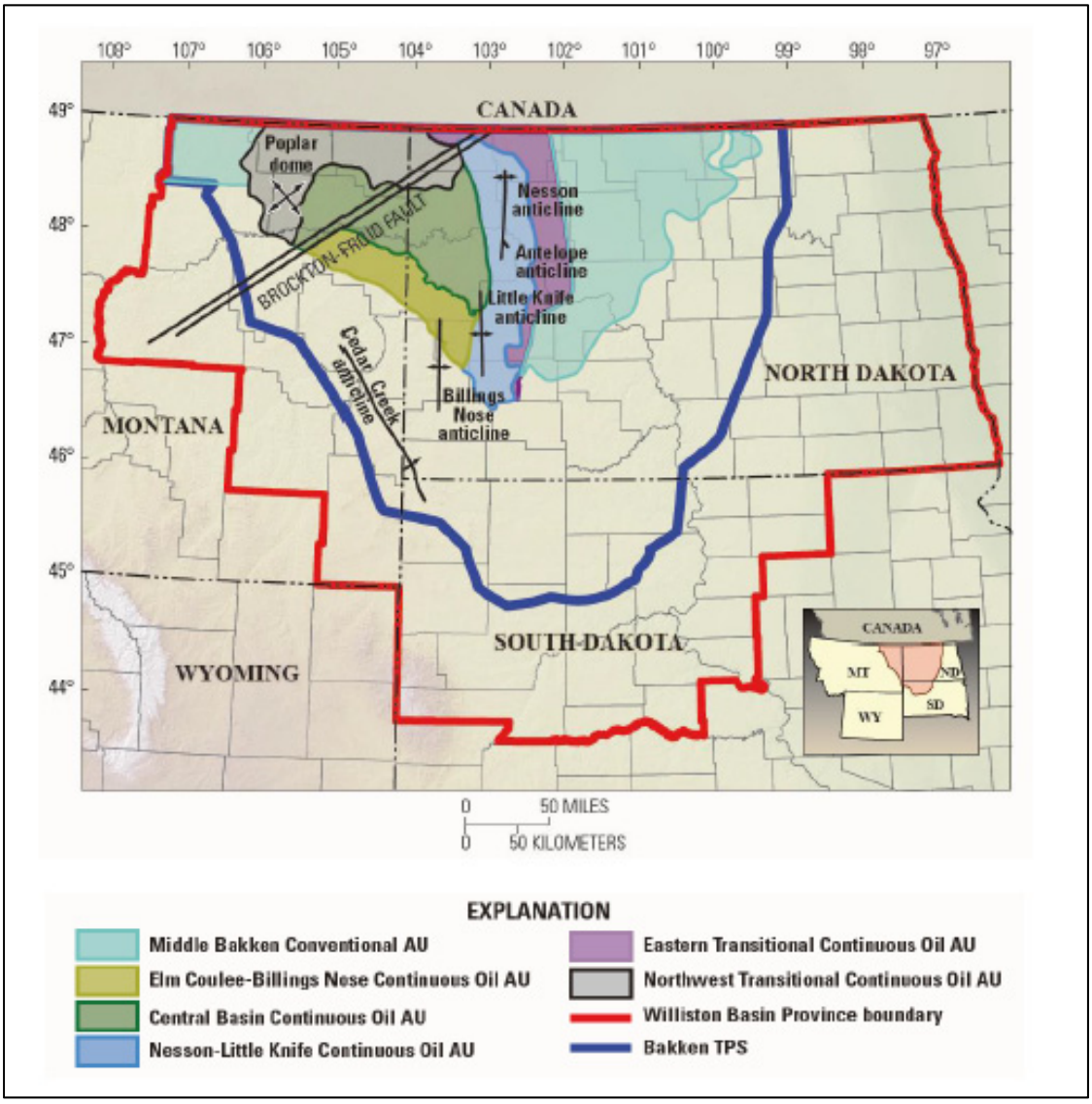

Figure 1.2: Map showing the Williston Basin Province, Bakken Total Petroleum System (TPS), and the Bakken Formation Assessment Units (AUs). Major structural features are also shown. Inset map shows the location of the Bakken TPS. (Modified from Du, 2015).

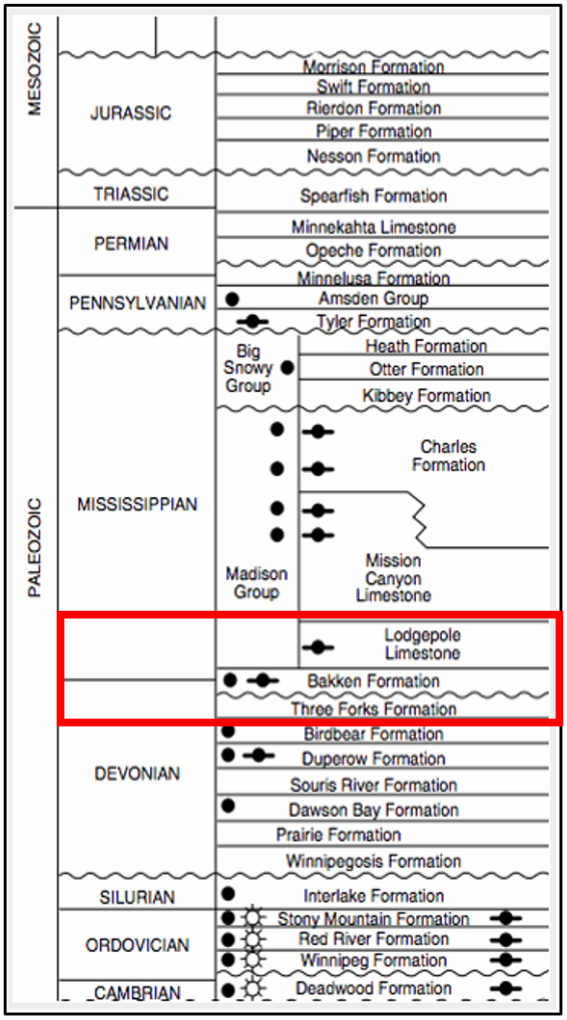

Figure 1.3: Stratigraphic column of the Williston Basin showing formations and major sequences. The red rectangle indicates the three main formations for this study. (Modified from KED Interests LLC, 2017).

1.5.2. The Bakken Formation

The Bakken Formation is a closed, low-permeability petroleum system that has generated approximately 3 to 4.3 billion barrels of technically recoverable oil in place (Omoboya, 2015) and it is easily recognizable on well logs (Figure 1.4).

The Bakken Formation overlies the Three Forks Formation and underlies the Lodgepole Formation. The Three Forks consists of interbedded mudstone and dolomite that can also serve as an oil reservoir. The Lodgepole, on the other hand, is made up of several shale-to-limestone cycles that are expressed as a progradational carbonate platform (Grover, 1996). The lower part of the Lodgepole limestone can be naturally fractured and act as a local reservoir.

The Bakken Formation has three distinct members: The Upper Shale Member, the Middle Clastic Member, and the Lower Shale Member. The Upper and Lower Members characterized by a dark marine shale with a high organic content exhibit very high gamma-ray readings (> 200 API), high-sonic slowness (80 to 120 μs/ft.), and low-resistivity readings (Pitman et al., 2001).

The Middle Member is typically constituted by mixed carbonate and clastic rocks. Its lithology is highly variable consisting of interbedded sequences of siltstones and sandstones with lesser amounts of shale, dolostones, limestone, and oolites (Pitman et al.,

2001). Measured porosity in the Middle Member ranges from 1% to 16%, averaging about 5%. Permeability ranges from 0 to 20 mD. as well, averaging around 0.04 mD. According to Pitman et al., 2001, higher permeability in the Middle Member corresponds to open and well-developed fractures and thus, most oil in the Bakken petroleum system is produced from the Bakken clastic Middle Member. The Bakken Formation in North Dakota reaches a maximum thickness of 145 ft (46 m) in the central portion of the basin, and the depocenter, which is located to the east of the Nesson anticline, trends in a north-south direction (Pitman et al., 2001).

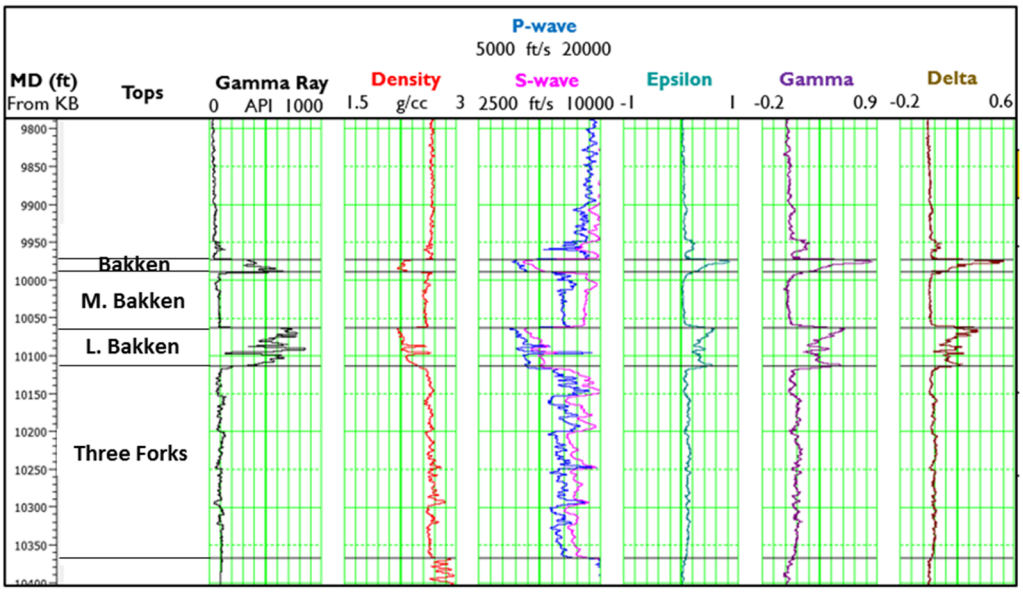

Figure 1.4: Gamma Ray, density, compressional and shear-wave velocities and Thomsen's weak anisotropy parameters logs from the Bakken Petroleum System (Mississippian Lodgepole Formation, the Devonian-Mississippian Bakken Formation, and the Devonian Three Forks Formation.

Thermal maturity of the Upper and Lower Bakken shale corresponds with the greater burial depth of the Bakken Formation in the study area and is a major factor for the productivity of this area (Crews, 2015). Thermal maturity of the Upper and Lower Bakken shales also correlates with overpressure within the Bakken Formation that has contributed to the generation of hydrocarbons by the conversion of solid, compressible kerogen to incompressible liquid hydrocarbons (Duhailan and Sonnenberg, 2014). This overpressure is a major driver of production in the Bakken tight oil system (Sorensen et al. 2010).

Sweet spots of the Williston Basin have been proposed on previous studies based on their geologic elements, historical well performance, thickness, thermal maturity, and overpressure (Crews, 2015). Therefore, high reservoir pressure, up-dip migration, diagenetic trapping, the presence of a mature source rock, a permeability conduit for hydrocarbon migration and a high-quality reservoir facies all characterize the sweet-spots (Crews, 2015). However, even within these sweet-spots, significant production variation exists between closely spaced wells (Sorensen et al. 2010).

1.6 Dataset overview

The dataset provided by the Allied Geophysical Laboratories for the purpose of this study consists of data reports, stratigraphic column, structural images and dissertations regarding previous research using the Bakken Shale data. The available Red Sky 2D-3C seismic data were acquired by Geokinetics in 2008 and comprises a seismic line of 3.4 miles oriented SW-NE. The 2D-3C data were processed in 2009 by GXT-AXIS Imaging Division, and two post-stack datasets were obtained corresponding to the vertical component and the radial component according to the following workflows (Figure 1.5).

	PP stacked data processing workflow	PS stacked data processing workflow
1	Geometry assignment and QC	Statistical trace edits
2	True amplitude recovery	True amplitude recovery
3	Surface consistent deconvolution	Surface consistent deconvolution
4	RoGain	Source refraction and residual statics
5	Refraction statics application – Shift to smooth floating datum	Receiver elevation statics
6	Three passes of residual statics	C-wave NMO correction
7	NMO correction	Front end mute
8	Mute and stack	Spike attenuation
9	Trim statics	CCP binning and stack
10	FX deconvolution – Random noise attenuation	FX random noise attenuation
11	Finite difference post-stack migration	Post-stack C-wave time migration
12	Spectral shaping / whitening	FX and eigenvector noise attenuation.

Figure 1.5: Processing workflows used for the generation of the PP and PS seismic data.

Figure 1.6 shows a comparison between the PP and PS full-stacked sections in their native times. Both seismic lines show good data quality and continuity of the events. The resolution of the PP data is noticeably better than that of the PS data. The target interval is located at approximately 1,700 ms in the PP section (PP time) and in 3,200 ms in the PS section (PS time).

One vertical well and in the vicinities of the 2D seismic line is provided. Four more wells approximately 17 miles apart from the seismic survey are also part of the database available. The suite of logs includes gamma ray, density, dipole sonic, neutron porosity and in some cases, resistivity and Thomsen's weak anisotropy parameters epsilon, and delta logs. Figures 1.7 and 1.8 show a map view of the location of the wells and the 2D seismic line.

1.6.1 Software

The well-log analysis is carried out using RokDoc, and the seismic modeling, well ties, inversions and statistical predictions are performed in Hampson-Russell using Geoview, ProMC, and Emerge modules.

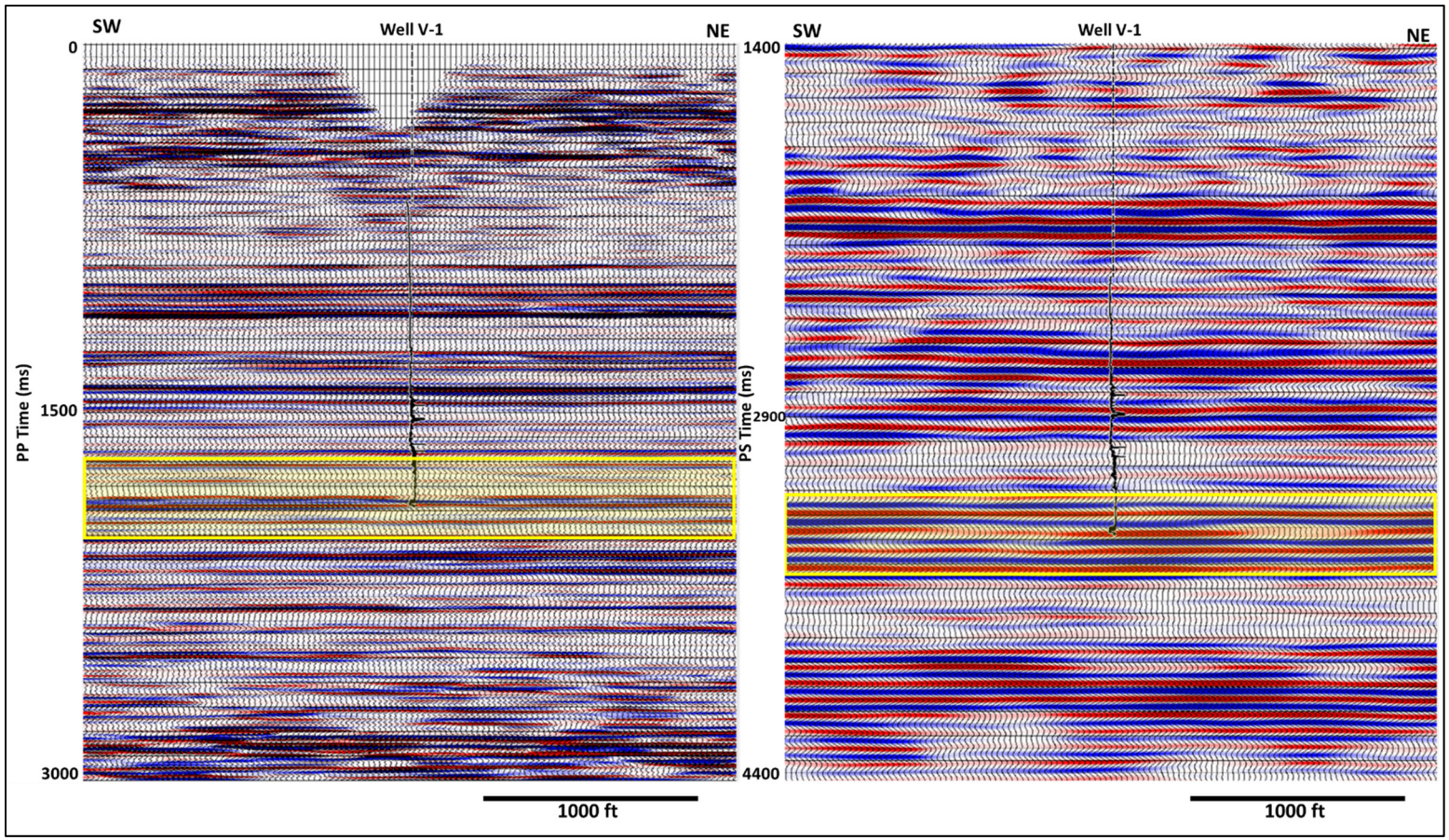

Figure 1.6: Comparison between the PP and PS stacked sections in their native times. The yellow polygon encloses the target interval: around 1,700 ms (PP time) and around 3,200 ms (PS time).

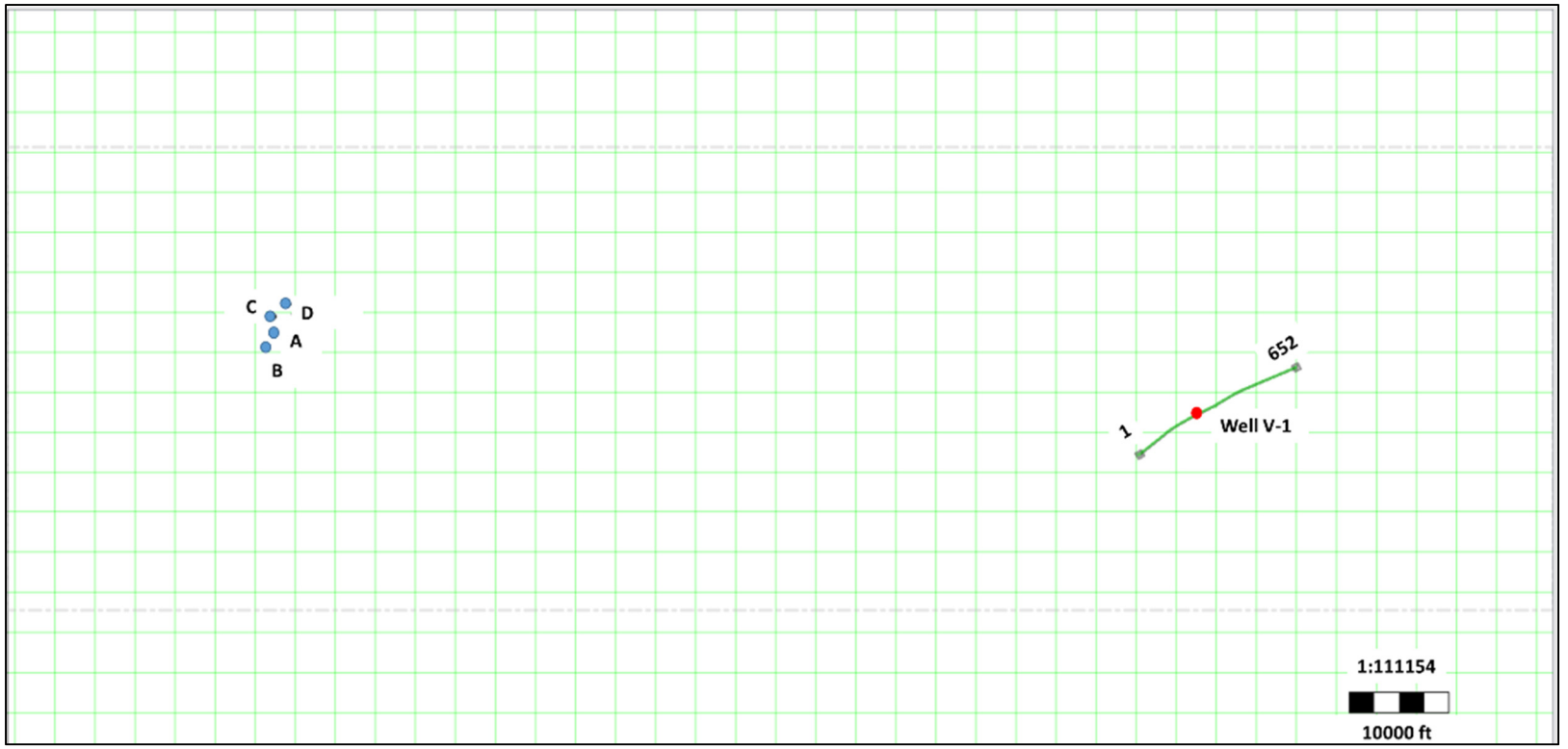

Figure 1.7: Base map showing the location of the wells available. 652 CDP. Coordinates are not plotted due to confidentiality.

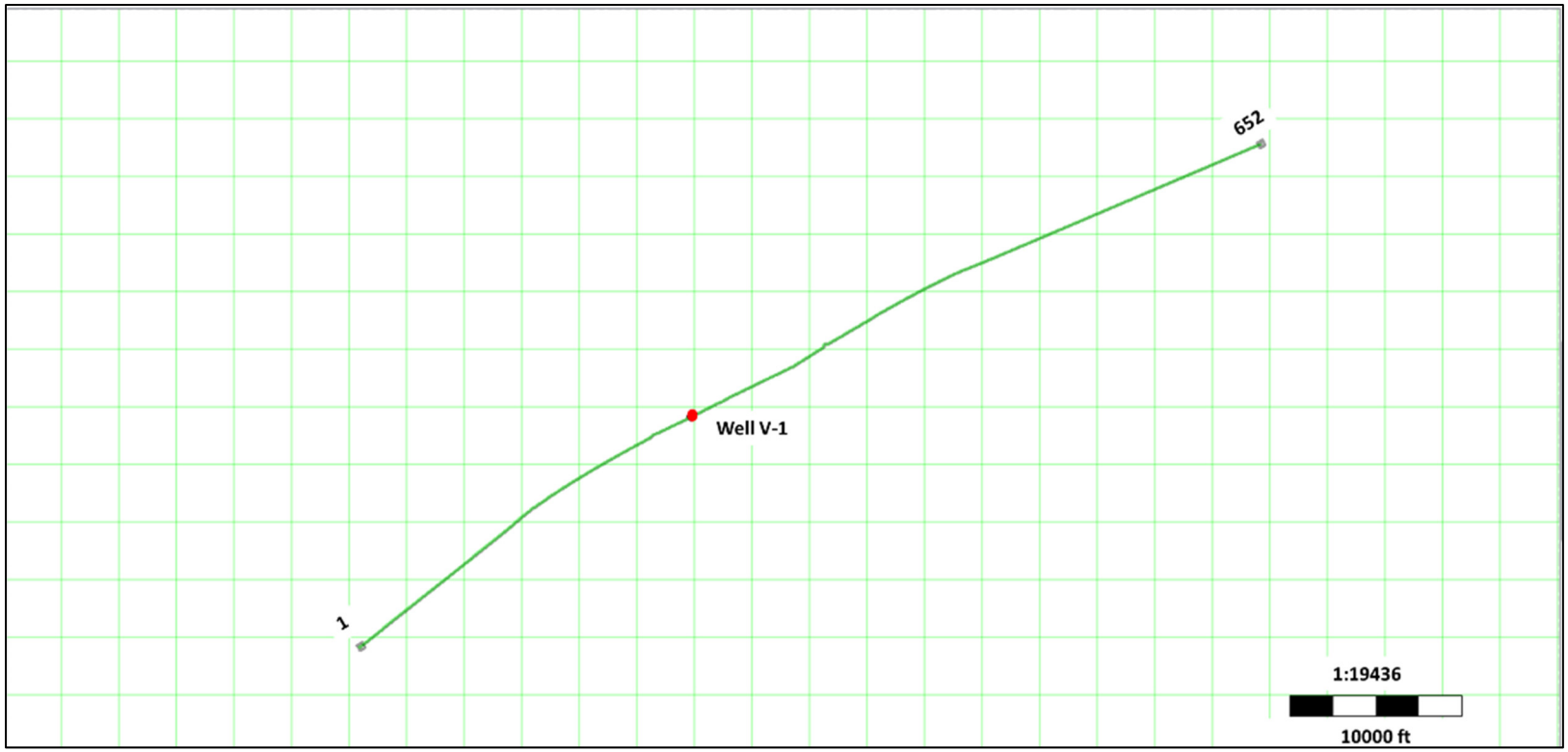

Figure 1.8: Base map showing the location of the vertical well in the vicinity of the 2D line of the Red Sky 2D-3C survey. 652 CDP. Coordinates are not plotted due to confidentiality.

Chapter 2

Well-log analysis and petrophysical properties

To understand the petrophysical properties of the reservoir and their relationship with the elastic parameters, well log data are used to investigate the rock properties of the Bakken shale in the study area, and how they relate to the elastic response (i.e. velocity and density).

In this chapter, the petrophysical evaluation comprises quality checking and editing of the available well logs. Then there is a description of their properties, evaluation of the intervals of interest and calculations to estimate the shale and clay volumes, TOC content, and brittleness for the vertical well V-1 in the vicinity of the seismic line. Cross-plot

analysis is also presented with the main purpose of finding a signature of the density and elastic behavior of the unconventional reservoir of interest.

Five wells with measured dipole sonic logs are available for this study. The suite of logs includes caliper, gamma ray, dipole sonic, and density measurements. Well V-1 includes neutron porosity and shallow and deep resistivity. In addition to log data, Well B contains spectral gamma-ray data and core TOC evaluation.

The Bakken Formation, a Devonian-Mississippian black shale and mixed sandstone/carbonate unit, is an important source rock for oil produced in the Williston Basin. The source rocks are world-class with total organic carbon content averaging 11 wt.%, and the reservoirs have been recognized as having low porosity and permeability. Natural fracturing enhances these reservoirs and results in reservoir "sweet spots" (Sarg, 2012).

According to Sarg (2012), the mineralogy across all the Middle Bakken lithofacies is very similar and is dominated by dolomite, calcite, and quartz. The Bakken shales show a diverse mineralogy and are quartz-rich (40-90% by volume). This, plus the carbonate content (5-40%), may play a significant role in making the Bakken shale brittle. The Upper Bakken shale is siliceous, which increases brittleness and enhances hydrofracturing potential. The Middle Bakken facies can all be reservoirs. Matrix reservoir quality is enhanced by dolomitization. Porosity is intercrystalline and tends to be greater than 6%.

The density porosity log may show high porosities around 30% but it does not imply matrix porosities in that range. Rather, this density-log response is due primarily to organic-matter which, with a specific gravity near 1.0 g/cm^3, is sensed by the density log as "porosity". Pyrite is a visually common constituent of the upper and lower shales and its presence, with a high density of 5.0 g/cm^3 should be taken into account in the calculation of organic carbon content from density logs (Schmoker and Hester, 1983). In these shale members, uranium associated with organic-matter is the principal cause of the high gamma-ray intensity (Schmoker, 1981). The low TOC shales are more brittle. The more mature and low TOC shales are, the more brittle and suitable for successful hydraulic fracturing (Yenugu and Han, 2013).

The thickness of the Bakken Formation in the study area decreases toward the location of the 2D seismic survey, from west to east, where it reaches a thickness of 90 ft in the vertical well V-1 (Figure 2.1). From the location of the wells A, B, C, and D to the vertical well V-1, the Upper Bakken member maintains its thickness around the 17 ft and the middle and lower members become thinner at 43 ft and 30 ft, respectively. Both shale members, the Upper Bakken, and Lower Bakken can be easily recognized in gamma-ray logs in these wells with API values higher than 150 related to the presence of radioactive materials such as uranium contained in shales deposited under marine conditions - type II kerogen (Passey et al., 2010).

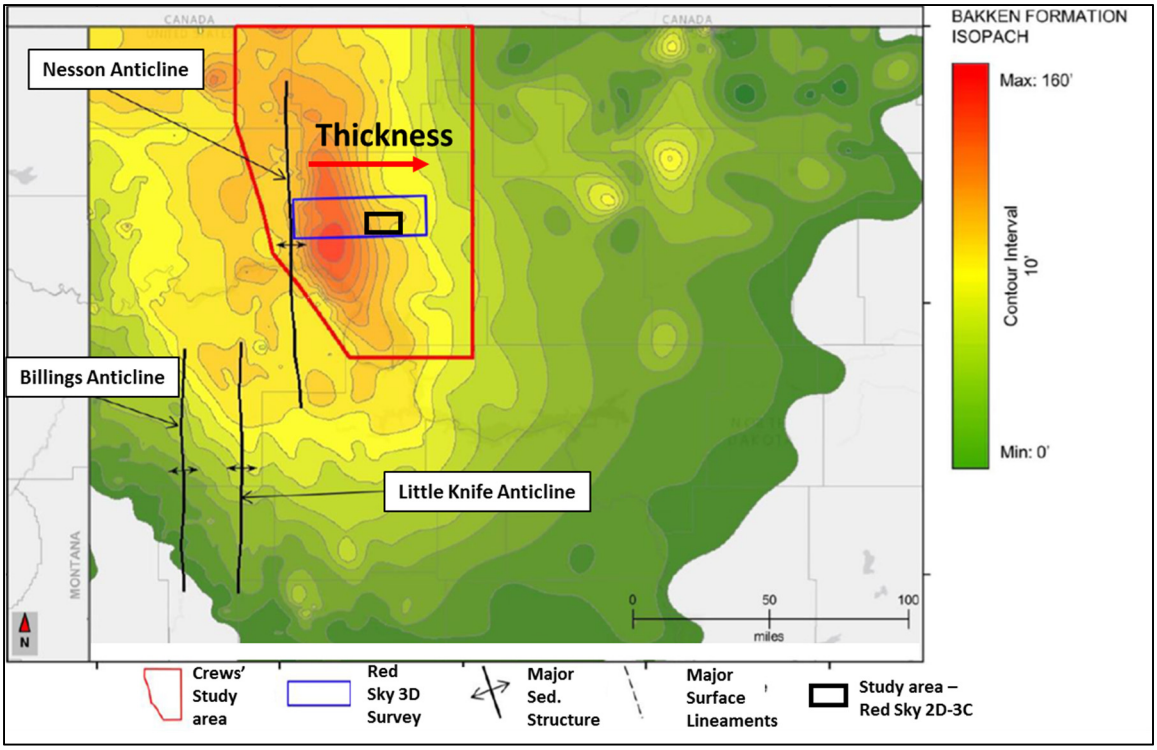

Figure 2.1: Bakken Formation isopach map showing thickness changes within the Bakken. The thickness of the Bakken Formation in the study area decreases toward the approximate location of the 2D seismic survey (black rectangle), from west to east. Coordinates are not plotted due to confidentiality. (Modified from Crews, 2015).

2.1 Shale volume estimation

The estimation of the shale volume in the zone of interest is performed in three ways in vertical well V-1, using the normalized version of the Gamma-Ray log (GR_n), and using both neutron and density porosity logs. Following the concept that the increase in radioactivity of the organic-rich shales is related to their organic matter content, the GR

and spectral GR responses need to be corrected for uranium before estimating clay content. This element forms compounds that sorbs to clays and organic material in both cases where their depositional environment is anoxic marine or oxidizing lacustrine (Ahmed and Meehan, 2016). Unfortunately, spectral GR data are not available for this well, so its correction for uranium is conducted by means of a linear empirical relationship constructed using both, the corrected spectral GR of the Well B plotted against the original GR log (Figure 2.2). The following equation is used for the GR correction for uranium:

$$GR_C = GR - 8U \tag{2.1}$$

Where, GR_C = Corrected GR, GR = total GR, and U = uranium in ppm.

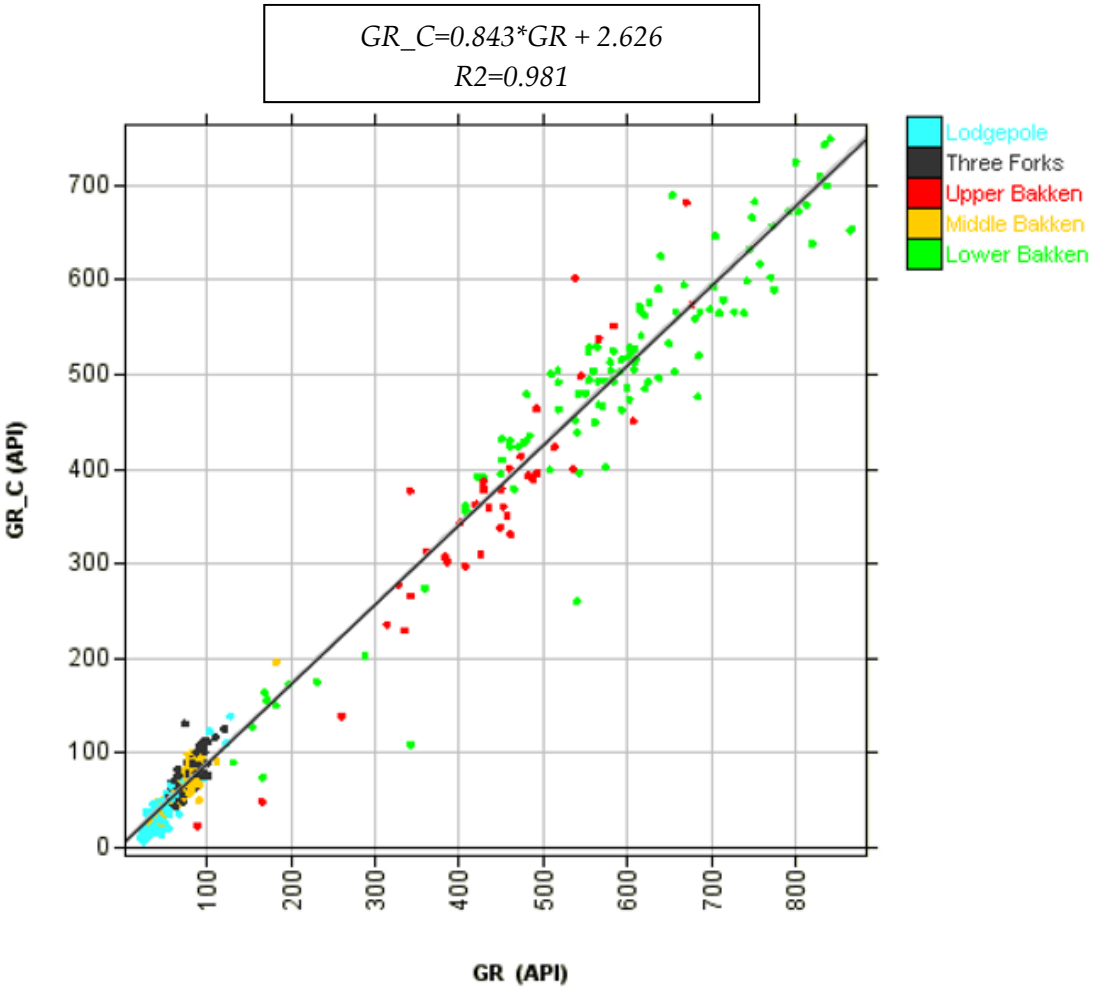

Figure 2.2: GR vs. Corrected Spectral GR for Well B, color-coded by formation. The correlation between both GR responses allows an adequate linear fit of 0.981. The linear empirical relationship is used to calculate the corrected GR for uranium in the Well V-1.

After correcting the GR for uranium to remove the effect of the organic matter, the normalization of the GR log is conducted as a method of reducing mud weight and hole size effects (Crain et al., 2014). The normalization process follows the assumption that all

pure shales in an area have the same GR values, and that all clean sands have the same GR log reading using the following equation:

$$GR_n = GR_{min} + \left[(GR_{max} - GR_{min}) * \frac{GR - GR_{low}}{GR_{high} - GR_{low}}\right] \quad (2.2)$$

Where, GR_n = normalized corrected GR in API units, GR_{min} = GR clean sand value to normalize to, GR_{max} = GR shale value to normalize to, GR = total GR, GR_{low} = GR clean sand value in the well/zone, GR_{high} = GR shale value in the well/zone.

To calculate Vshale from GRn, the following methodology was applied:

$$Vsh_{GRn} = \frac{(GR_n - GR_0)}{(GR_{100} - GR_0)} \quad (2.3)$$

Where, Vsh_{GRn} = shale volume from normalized GR log, GR_n= normalized GR, GR_0= GR log reading in 100% clean zone, GR_{100} = GR log reading in 100% shale.

The cutoffs for 0 and 100% shale correspond to 5 and 230 API units, respectively. On the other hand, given the neutron porosity log and the densities of clay (2.68 g/cc) and shale (2.35 g/cc), the volume fraction of shale (Vsh_{NPHI}) can be calculated via determination of the clay-bound water by setting values representative of clean sand and pure shale that correspond to the maximum and minimum value of the neutron porosity log, respectively.

Another method for estimating the shale volume uses both the density and neutron porosity logs. The linear interpolation of the separation between these two logs corresponds to the following algebraic formula to solve for shale volume:

$$Vsh_{PHI} = \frac{(NPHI - PHID)}{(NPHIsh - PHIDsh)} \tag{2.4}$$

Where, Vsh_{PHI} = Vshale from porosity logs, $NPHI$ = neutron log reading in zone of interest, $PHID$ = density log porosity reading in zone of interest, $NPHIsh$ = Neutron log reading in 100% shale, $PHIDsh$ = apparent density porosity in shale. The density porosity and neutron porosity of pure shale are 0 and 0.4, respectively. The neutron porosity at pure shale is taken from the density neutron cross-plot at the depths of the Upper and Lower Bakken shale.

The total GR, the corrected GR response for uranium and its normalized readings (thick black curve), the separation between density and neutron porosity, density porosity, and the comparison between the shale volumes (Vsh_{GRn}, Vsh_{NPHI}, Vsh_{PHI}) estimated for the vertical well V-1 are shown in the Figure 2.3. Note how the shale volume estimated from the normalized GR resembles the volume fraction of shale calculated from the neutron porosity log at depths of the Upper and Lower Bakken members. Although the Vshale values estimated from porosity logs differ from the volume of shale calculated with the GR readings for these two main shales of interest, they appear to be more similar for the middle clastic member of the Bakken Formation. The shale volume from the

density neutron cross-plot is not reliable at depths of the Three Forks Formation. In cases where the lithology is characterized by dolomites, the separation between the two curves is not a function of shale (Crain, 2000). In general, the shale volumes calculated follow the separation trend between NPHI and RHOZ: the higher the separation, the higher the shale volume.

Since a spectral gamma-ray log was available for the well B, the effect of the organic matter could be assessed in the Well V-1 by means of an empirical linear relation that allows the GR correction for uranium. However, the high-density log porosity of the upper and lower shale members is also due primarily to organic matter (Schmoker and Hester, 1983). Hence, the shale volume estimated from the normalized corrected GR log can be used as a guide of the relative volume of shale in the formation of interest, and the Vshale calculated from the porosity logs should be interpreted as an underestimation of the shale volume especially in the upper and lower shale members.

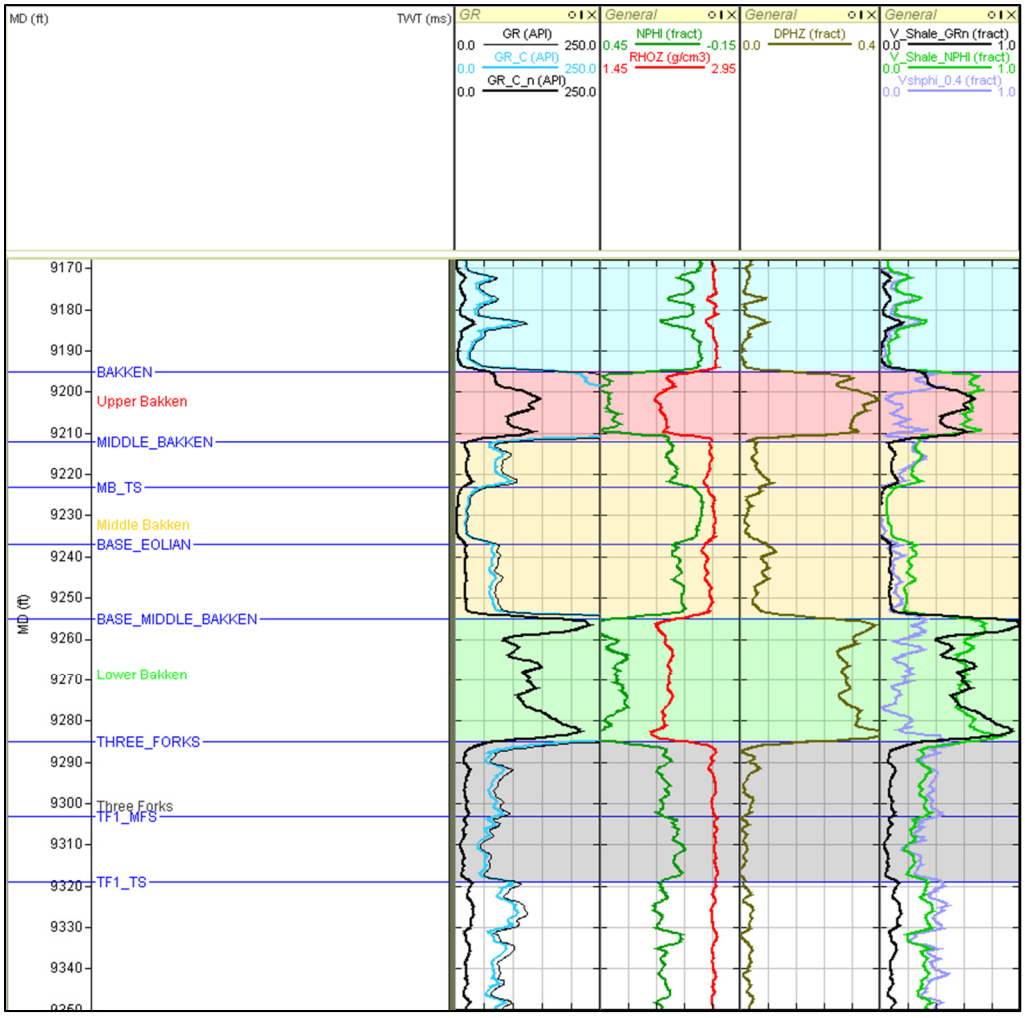

Figure 2.3: Well V-1 logs. From left to right, total GR, the corrected GR for uranium and its normalized readings (thick black curve), neutron porosity and density, density porosity and the comparison between the estimated shale volumes (Vsh_{GRn}, Vsh_{NPHI}, Vsh_{PHI}). Shale volumes calculated with the three methods follow the separation trend between NPHI and RHOZ except in the dolomitic Three Forks Formation. Since the high-density porosity reading in the Upper and Lower Bakken is due primarily to organic matter rather than porosity, values of shale volume in these two members are considered underestimated. Vsh_{GRn} and Vsh_{NPHI} are taken as better representations of the relative volume fraction of shales in the formation of interest.

2.2 TOC estimation

Total organic carbon (TOC) is an important parameter in the evaluation of kerogen-rich unconventional reservoirs (Charsky and Herron, 2013). An initial identification of zones with high TOC content is performed using the Heslop (2010) method. From the various existing approaches for TOC estimation, Passey (1990) and Vernik and Landis (1996) methods are applied to compare with the results of the estimation of the organic-carbon content in Bakken Formation proposed by Schmoker and Hester (1983). Core data are available for this study, so the calibration of the computed organic-carbon content will be conducted with the TOC values reported for the Well B.

The increase in GR readings and deep resistivity (RT) can be related to TOC within shales and there is a relationship between the curves associated with these two petrophysical properties. In a clean matrix, the GR typically decreases whereas the resistivity increases. On the other hand, in non-source shales (i.e. low TOC content), the GR increases while the Rt decreases. Since these two curves tend to "hour-glass" when plotted using conventional scales, reversing and selecting appropriate values for the Rt scale causes the GR and the Rt curves to track, except in source shales where both the GR and Rt values increase due to the TOC content (Heslop, 2010). This model was followed to identify areas of source shales in which the deviation of each of these two log curves from the non-source response is a function of TOC.

The method used to identify high TOC zones in the Bakken Formation is shown in Figure 2.4. As expected, the crossover between the GR and Rt curves is indicative of the TOC effect in the upper and lower shale members in which these two properties increase, and the hydrocarbon potential is observed on logs as lower density relative to shale density, "hot" GR response, increased P-wave sonic (DT) relative to shale DT, and increased neutron porosity relative to shale neutron.

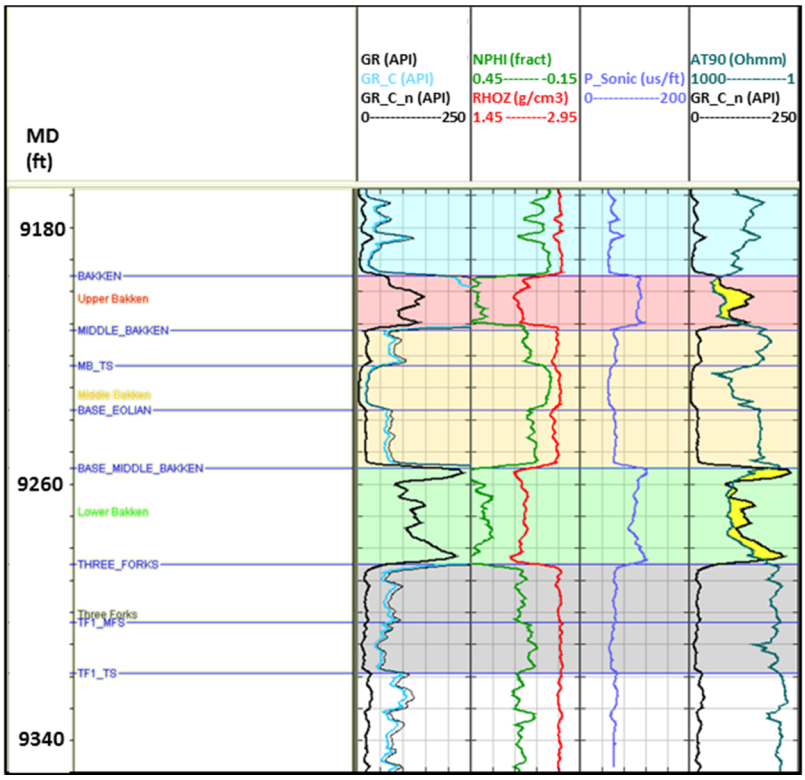

Figure 2.4: Well V-1 logs. From left to right, total GR and the normalized corrected GR (GRn), neutron porosity and density, P-wave sonic, and the superposition of the deep resistivity and the GRn curves. The cross-over between resistivity and gamma-ray readings (in yellow) is indicative of high TOC content.

Assuming that resistivity logs respond to fluids, while porosity logs (sonic, density, or neutron) respond to kerogen/matrix and fluids, the Passey (1990) method combines these two type of logs to estimate TOC in organic-rich rocks (Passey, 1990). Using either porosity curve, the method relies on porosity and deep resistivity readings separating from each other in organic-rich rocks, whereas in organic-lean rocks, the two curves overlie. The separation between the two curves or the scaled difference ($\Delta logR$) between them is related to the TOC content through the level of thermal maturation (LOM) by the following relation:

$$TOC(wt\%) = \Delta logR * 10^{(2.297 - 0.1688 * LOM)} \tag{2.5}$$

Where, $\Delta logR$ = scaled difference between deep resistivity and density logs and LOM = Level of organic maturity.

$$\Delta logR = \log_{10} \frac{RT}{RT_{baseline}} - \left[Scaling\ Factor * (PHI\ - PHI_{baseline})\right] \tag{2.6}$$

Where, RT = deep resistivity log in ohm/m, $RT_{baseline}$ = resistivity in the organic-lean zone in ohm/m, PHI = porosity log (i.e. sonic, density or neutron logs), $PHI_{baseline}$ = porosity log reading in the organic-lean zone. The scaling factor is calculated after baselining the two curves in the organic-lean zone.

If the type of organic matter is known, the level of organic maturity (LOM) (Hood et al., 1975) can be determined from a variety of measurements such as vitrinite

reflectance, thermal alteration index (Tmax) or Rock-Eval pyrolysis. In over-mature shale reservoirs with LOM values greater than 10.5, the limit of calibration of maturity to TOC is reached (Charsky and Herron, 2013). In this study, this value of 10.5 is used to define the LOM of the over-mature shale members of the Bakken Formation according to the value proposed by Passey et al., (2010). The average of TOC estimations for the upper and lower shale members are found in Table 2.1. The inorganic Three Forks Formation was taken as the baseline for $\Delta logR$ calculation in Passey's formulation. Figure 2.5 shows the estimated TOC logs using sonic, neutron porosity, density, and deep resistivity logs. Note the good agreement between the estimations calculated from the density and neutron porosity logs. The TOC values estimated from the P-wave sonic log (DT) appear to be lower and differ from the averages of the previous two estimations in approximately 18% and 24%, respectively. In the three cases, the TOC content of the upper shale member is greater than the organic carbon contained in the Lower Bakken.

Member	**TOC _RHOZ (wt. %)**	**TOC _NPHI (wt. %)**	**TOC _DT (wt. %)**
Upper Bakken	7.82	8.18	6.42
Lower Bakken	6.84	7.18	5.15

Table 2.1: Average TOC values calculated with the Passey (1990) method for the Upper and Lower Bakken shale members using the P-wave sonic (DT), neutron porosity (NPHI), and density (RHOZ) logs in the well V-1.

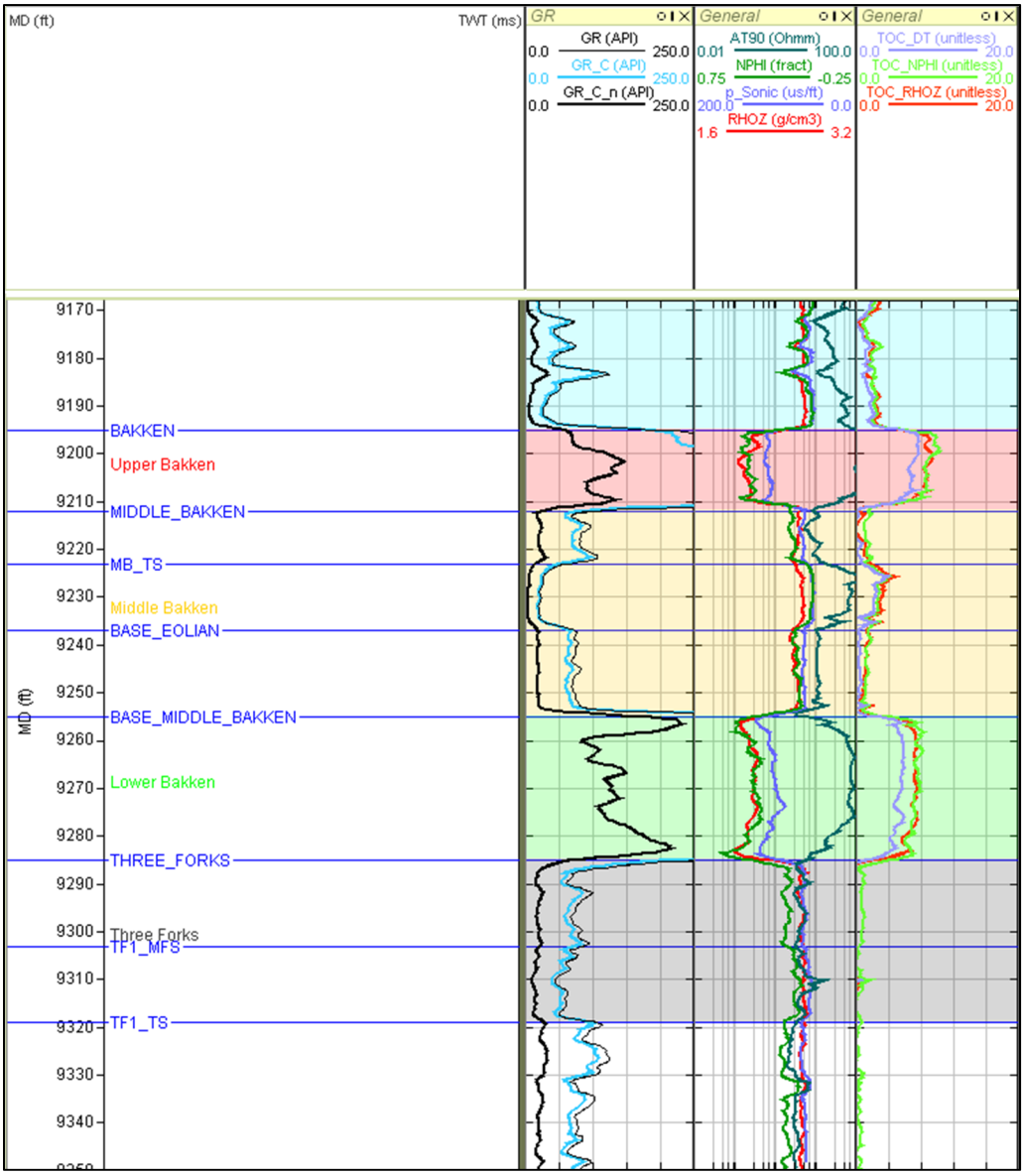

Figure 2.5: Estimation of the TOC from the Passey (1990) Method for the Well V-1. From left to right, total and normalized GR, deep resistivity, neutron porosity, P-wave sonic, density logs, and the comparison between their respective estimated values of TOC content. The inorganic Three Forks Formation was taken as the baseline for $\Delta logR$ calculation in Passey's formulation. Note how the curves approach to each other at the base of the Three Forks Formation in the second track.

Common TOC from density logs methods are highly susceptible to borehole effects (i.e. washouts) and tend to ignore lithology changes (Heslop, 2010). However, if heavy minerals (e.g., pyrite) are present as trace minerals, there is practically no variation in porosity, and there are good borehole conditions, using density logs could be a good method to estimate TOC. In the case of the Bakken Formation, not only these conditions are met, however, variations in organic content are expected to cause significant changes in the bulk density of the formation due to the organic matter density of about 1.0 g/cc contained in shale members with a matrix density of 2.68 g/cc (Schmoker, 1983).

Assuming that the change in density of the formation is due to the presence or absence of low-density organic matter, an empirical approach was developed by Schmoker (1979) to quantitatively estimate TOC in Devonian shales from log data. The methodology was then refined for the Bakken black shales which were treated as a four-component system consisting of rock matrix, interstitial pores, pyrite, and organic matter. High-density minerals other, than pyrite, are assumed to comprise a fixed (but unknown) percentage of the rock matrix (Schmoker and Hester, 1983). The formulation for TOC calculation with the Schmoker method is shown as follows:

$$TOC(wt\%) = \left(\frac{154.497}{\rho}\right) - 57.261 \tag{2.7}$$

Where, ρ = bulk density in g/cc, and the constants were specifically calculated for the upper and lower shale members of the Bakken Formation based on an organic matter

density of 1.01 g/cc, a matrix density of 2.68 g/cc, and a ratio between weight percent of organic matter and organic carbon of 1.3. The study reported an average of organic-carbon content in the upper and lower shale members of 12.1 wt.% and 11.5 wt.%, respectively, calculated at 159 locations in North Dakota and 107 in Montana.

Vernik and Landis (1996) also proposed an empirical formulation for TOC estimation using the density log as follows:

$$TOC(wt\%) = 67 * \frac{RHO_K(RHO_S - RHOB)}{RHOB(RHO_S - RHO_K)} \quad (2.8)$$

Where, $RHOB$ = density log, RHO_S = clay density and RHO_K = kerogen density.

Based on the Schmoker and Hester (1983) work in the Bakken Shale, in this study, the clay and kerogen densities are assumed to be 2.68 g/cc and 1.01 g/cc, respectively.

The last two methods were also applied for the estimation of TOC in the Bakken shales of the Well B and then compared with its reported TOC values from the available core data. Figure 2.6 shows the comparison between the TOC core values and the TOC estimations for both well B and well V-1. Note all the curves follow the relative trend. In well B, note the general similarity between the TOC core values and the Schmoker's TOC estimation in the Lower Bakken member. Considerable differences between the core data and the two calculated TOC values can be noticed in the upper shale member except in the middle Upper Bakken where both, the TOC reported data and the Schmoker's

estimation, range around 11 wt.%. On the other hand, well V-1 shows that at the very top of the Upper Bakken, Passey's and Vernik's estimations are in good agreement and they start to differ in the middle upper shale member. Since Passey's TOC is influenced by noisy readings in the resistivity response (Ruiz, 2016), the spikes in the resistivity logs at depths of middle Upper Bakken and Lower Bakken can be causing this mismatch.

Vernik's method tends to underestimate the values of TOC by as much as 4 wt.% in both wells in comparison with the TOC from core data. The average TOC values estimated with Vernik's and Schmoker's methods for both black Bakken shales in the wells B and V-1 are presented in Table 2.2. The average TOC values appear to increase from the upper to the lower shale members but the overall well trend (Figure 2.5) indicates that, with the exception of the very top and base of the Lower Bakken, its TOC values are generally lower than the values at Upper Bakken as it is shown in the reported core data.

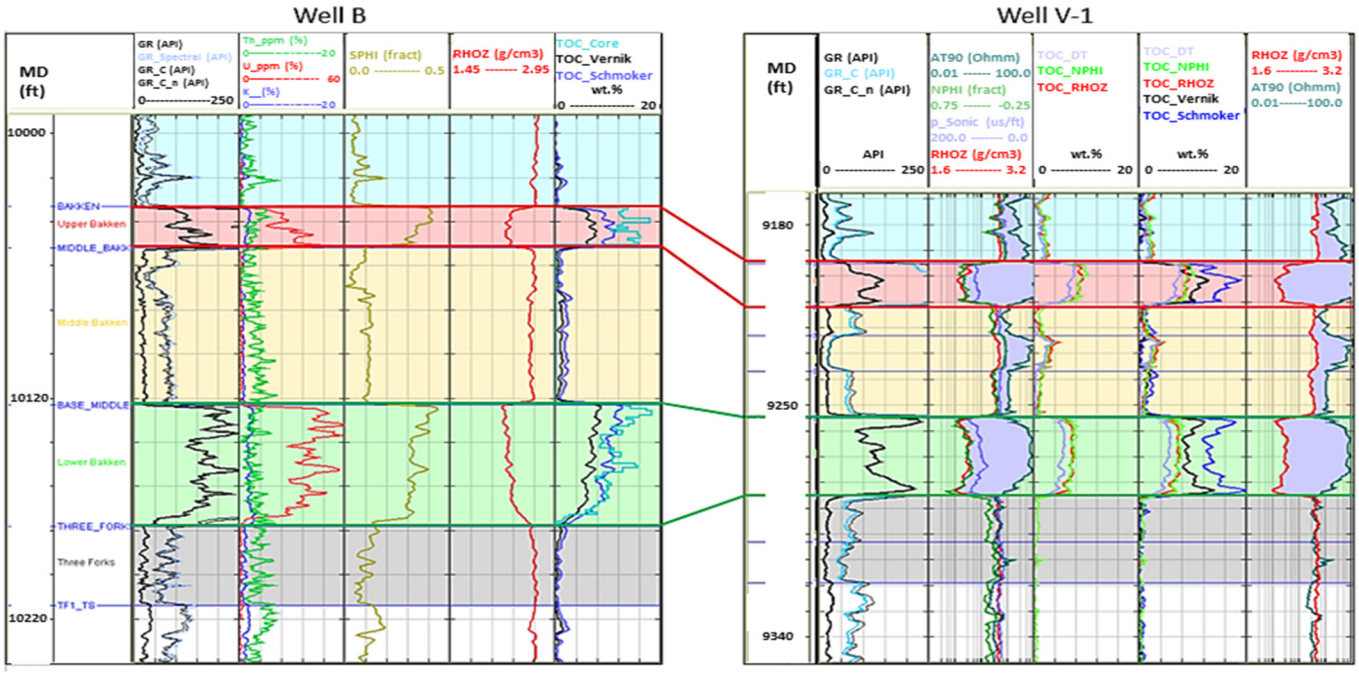

Figure 2.6: Comparison between the TOC estimations at the well B and well V-1. From left to right (In the well B), total gamma-ray (GR), density (RHOZ), sonic porosity (SPHI), and the comparison between the TOC curves from Vernik and Landis (1996), and Schmoker and Hester (1983). From left to right (In the well V-1), total and normalized GR, deep resistivity (AT90), neutron porosity (NPHI), P-wave sonic (DT) and density (RHOZ) logs, the comparison between the estimated values of TOC by the Passey (1990), Vernik and Landis (1996) and Schmoker and Hester (1983) methods, and the resistivity (AT90)-density (RHOZ) overlay for $\Delta logR$ calculation, where areas highlighted in purple correspond to high organic-matter zones.

Member	Well B			Well V-1	
	TOC_Core (wt.%)	TOC_Vernik (wt.%)	TOC_Schmoker (wt.%)	TOC_Vernik (wt.%)	TOC_Schmoker (wt.%)
Upper Bakken	12.47	6.08	9.03	9.16	13.42
Lower Bakken	10.30	6.30	9.35	9.79	14.32

Table 2.2: Average TOC values from core data of the well B, and TOC calculated with the Vernik and Landis (1996) and the Schmoker and Hester (1983) formulations for the Upper and Lower Bakken shale members using the density (RHOZ) logs in both wells B and V-1. The Schmoker's estimation seems to have a better agreement with the core TOC values.

The increase of approximately 8% and 40% in the TOC values reported in the well B to the estimated TOC of the well V-1, for the upper and lower shale members, respectively, can be due to the well location relative to the basin. According to Schmoker and Hester (1983), in the United States portion of the Williston Basin, around the location of both wells (Figures 2.7 and 2.8), the organic-carbon content increases sharply towards the East in both upper and lower members due to a well preservation of the algal kerogen in these areas, resulting in a higher organic-carbon content and a less inert organic matter with better oil-generation potential in the vicinities of the vertical well V-1.

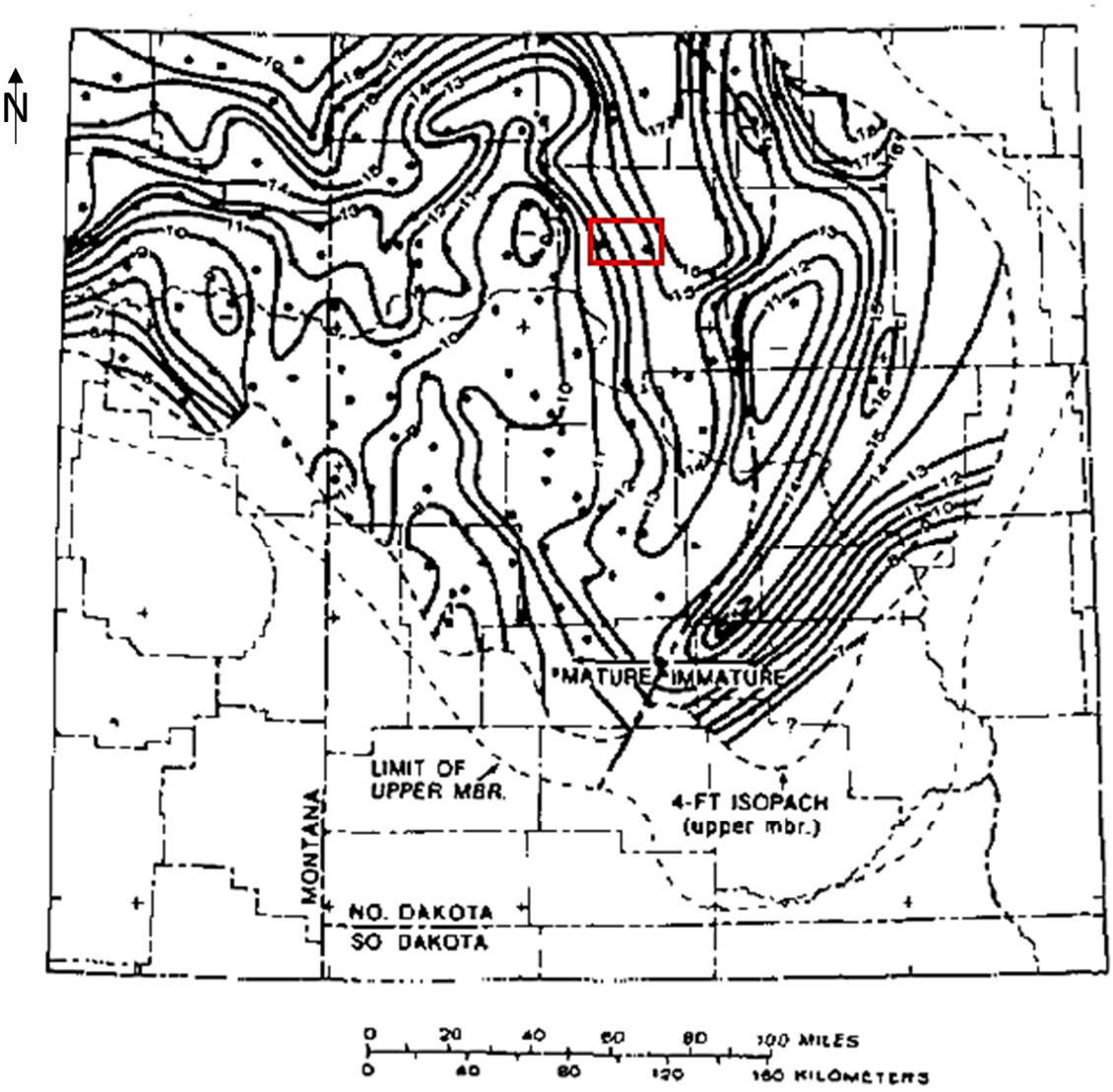

Figure 2.7: Organic-carbon content (wt.%) of the upper member of Bakken Formation. Contour interval is 1.0%. The red rectangle shows the location of the wells B and V-1. Note the increase of TOC values in East direction inside the study area. Coordinates are not plotted due to confidentiality. (Modified from Schmoker and Hester, 1983).

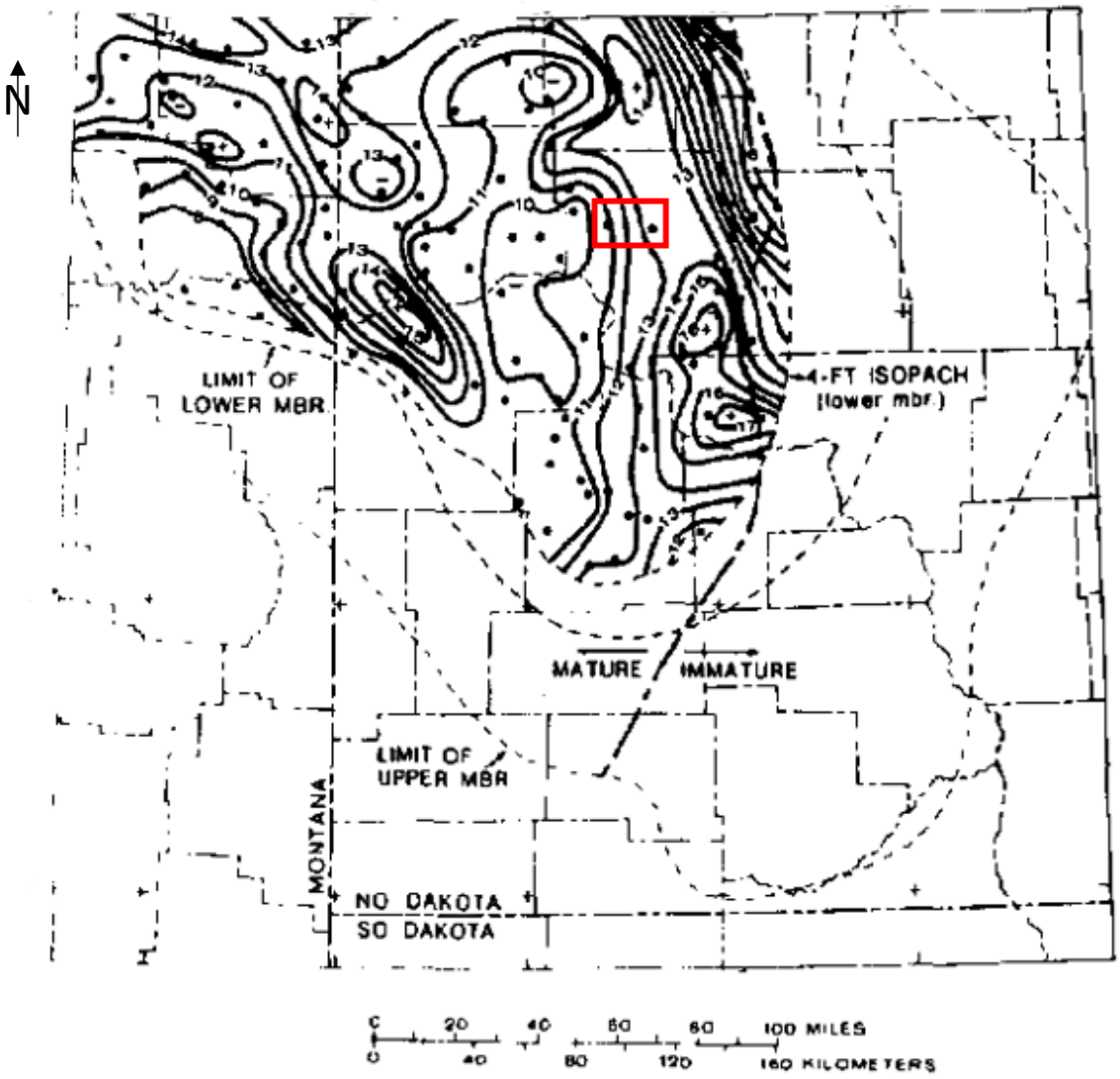

Figure 2.8: Organic-carbon content (wt.%) of the lower member of Bakken Formation. Contour interval is 1.0%. The red rectangle shows the location of the wells B and V-1. Note the increase of TOC values in East direction inside the study area. Coordinates are not plotted due to confidentiality. (Modified from Schmoker and Hester, 1983).

Since the Passey formulation utilizes resistivity and porosity logs, and Vernik's method is based on density logs, their associated TOC estimations are conditioned by their response, readings, and implications. Porosity logs incorporate a lithology response in addition to porosity, the noisy resistivity readings might cause underestimation of TOC, and the complication of borehole related errors associated with the utilization of density logs may influence the final calculations. Therefore, the Schmoker and Hester empirical method, derived from the calculations in 266 locations in the Williston Basin, seems to be more reliable to define the Bakken shales TOC in the area of study and it also has a better agreement with the reported TOC core values of the calibration well B.

2.3 Cross-plot analysis

To identify the combination that better describe the relationship between the geomechanical, petrophysical, and elastic characteristics of the Bakken Shale, all the five vertical wells were evaluated and compared to finally delimit a zone of interest with properties that might be recognized in the seismic inversion results. With the main purpose of finding a signature of the density and elastic behavior of the unconventional reservoir of interest, plots of density versus P-wave and S-wave velocities and plots Vp-Vs will enable us to study the relationship between these properties to characterize this potential hydrocarbon shale.

Figure 2.9 shows cross-plots between the shear-wave velocity against its slow and fast components for the four vertical wells A, B, C, and D. Note how both components correlate to the S-wave velocity log with a 0.98 coefficient. The values of the upper and lower shale members of the Bakken Formation appear to have a better fit. In general, the Vs, Vs_slow, and Vs_fast logs show similar values at each depth. The three shear wave velocity readings are approximately 5940 ft/s and 6220 ft/s for the Upper Bakken and Lower Bakken, respectively.

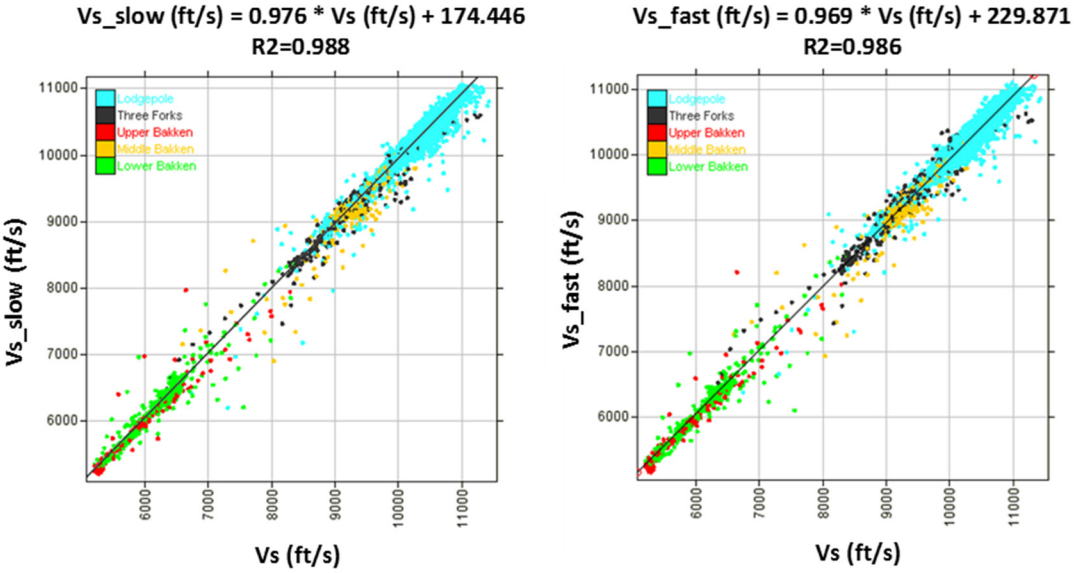

(a) (b)

Figure 2.9: Vs vs. (a) Vs_slow and (b) Vs_fast cross-plots for well A, B, C, and D, color-coded by formation. The correlation between Vs and both the Vs slow and fast components allows an adequate linear fit of 0.98.

Figure 2.10 shows cross-plots between Vp and Vs for the five wells, color-coded by (a) member and (b) gamma-ray. Since the differences in values of Vs, Vs_slow and Vs_fast are not substantial, the Vs logs of all the wells are used in the cross-plot analysis. The Castagna mudrock line for brine-saturated siliciclastic rocks (Castagna et al., 1985) was plotted as a guideline. The siltstones and sandstones of the Middle Bakken member plot toward high Vp/Vs values and the same occurs with the high-velocity carbonates of the Lodgepole and Three Forks Formations. Both Upper and Lower Bakken Shale deviate significantly from the trend and show lower P and S-wave velocities, and hence lower Vp/Vs (around 1.6). The combination of fluid (oil saturation) and TOC content might cause the deviation from the background trend. The correlation between Vp and Vs allows an adequate linear fit with a correlation coefficient of 0.956.

In the density vs. P-wave velocity cross-plots (Figure 2.11) a lithological trend can be observed from high to low Vp and density. The Lodgepole limestones, Three Forks dolomites, and Middle Bakken siltstones are recognized by their high velocities (> 15,000 ft/s), and organic-matter-rich shales from Upper and Lower Bakken members can be easily discriminated in the density domain, showing values lower than 2.5 g/cc. Not only the low density of kerogen has a substantial effect on the elastic properties of the rock (Prasad and Zargari, 2014) but also the oil saturation changes the compressibility of the rock, causing a decrease in velocity and density.

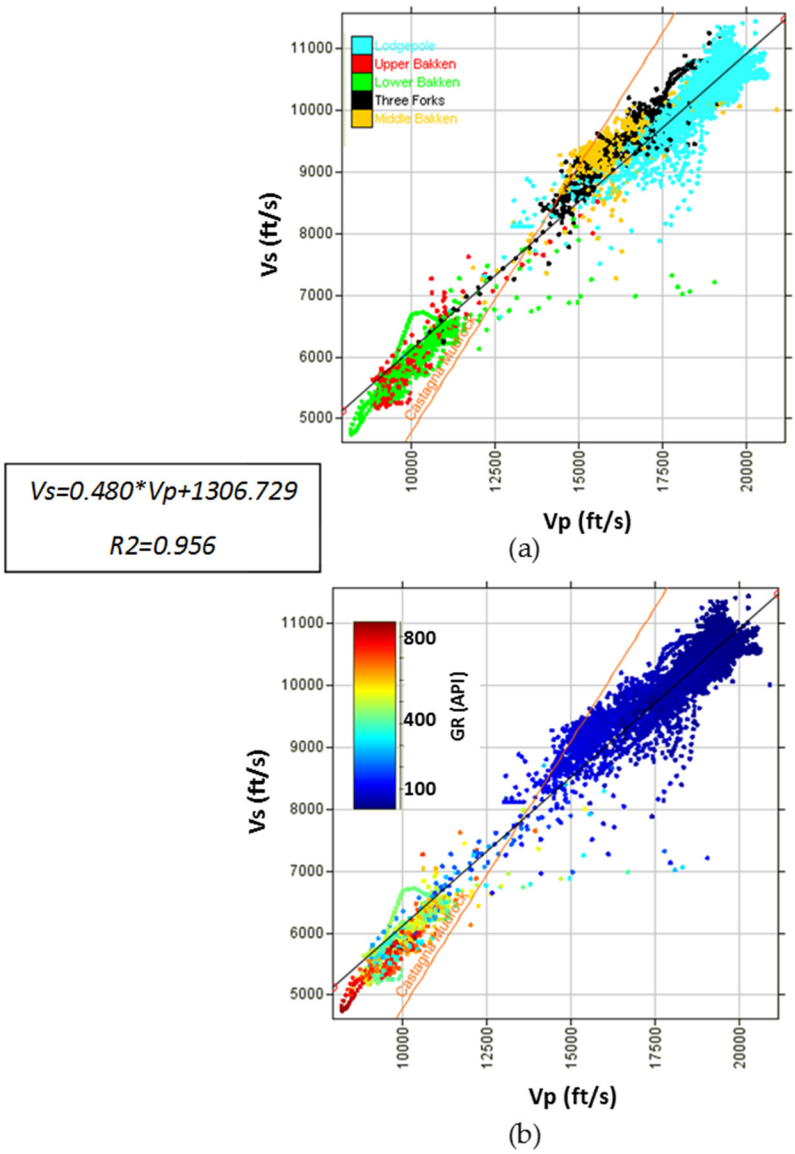

Figure 2.10: Vp vs. Vs cross-plot for Well A, B, C, D, and Well V-1, color-coded by (a) formation and (b) GR. Note how both, Upper and Lower Bakken shales deviate from the Castagna's mudrock line (Castagna et al., 1985) towards lower velocities which can be caused by oil saturation and especially TOC content. The correlation between Vp and Vs allows an adequate linear fit of 0.957.

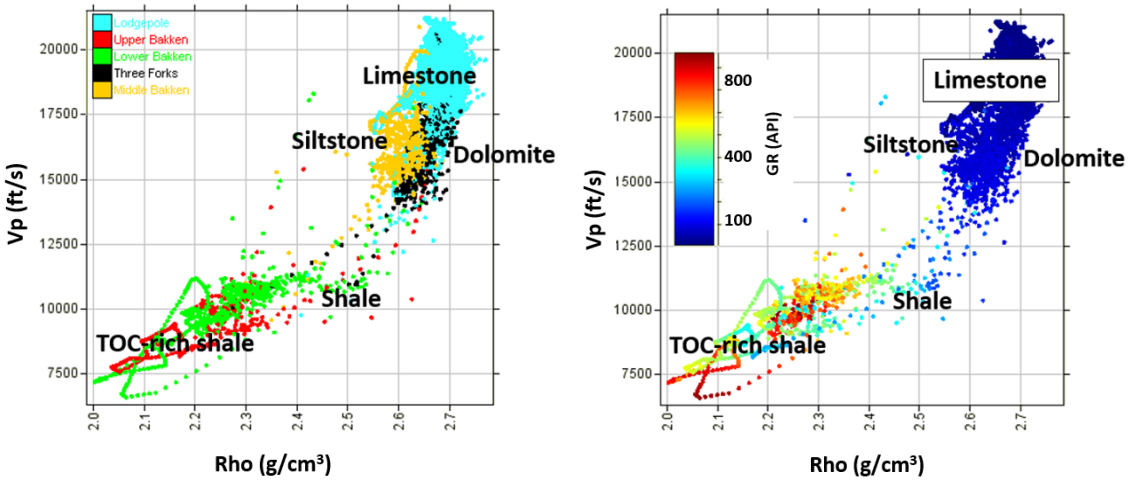

(a) (b)

Figure 2.11: Density vs. Vp cross-plot for Well A, B, C, D, and Well V-1, color-coded by (a) formation and (b) GR. Note how both, Upper and Lower Bakken organic-rich shales can be easily identified in the density domain with values lower than 2.5 g/cc.

To understand the behavior of the reservoir rocks in terms of the mineralogy and elastic properties that characterize the organic-rich shales of the Upper and Lower Bakken, Figures 2.12 and 2.13 show cross-plots that include samples of density-Vp and density-Vs from the five wells: A, B, C, D, and V-1. These cross-plots are represented for the Bakken Formation only. Rocks with TOC content higher than 10 wt. % deviate from the ones that have lower TOC in the density domain and exhibit slightly lower velocities and lower densities (< 2.3 g/cc) within the Bakken Formation. The presence of kerogen leads to a decrease in all elastic moduli (Sayers, 2013), so the increase in TOC content is expected to cause a decrease in both density and velocities. These high TOC rocks show a generally

higher shale content than those with lower TOC content (2.5 – 7.5 wt.%). These observations agree with the previous studies of stratigraphy (Sarg, 2011) and mineralogic content (Smith et al., 1958) of the Bakken Shale in North Dakota in which the most organic-rich sediments are found to be associated with high quartz, silt, siliceous microfossils, clay, and pyrite content.

Based on this observation and the hydrocarbon potential of shales observed on all the five wells as elevated resistivity, lower density relative to shale density, a high GR response greater than the shale GR, and an increased P-wave sonic relative to the one for shales, two "hot" organic-rich zones can be separated from the Upper Bakken and Lower Bakken (gray and black polygons) showing TOC trend, where the lower the density and velocity, the higher the TOC content. P-wave velocity (Vp) seems to be a good lithological indicator for these two units, showing a decrease in their values as TOC content decreases. However, since the shale content associated with clay does not show a noticeable pattern or trend, the interplay between the inorganic minerals does not seem to be a significant factor driving velocity changes in the two high TOC units. Note that the well V-1 has the highest TOC content within the Bakken Shale.

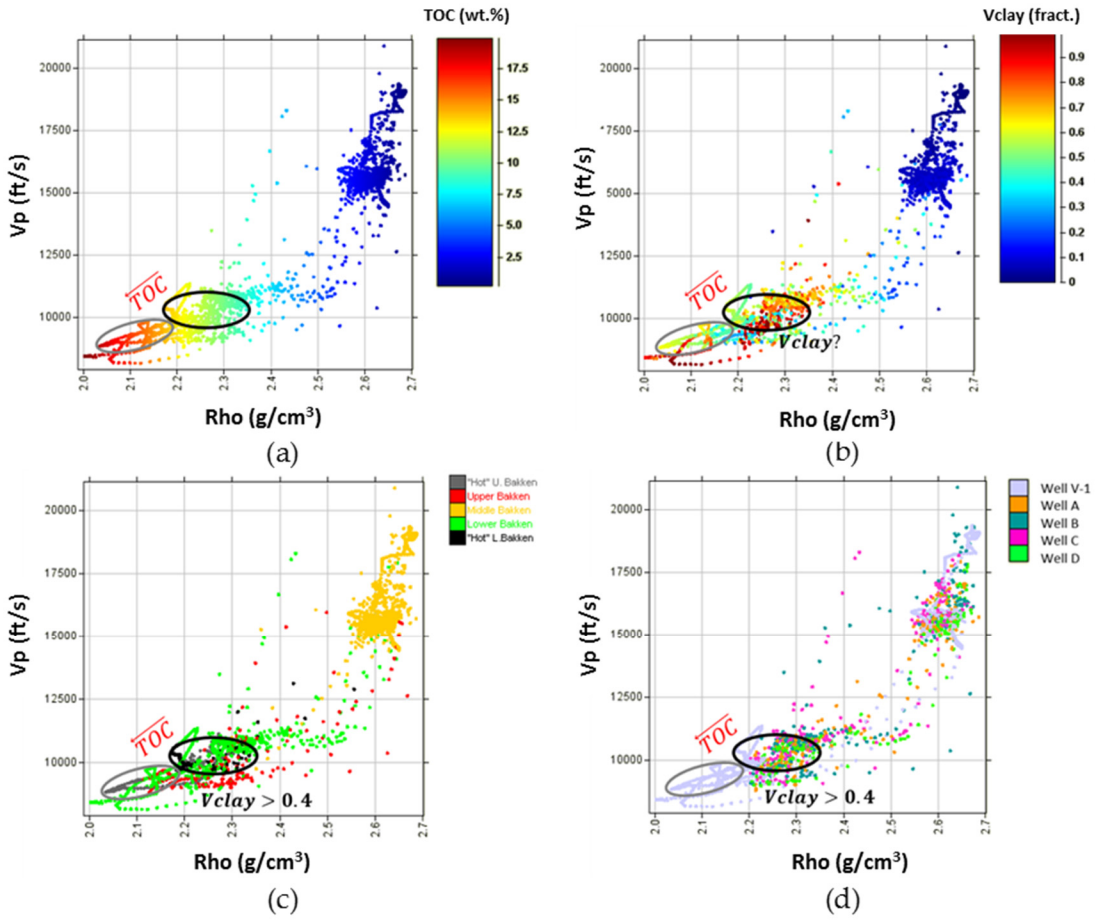

Figure 2.12: Density vs. Vp cross-plots for the Bakken Formation, including the wells A, B, C, D, and V-1. Cross-plots are color-coded by (a) TOC from Schmoker and Hester (1983), (b) Vclay, (c) unit and (d) well. The high-TOC interval correlates to low densities, high velocities, and variable clay content. The "hot" Upper and Lower Bakken Shales units are enclosed in the gray and black polygons of high TOC, respectively. Vp is a good lithological indicator for these two units, showing a general decrease in their values as clay content decreases. TOC seems to be the principal factor affecting changes in density and P-wave velocity in these wells.

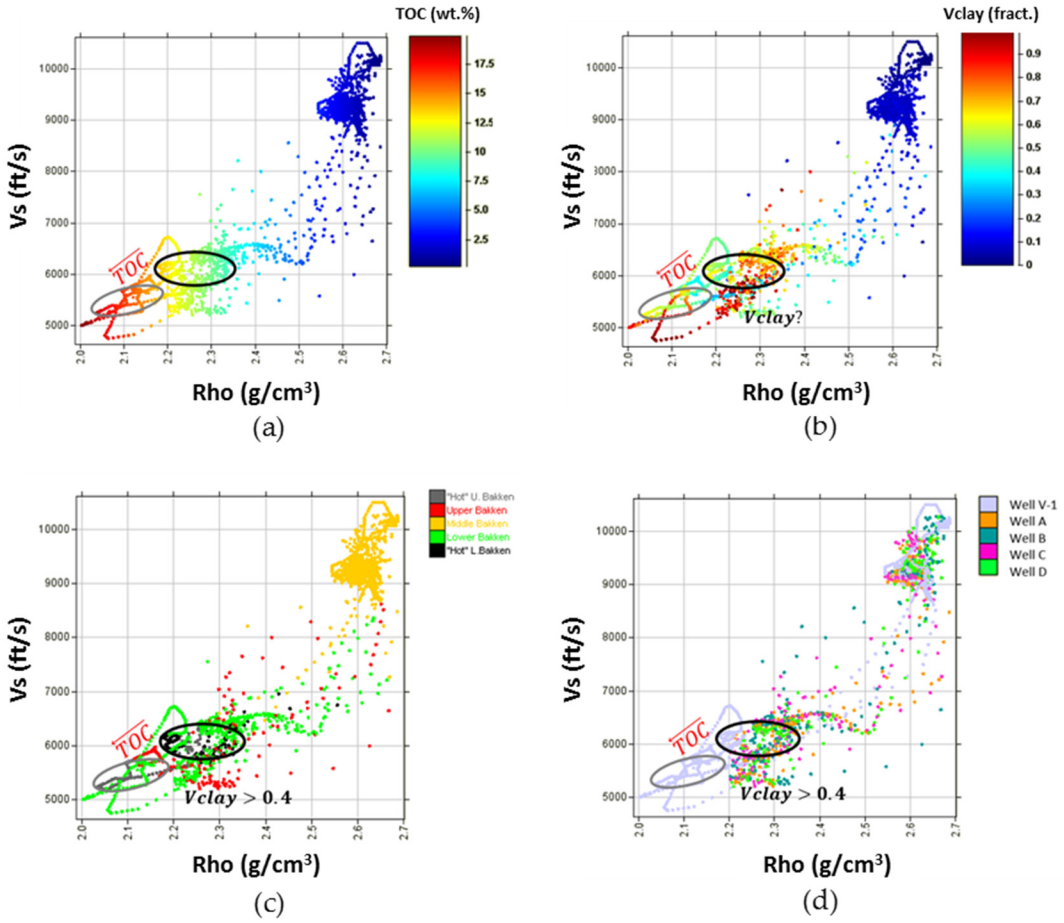

Figure 2.13: Density vs. Vs cross-plots for the Bakken Formation, including the wells A, B, C, D, and V-1. Cross-plots are color-coded by (a) TOC from Schmoker and Hester (1983), (b) Vclay, (c) unit and (d) well. The high-TOC interval correlates to low densities, high velocities, and variable clay content. The "hot" Upper and Lower Bakken Shales units are enclosed in the gray and black polygons of high TOC, respectively. Vs is a good lithological indicator for these two units, showing a general decrease in their values as clay content decreases. TOC seems to be the principal factor affecting changes in density and S-wave velocity in these wells.

Cross-plots between Vp/Vs and density for the five wells color-coded by TOC (Figure 2.14a), Vclay (2.14b), unit (2.14c), and well (2.14d) are shown in the Figure 2.14. Similarly to the previous case, TOC seems to be the principal factor affecting changes in density and the clay content does not appear to influence this property variation for the Bakken intervals. In this case, Vp/Vs does not clearly separate zones with TOC and shale content. Low Vp/Vs correlate to both organic-rich and organic-lean shales with high and low clay content. In the "hot" Lower Bakken, cutoff values or a proportional relation between density and clay volume cannot be defined. In the "hot" Upper Bakken where TOC is higher than 14 wt.% and density ranges between 2.00 g/cc and 2.15 g/cc, the general clay volume corresponds to values no lower than 0.5. This observation is made in general terms and cannot be taken as the exact response due to the uncertainty in the Vclay pattern within the interval. In all the five wells samples, these two "hot" units show Vp/Vs values between 1.65 - 1.75.

There is a directly proportional relation between density and acoustic impedance in the whole formation of interest (Figure 2.15) and even though the acoustic impedance cannot clearly discriminate between low and high clay content, AI seems to be a good lithological indicator. The cross-plot 2.15d shows that the "hot" Upper Bakken AI is lower than the "hot" Lower Bakken AI. These two units can be discriminated with a cutoff value of approximately 20,000 g/cc*ft/s. In general, the higher the TOC and shale/clay content, the lower the acoustic impedance.

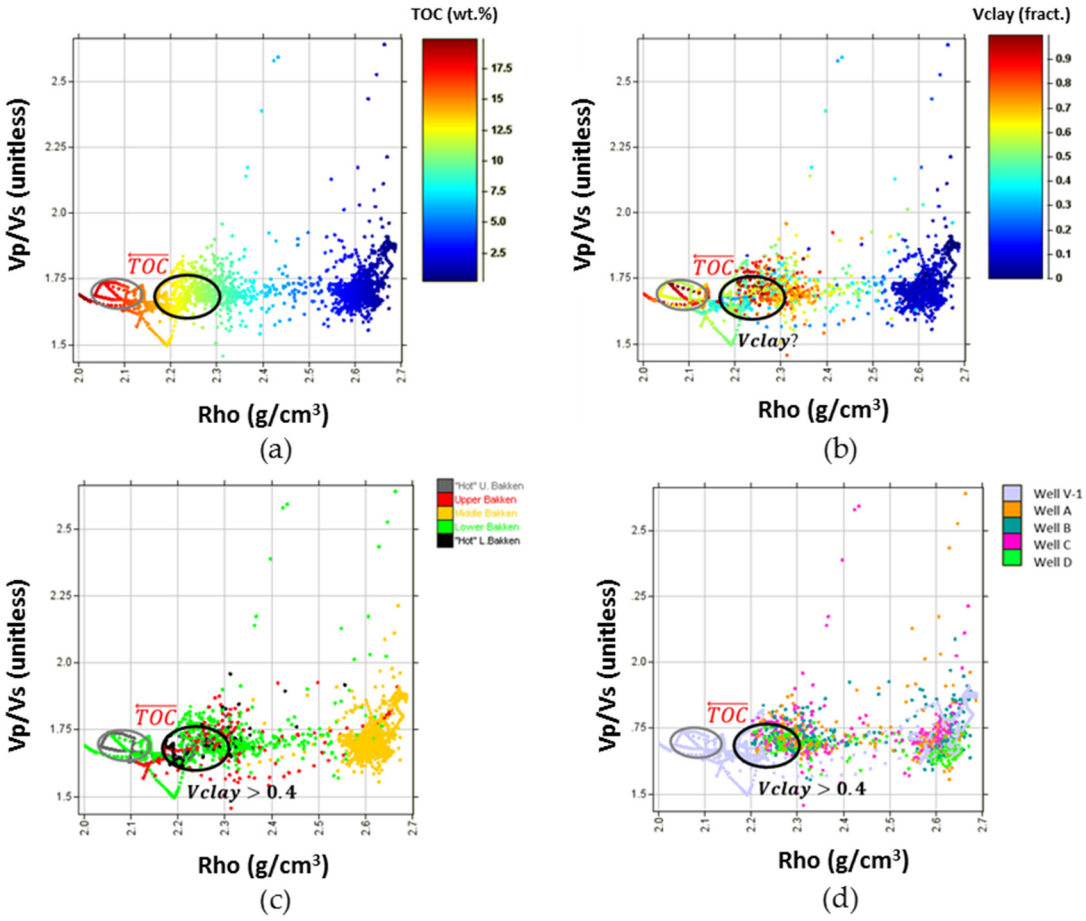

Figure 2.14: Density vs. Vp/Vs cross-plots for the Bakken Formation, including the wells A, B, C, D, and V-1. Cross-plots are color-coded by (a) TOC from Schmoker and Hester (1983) empirical method, (b) Vclay, (c) unit and (d) well. The high-TOC interval correlates to low densities and a Vp/Vs that ranges between 1.65 and 1.75. The "hot" Upper and Lower Bakken Shales units are enclosed in the gray and black polygons with TOC values higher than 14 wt.% and 10 wt.%, respectively.

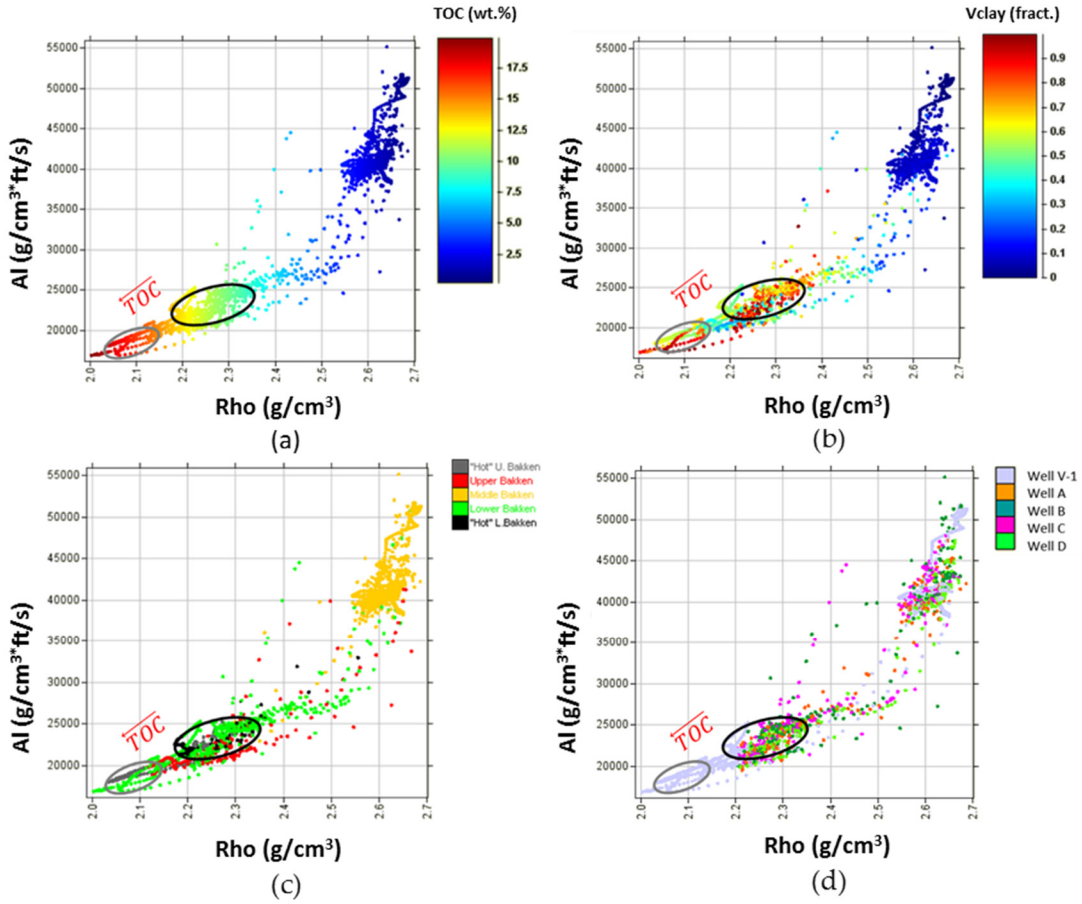

Figure 2.15: Density vs. acoustic impedance (AI) cross-plots for the Bakken Formation, including the wells A, B, C, D, and V-1. Cross-plots are color-coded by (a) TOC from Schmoker and Hester (1983) empirical method, (b) Vshale, (c) unit and (d) well. The high-TOC interval correlates to low densities, high velocities, and a high-clay content greater than 0.5. The "hot" Upper and Lower Bakken Shales units are enclosed in the gray and black polygons with TOC values higher than 14 wt.% and 10 wt.%, respectively. Acoustic impedance is also a good lithological indicator for these two units with a cutoff value of 20,000 g/cc*ft/s.

As expected, density seems to be a good indicator of lithology. Organic-rich matter rocks can also be identified in this domain, where a cutoff around 2.5 g/cc separate facies with low TOC content (< 7 wt.%) from facies with high TOC content (> higher 7 wt.%). A more restrained distinction can be found for the two ''hot" organic units in the Upper and Lower Bakken members (Table 2.3) defined by TOC values greater than 10 wt.% and densities between 2 – 2.15 g/cc (Upper Bakken unit), 2.2 – 2.3 g/cc (Lower Bakken unit).

Unit	TOC (wt. %)	Density (g/cc)
"Hot" Upper Bakken	14 – 16	2.00 – 2.15
"Hot" Lower Bakken	10 – 13	2.20 – 2.30

Table 2.3: TOC content and density ranges for the "hot" Upper Bakken and the "hot" Lower Bakken units. Note that the lower the density the larger the TOC content. The "hot" Upper Bakken unit shows a greater TOC content.

Cross-plots of AI vs. Poisson's ratio and LambdaRho vs. MuRho were generated for the Bakken Formation (Figure 2.16) color-coded by unit to test the feasibility of these domains in discriminating high TOC areas. Unfortunately, the high TOC "hot" Bakken shale intervals, cannot be identified in any of these domains indicating that the best attribute that could be used as an alternative for organic content assessment in the area of study is the inversion for density.

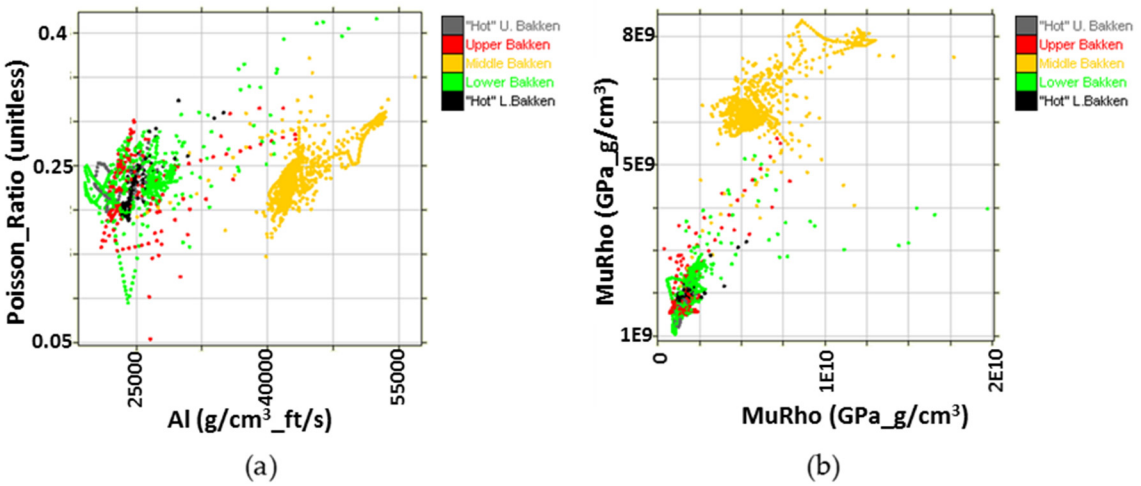

Figure 2.16: Acoustic impedance vs. Poisson's ratio (a), and $\lambda\rho$ vs. $\mu\rho$ (b) cross-plots of the Bakken Formation, colored by unit. Both "hot" Upper and Lower Bakken units (gray and black) cannot be easily discriminated in any of these domains.

2.4 Brittleness estimation

Finding areas in the shale play that are brittle is important in the development of a fracture fairway large enough to connect the highest amount of rock volume during the hydraulic fracturing process (Perez, 2014).

Based on the amount of plastic deformation that the rock undergoes before a fracture occurs, its response to stress can be differentiated between brittle and ductile. Brittle rocks can potentially generate microfractures that could remain open during hydraulic fracturing and therefore they tend to break easily. On the other hand, ductile

rocks absorb a high amount of energy before fracturing and as a consequence, they deform plastically (Ruiz, 2016).

The measure of stored energy before failure is a function of rock strength, lithology, texture, effective stress, temperature, fluid type, diagenesis and TOC and the analysis to differentiate brittle from ductile rocks has been key to stimulation process in shale oil and gas reservoirs where brittleness is mainly controlled by quartz content and ductility is controlled by clay, calcite, and total organic content (Perez, 2013).

Since the mineralogy of the Bakken shale members is mainly defined by quartz and clay, the response to stress could be difficult to associate directly to brittleness or ductility. Hence, the brittleness needs to be more accurately estimated and is calculated in both the wells, B and V-1 by a renormalization of Young's modulus (E) and Poisson's ratio (ν) over the zone of interest according to the Rickman et al., (2008) relation:

$$E_{BRIT} = \frac{E - E_{min}}{E_{max} - E_{min}} \tag{2.9}$$

$$\nu_{BRIT} = \frac{\nu - \nu_{min}}{\nu_{max} - \nu_{min}} \tag{2.10}$$

$$BI_{ave} = \frac{E_{BRIT} - \nu_{BRIT}}{2} \tag{2.11}$$

Where, E_{BRIT} = Normalized Young's modulus, ν_{BRIT} = Normalized Poisson's ratio, and BI_{ave} = Average brittleness index.

Since the average brittleness is defined by a subjective and arbitrary renormalization process with defined upper and lower E and ν bounds of 835, 114 and 0.363, 0.095, respectively. It only provides relative information and it should be compared and correlated with an estimation using fractions of brittle minerals or other attributes such the product of Young's modulus and density $E\rho$. Sharma and Chopra (2015) suggest that $E\rho$ accentuates lithology detection in terms of brittleness and could be useful for the determination of E from seismic data by way of inversion. In this sense, impedance inversion of seismic data takes place using the resulting P and S-impedances to determine $E\rho$ without the requirement of density which is difficult to derive from seismic data unless long offset information is available.

Figure 2.17a shows the cross-plot of Poisson's ratio versus E that is generated to pick out brittle-shale zones defined by low Poisson's ratio and high Young's modulus (red rectangle). Note the similarity between both ν vs. E and ν vs. $E\rho$ which facilitates a new domain $E\rho/\nu$ and suggest that templates of $E\rho$ versus Poisson's ratio can be used as well in engineering and geophysical workflows.

The comparison of the brittleness indices derived using Rickman's approach and using $E\rho/\nu$ for the wells B and V-1 is shown in the Figure 2.18. Even though the scales are different, the curves show similar trends of increasing brittleness towards the base of the Upper and Lower Bakken. The similarity between the curves is higher for the well B.

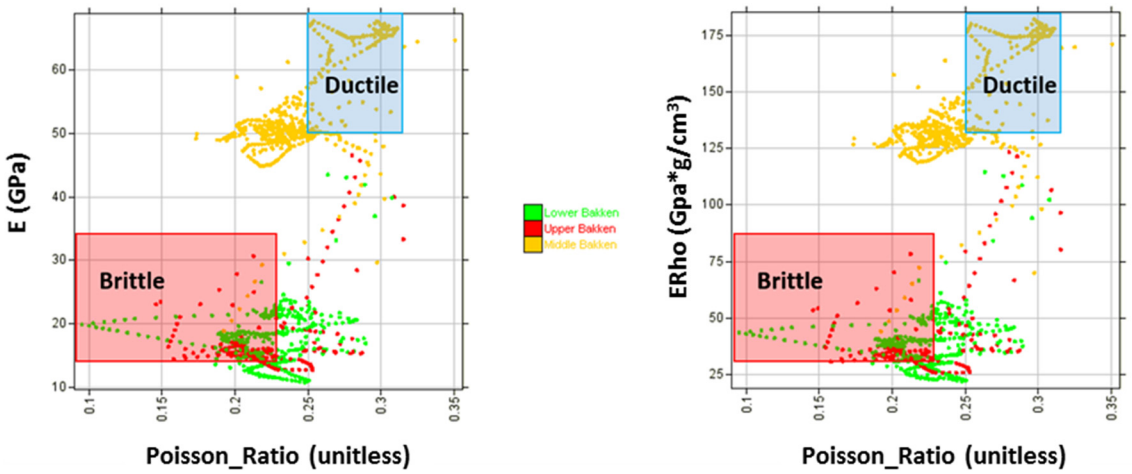

(a) (b)

Figure 2.17: Poisson's ratio vs. E (a), and Poisson's ratio vs. Eϱ (b) cross-plots of the Bakken Formation colored by unit. Notice the similarity between cluster points. A new domain $E\rho/\nu$ can be used as a brittleness indicator for the Bakken shale members. Brittle-shale zones and high-ductile zones in the red and blue rectangles, respectively. The Lower Bakken is generally less brittle than the Upper Bakken and the Middle Bakken shows points with moderate brittleness.

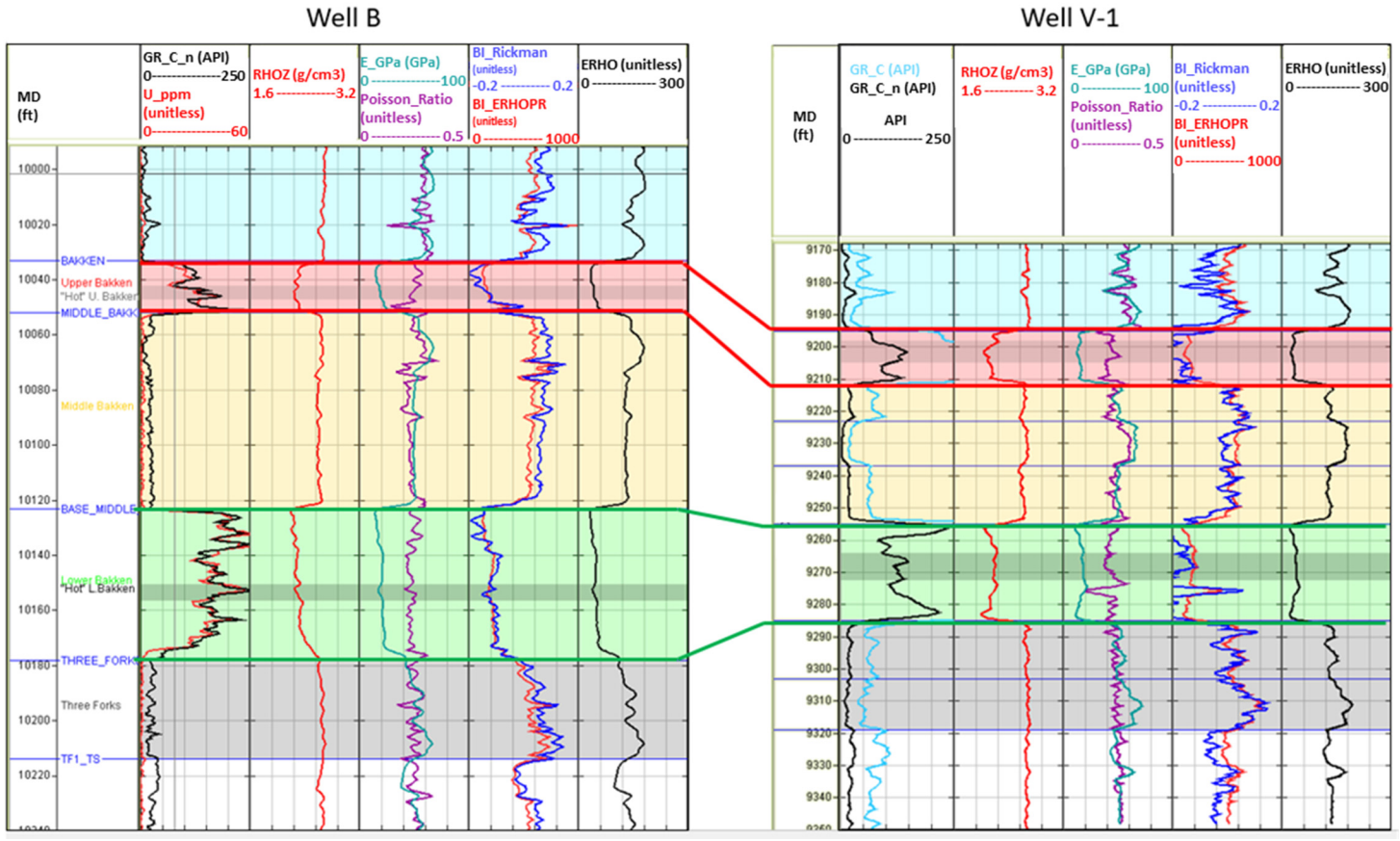

Figure 2.18: Well section through Well B and Well V-1, showing a comparison between the brittleness indexes (fourth track) derived using Rickman's formulation (blue curve) and $E\rho/\nu$ (red curve). The fifth track shows the $E\rho$ calculation for reference.

Figure 2.19 shows a comparison between the Well B and Well V-1 logs. From left to right, gamma-ray, uranium, mineral volumes, density, TOC and total porosity, P and S-wave velocities, P and S-wave impedances, and Vp/Vs. The vertical well V-1 presents the neutron porosity and a water saturation log was calculated using the deep resistivity log available assuming an oil saturation of 75%. The well section is colored by the previously defined working intervals. In general, The Upper and Lower Bakken show high clay content (0.3 to 0.6), high total porosities (20 to 35%), and high TOC content (10 to around 17 wt. %). The high density-porosity log does not imply matrix porosities in the 30% range. Rather, this density-log response is due primarily to organic-matter which, with a specific gravity near 1.0 g/cm^3, is sensed by the density log as "porosity" (Schmoker and Hester, 1983). In these shale members, uranium associated with organic-matter is the principal cause of the high gamma-ray intensity (Schmoker, 1981). The low TOC part of the Upper Bakken member is more brittle showing that not only its brittle mineral content (e.g., quartz) but its low TOC, enhances its hydro-fracturing potential.

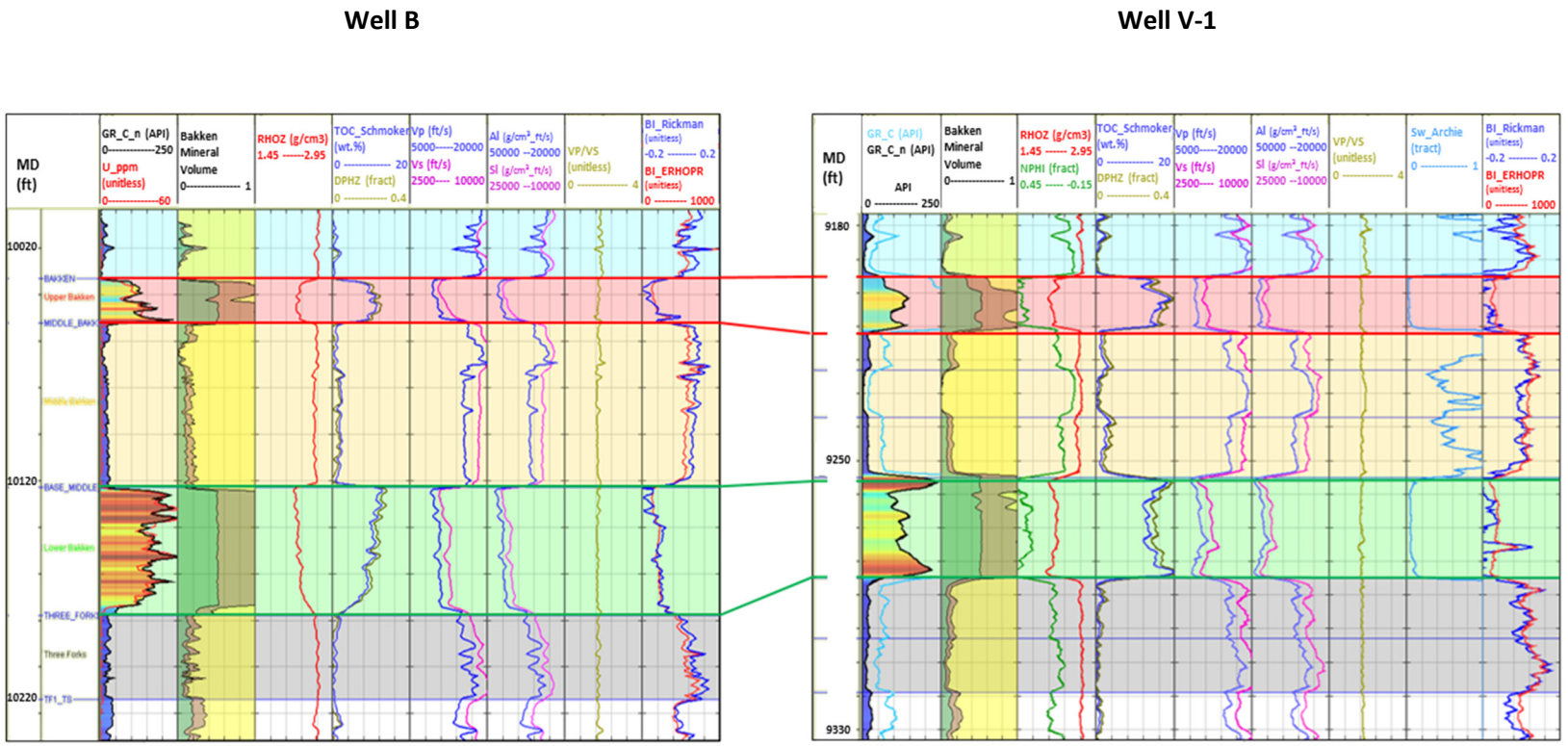

Figure 2.19: Comparison between Well B and Well V-1 logs. From left to right, gamma-ray, uranium, mineral volumes (Shale in green, clay in brown, and quartz in yellow), density, TOC and total porosity, P and S-wave velocities, P and S-wave impedances, and Vp/Vs. Both the Upper and Lower Bakken show high clay content, high total porosities, and high TOC content. Upper Bakken has more brittle material content (e.g., quartz) than Lower Bakken and it could be more prone to open and maintain fractures during hydraulic fracturing.

Chapter 3

AVO seismic modeling and fluid substitution

Anisotropy generally affects wave propagation of both P and S waves in shales (Tsvankin, 2001), therefore it cannot be ignored when understanding, predicting, and evaluating seismic amplitude responses. AVO modeling is performed in the wells A and V-1 to understand the acoustic and elastic modeling differences and the amplitude behavior in the compressional and shear-wave domain. The estimation of rock physics properties in the intervals of interest is undertaken by defining sets of volume fractions, fluids, saturations, and minerals. Empirical Vp-Vs relations and $\varepsilon - \gamma - \delta$ anisotropic parameters are derived for the Lodgepole, Bakken, and Three Forks Formations. The effects of fluid substitutions on the log data and synthetic gathers are also modeled.

3.1 Interval properties from log data

The estimation of the rock physics properties in the intervals of interest is performed in four ways in the vertical wells A and V-1 by creating sets of volume fractions, fluids, saturations, and minerals. Within a volume fraction set, a volume log is associated with a mineral, thus describing the composition of the matrix. For both vertical wells, their Vshale and Vclay volume logs previously calculated in the second chapter, are used as shale and dry clay logs, respectively. A complimentary log associated with quartz is also created and normalized to ensure that the total volume adds up to one at any given depth.

On the other hand, fluid log sets are calculated for the Middle Bakken reservoir using the FLAG 2014 models from the University of Houston Fluid/DHI Consortium to take into account the fluid properties change with depth. Hence, a temperature and pressure gradient, together with various, water, oil and gas fluid constants are used to calculate a log of Bulk Modulus (K) and density (Rho). According to Meissner (1991), the hydrocarbon source-rock bodies comprising the Upper and Lower Bakken shale units are mature in the deeper portions of the Williston Basin where they have been exposed to maximum burial-related temperatures of about 165 °F (73.89 °C). The reservoir pressure gradient is assumed to be 0.55 psi/ft. (Havens, 2012), which corresponds to approximately 5100 psi (35.16 MPa) of pressure in the middle Bakken. The gas to oil ratio, oil API, and gas gravity are considered as 1200 scf/bbl, 42 API, and 0.65, respectively (from

ConocoPhillips Report 2010). The calculated densities, velocities, and Bulk moduli of the reservoir fluids are specified in Table 3.1.

Fluid Type	ρ (g/cc)	Vp (ft/s)	K (GPa)
Water	1.06	5,612.75	3.09
Oil	0.61	3,175.58	0.57
Gas	0.23	2,108.12	0.09

Table 3.1: Densities, velocities, and Bulk moduli of fluids calculated for the middle Bakken member using the FLAG 2014 models (Han et al., 2014).

On the other hand, saturation logs are grouped together to provide a complete fluid description in terms of water, oil, and gas content. The water saturation is calculated for the Well V-1 using the deep resistivity log and the effective porosity log. 75% of oil saturation is assumed to be constant for the three formations of interest and the complementary gas saturation log is created and normalized to ensure that the total fluids add up to one (Figure 3.1).

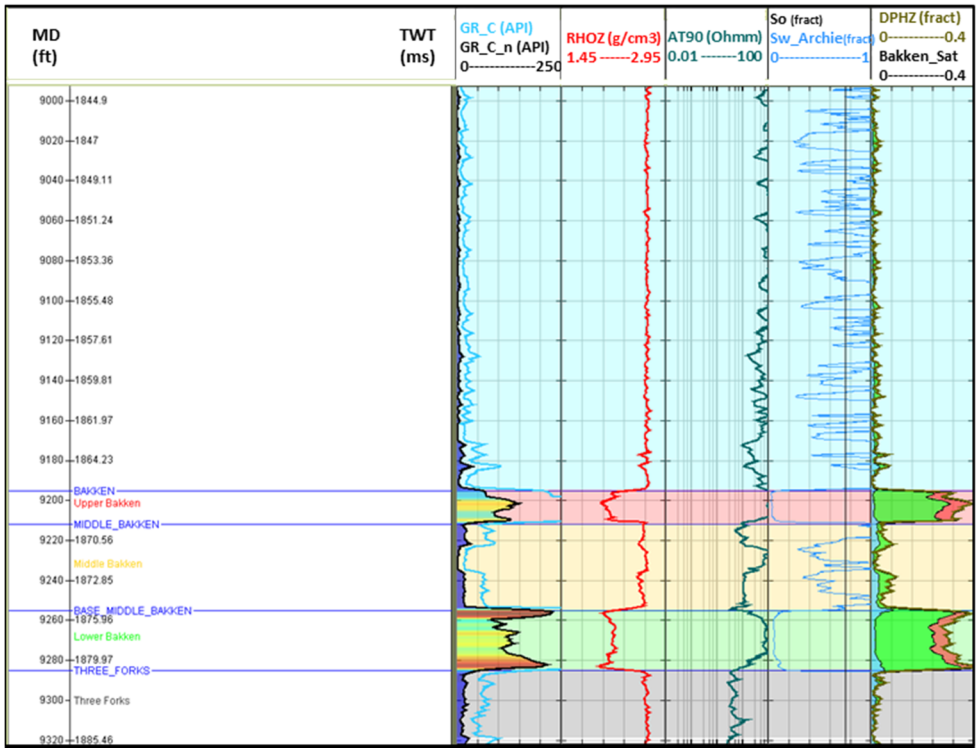

Figure 3.1: Estimation of the saturation curves and set for Well V-1. From left to right, total and normalized GR colored by Vshale, density, deep resistivity, oil and water saturation, and the density porosity log colored by the initial fluid saturation. Water saturation (in blue), oil saturation (in green) and gas saturation (in red).

In rock physics terms, S-wave velocity plays an important role in lithology determination, fluid indication, and seismic modeling. On the one hand, it gives a measure of the rigidity of the rock, as it is unaffected by fluid type (i.e. fluids do not shear). On the other hand, its relation with the P-wave velocity is commonly used as a fluid indicator. As the fluid becomes lighter, density decreases which results in a higher value for Vs. Furthermore, S-wave information is required for calculating the offset or angle

reflectivity. Given its relevant uses, empirical relationships between Vp and Vs such as the Greenberg & Castagna (1992) in multimineralic rocks permits the conversion from one velocity to the other in reservoirs and intervals of interest. In this study, measured Vp and Vs values from the vertical well V-1 (Figures 3.2 and 3.3) are used to calibrate the Greenberg-Castagna equation associated with the main lithology at each of the five zones of interest (Table 3.2). In Figure 3.2a, the Vp vs. Vs cross-plot of the shale members of the Bakken Formation is compared with the Vp-Vs regression line for all the velocity data in the Well V-1 (G/C Bakken – blue line).

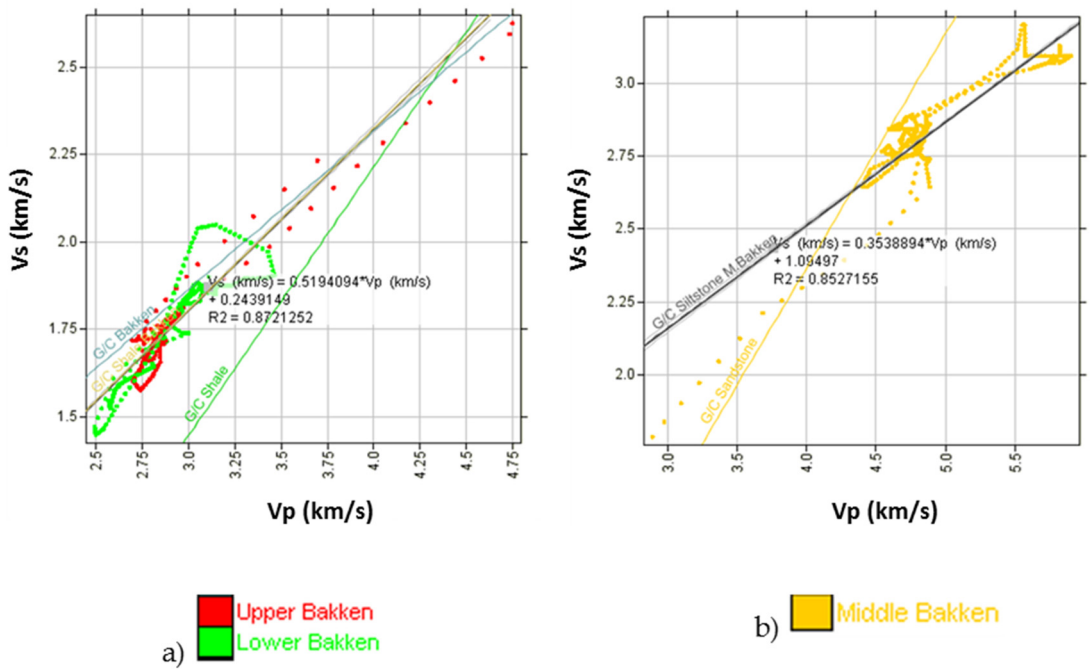

Figure 3.2: Vp vs. Vs cross-plots for Well V-1 color-coded by a) Upper and Lower Bakken members and b) middle Bakken member. The cross-plots are used to calibrate the Greenberg-Castagna relation for shales (green line) and sandstones (yellow line).

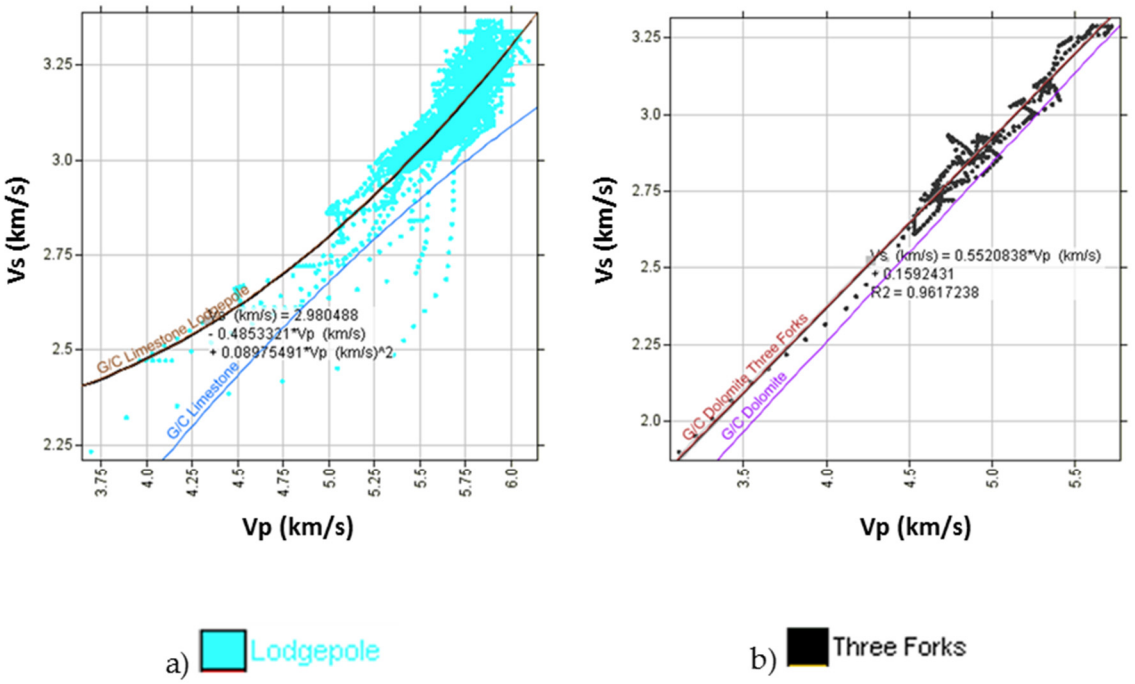

Figure 3.3: Vp vs. Vs cross-plots for Well V-1 color-coded by a) Lodgepole Formation and b) Three Forks Formation. The cross-plots are used to calibrate the Greenberg-Castagna polynomial and lineal regressions for limestones (blue line) and dolomites (purple line).

Formation / Member		**Main Lithology**	**Calibrated Greenberg-Castagna Relation (in Km/s)**
Lodgepole		Limestone	$Vs = 2.98 - 0.485 * Vp + 0.09 * Vp^2$
Bakken	Upper and Lower Bakken	Shale	$Vs = 0.519 * Vp + 0.244$
	Middle Bakken	Siltstone	$Vs = 0.354 * Vp + 1.095$
Three Forks		Dolomite	$Vs = 0.552 * Vp + 0.159$

Table 3.2: Calibrated Greenberg-Castagna empirical Vp-Vs relations for the Lodgepole, Bakken, and Three Forks Formations using the log data from Well V-1.

To get a representative average of the interval Vp, Vs and density properties from our log data (Tables 3.3 and 3.4), cross-plot analyses and cut-offs of Vclay < 0.3 and Vclay > 0.3 are applied to the three working intervals of the Bakken Formation, to exclude shale points from the sand/siltstone interval (Middle Bakken), and sand points from the shale intervals (Upper and Lower Bakken).

Formation / Member		**Vp (ft/s)**	**Vs (ft/s)**	**ρ (g/cc)**
Lodgepole		16,608.865	10,232.181	2.685
Bakken	Upper	9,295.487	5,645.331	2.131
	Middle	16,513.167	9,435.445	2.626
	Lower	9,729.524	5,870.239	2.166
Three Forks		16,212.917	9,473.34	2.668

Table 3.3: Mean Vp, Vs, and density values for the Lodgepole, Bakken, and Three Forks Formations. These values are calculated from Well V-1.

Formation / Member		**Vp (ft/s)**	**Vs (ft/s)**	**ρ (g/cc)**
Lodgepole		18,822.232	10,272.043	2.687
Bakken	Upper	10,059.016	5,824.049	2.290
	Middle	15,645.288	9,097.364	2.600
	Lower	10,579.737	6,206.643	2.326
Three Forks		15,996.451	8,929.599	2.650

Table 3.4: Mean Vp, Vs, and density values for the Lodgepole, Bakken, and Three Forks Formations. These values are calculated from Well A.

A large number of elastic quantities control the propagation of seismic waves through materials. By taking into account symmetry properties, as well as by realizing that anisotropy is normally relatively weak, Thomsen (1986) determined a set of five parameters required to define wave motion in VTI, HTI or orthorhombic media: vertical P-wave and S-wave velocities, Epsilon (ε), Gamma (γ), and Delta (δ). The last three dimensionless parameters describe the variation in P-wave velocity, the variation in S-wave velocity, and the relationship between the two velocities, respectively.

For the purpose of this study, an initial derivation of the anisotropic parameters of the formations of interest is performed using the Havens (2012) formulations. From various existing approaches for Thomsen's parameters, Vernik and Liu (1997) and Huang (2016) values are reported to compare the results of the anisotropic estimations in the Bakken shale members. Weak-anisotropy components C_{33}, C_{44}, C_{55}, C_{66}, and Gamma (γ) values for the Well A are available for this study, and will be used in the calibration of the estimated anisotropic parameters for the Well V-1 in the Bakken and its overlying / underlying formations.

Table 3.5 cites the core sample measurements of the Bakken shales performed under dry conditions (Vernik and Liu, 1997), showing a VTI anisotropy with Epsilon (ε) ranging from 0.19 to 0.51, Gamma (γ) ranging from 0.16 to 0.59, and Delta (δ) ranging from 0.02 to 0.30.

Depth (ft)	Epsilon (ε)	Gamma (γ)	Delta (δ)
8,634	0.44	0.51	0.03
9,831	0.24	0.24	0.12
10,164	0.27	0.23	0.04
10,733	0.39	0.27	0.08
10,734	0.29	0.42	0.18
10,931	0.51	0.59	0.30
11,230	0.20	0.17	0.02
11,246	0.19	0.16	0.03
11,280	0.26	0.18	0.13
Average Variation	0.31 - 0.11	0.31 – 0.16	0.10 – 0.09

Table 3.5: Laboratory measurements of anisotropy parameters on the dry samples from Bakken shales with 70 MPa of confining pressure. From Vernik and Liu (1997), and Huang (2016).

After processing the zero-offset, walk-away and walk-around VSP data in the Bakken shale provided by Hess Corporation, Huang (2016) found that there is strong polar anisotropy in evidence from the VSP data in the Lodgepole and Bakken Formations, and Thomsen's anisotropic parameters for the Bakken Formation agree with the core sample measurements and are estimated to be 0.27 for ε, and 0.07 for δ.

Havens (2012) reports laboratory measurements on dry samples that provide trends amongst the anisotropy parameters for both the shales and the middle Bakken. Based on the assumption that none of the middle Bakken member, Lodgepole, and Three Forks Formations contain intrinsic anisotropy, a single trend is applied based on $\gamma - \varepsilon$ and ε - δ trends as follows:

$$\varepsilon = 2.04\gamma^{1.09} \quad 3.1$$

$$\delta = 6.14\varepsilon^{1.87} \quad 3.2$$

Based on the Vernik and Nur (1992) anisotropic parameters of black shales dataset, assuming that the γ values are all positive, and after a modification of Thomsen's δ parameter that resulted to be a stronger correlation with the ε anisotropy parameter according to Havens (2012) study, the corresponding relationships for the Bakken shale members are given by:

$$\varepsilon = 0.71\gamma^{0.69} \quad 3.3$$

$$\delta = 0.43\varepsilon^{0.82} \quad 3.4$$

Havens (2012) equations 3.1 – 3.4 are applied for the estimation of the ε and δ values using the γ log available of the Well A (Figure 3.4). Over the area of interest, the dipole sonic log showed $C_{44} \approx C_{55}$ suggesting a VTI model, in which the axis of symmetry is

parallel to the vertical direction, is sufficient for studying the anisotropy system for the Bakken Shale in the vicinities of the available wells.

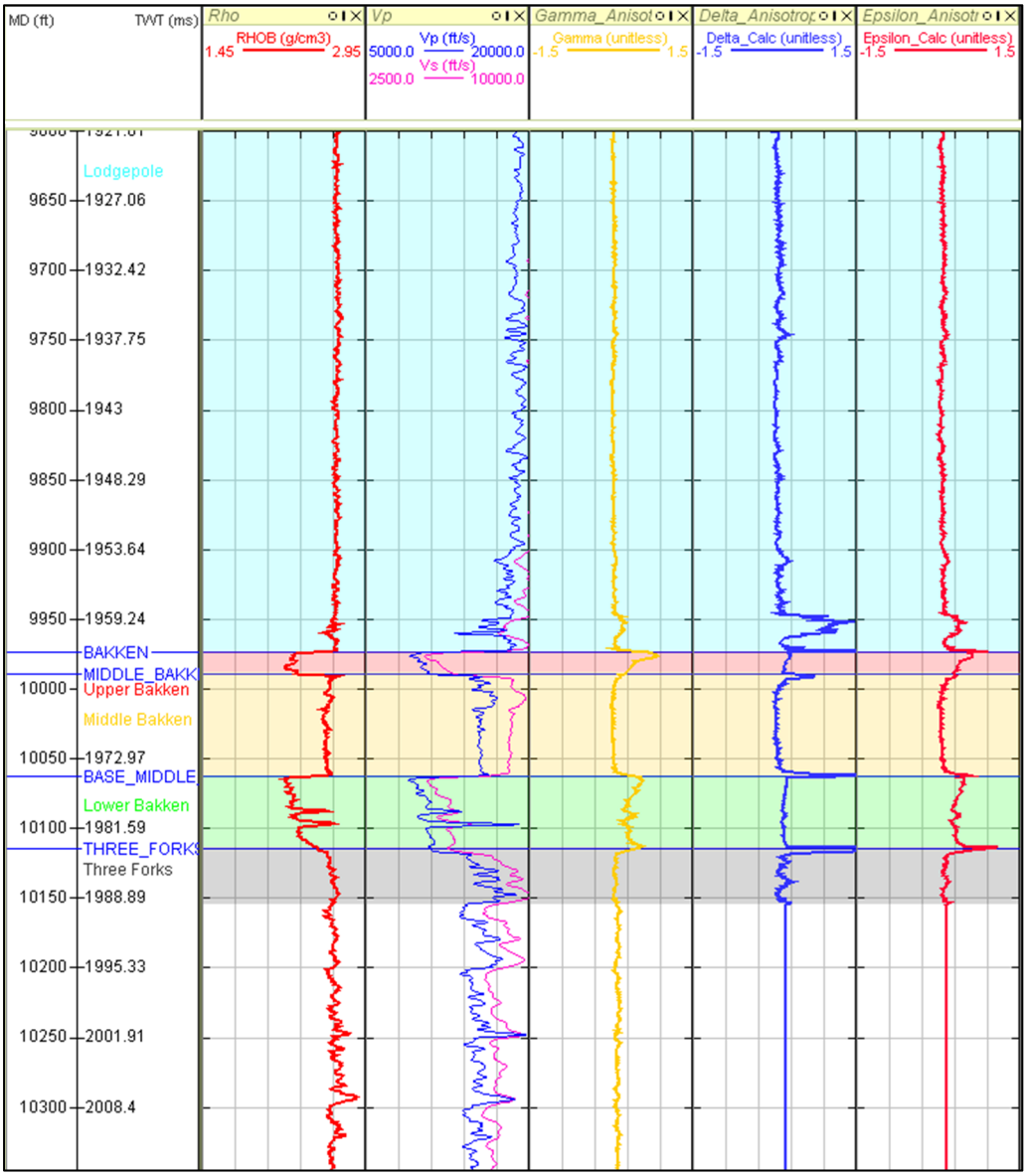

Figure 3.4: Estimation of δ and ε curves for Well A. From left to right, density, Vp and Vs, γ log provided by Hess Corporation, and the δ and ε logs estimated through Havens (2012) formulations.

Table 3.6 shows a representative average of the interval ε, γ and δ properties from our log data. The tabulated values will then be used for building the log anisotropy model in the vertical well V-1 and its associated AVO seismic modeling.

Formation / Member		**Epsilon (ε)**	**Gamma (γ)**	**Delta (δ)**
Lodgepole		0.100	0.062	0.099
Bakken	Upper	0.450	0.530	0.220
	Middle	0.081	0.051	0.067
	Lower	0.370	0.390	0.190
Three Forks		0.135	0.083	0.155

Table 3.6: Mean ε, γ and δ values for the Lodgepole, Bakken and Three Forks Formations. These values are calculated from log data of Well A.

In the Bakken Formation, the calculated ε average of 0.30 agrees with the measurements on core samples (Vernik and Liu, 1997) and the VSP processing results (Huang, 2016). On the other hand, an increase of 0.09 units with respect to the Huang (2016) δ average could be associated with high peak δ log values at the top and base of the three members of the Bakken Formation (Figure 3.4). In addition, according to the Havens (2012) study, the empirical ε - δ relations has been extrapolated from laboratory data, they disregard the possibility of Biot's coefficients less than unit, and are derived from a modification of Thomsen's δ parameter which suggest a level of uncertainty even when the modifications of δ resulted to be a stronger correlation with the ε anisotropy

parameter. However, the results appear to be more reliable and agree with the reported δ values for the middle Bakken member and both the Lodgepole and Three Forks formations with $\delta \sim 0$ (Havens, 2012).

3.2 AVO seismic modeling

Seismic anisotropy can be defined as the variation of seismic velocity with the angle in which the ray path travels that is attributable to the presence of fractures and cracks and/or layering of different lithologies or minerals. In this study, to enable the anisotropy to be assigned on a log sample-by-sample basis, a set of ε, γ, and δ logs is built based on the constant values previously estimated and together with corrected Vp-Vs-Rho sets, it can then be used in the AVO synthetic generation process to compute PP and PS seismograms for both wells, A and V-I.

The anisotropy model makes geometrical corrections to the velocities due to both the deviation of the well and the dipping of any horizontal layering. Hence, a new set of vertically corrected Vp and Vs logs is obtained from the $\varepsilon - \gamma - \delta$ values, strike data and the well trajectory information. The calculations are done assuming the dip and azimuth angles of the shale bed for pure VTI to be 69° and 75°respectively, according to Yang and Zoback (2014) in their study of the preexisting fractures and faults in the Bakken Formation.

PP pre-stack offset gathers are calculated using a 45 Hz Ricker Wavelet of 2 ms of sample interval and the Backus-averaged velocities and density logs using a 50 ft window for averaging to model a more homogeneous representation of the logs that might adapt better to the actual seismic response. All synthetic seismograms are generated in Hampson-Russell software by a ray-trace modeling code using the anisotropic version of Zoeppritz with reflectivity formulations from Tsvankin and Thomsen (1994), and Ruger (2002). The seismic polarity for the synthetics was normal polarity which means a peak in seismic traces corresponds to a positive reflection coefficient (an increase in acoustic impedance).

Figures 3.5 to 3.8 show for both wells, their respective ρ log, and their corresponding vertically corrected velocities and Backus – averaged logs, the previously calculated $\varepsilon - \gamma - \delta$ logs, and two PP and PS synthetic seismograms using the corrected Vp, Vs, density logs, and their Backus average, respectively.

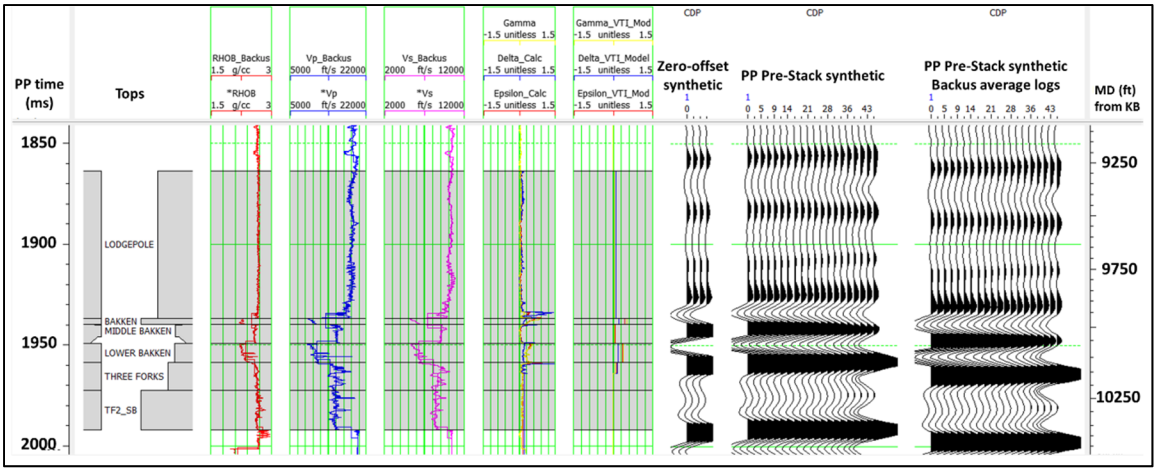

Figure 3.5: PP pre-stack synthetic seismograms for Well A. From left to right, corrected and Backus-averaged density, Vp and Vs logs, calculated and modeled Thomsen's parameters logs, repeated synthetic traces at zero-offset, PP synthetic seismograms using the Vp log and its respective Backus average.

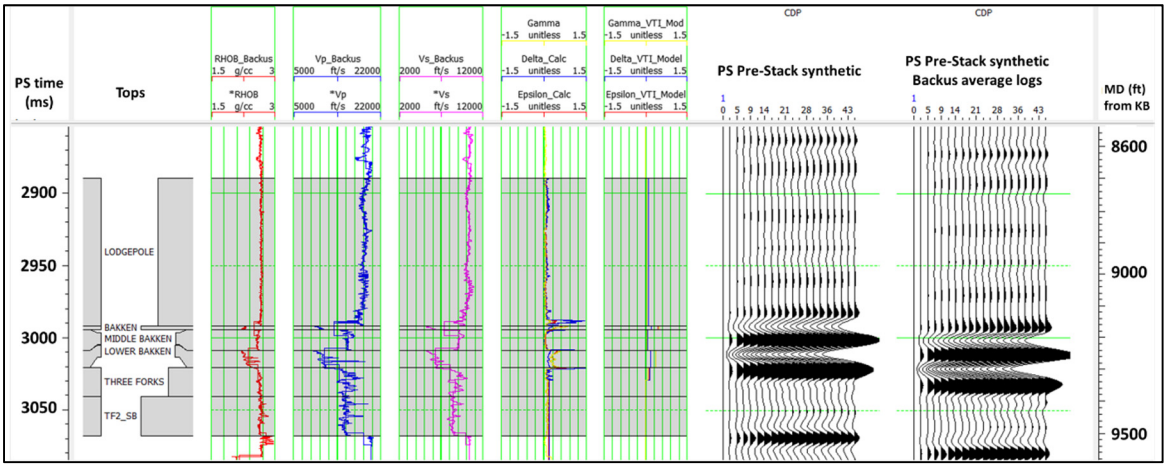

Figure 3.6: PS synthetic seismograms for Well A. From left to right, corrected and Backus-averaged density, Vp and Vs logs, calculated and modeled Thomsen's parameters logs, PS synthetic seismograms using the Vs log and its respective Backus average.

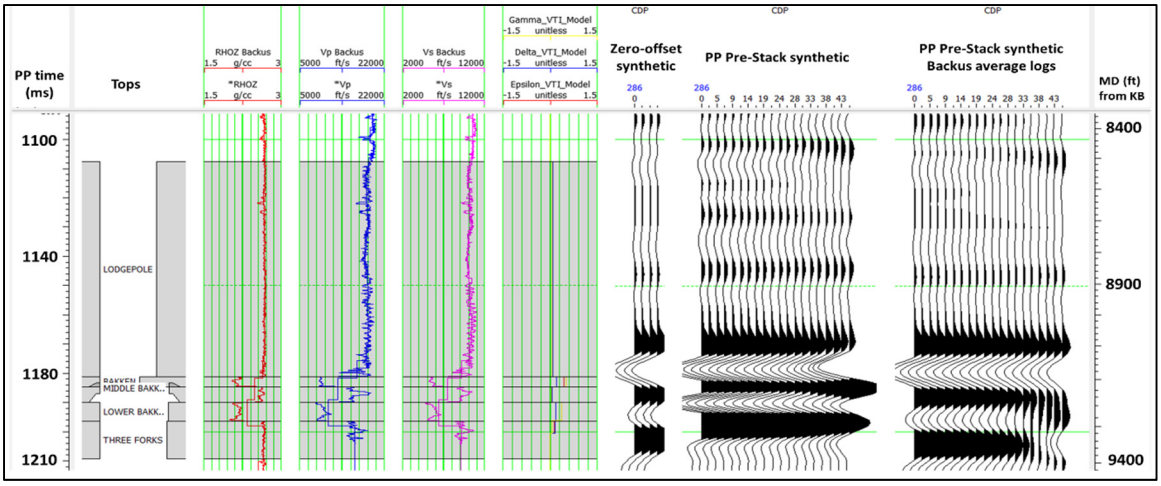

Figure 3.7: PP pre-stack synthetic seismograms for Well V-1. From left to right, corrected and Backus-averaged density Vp and Vs logs, VTI modeled Thomsen's parameters logs, repeated synthetic traces at zero-offset, PP synthetic seismograms using the Vp log and its respective Backus average.

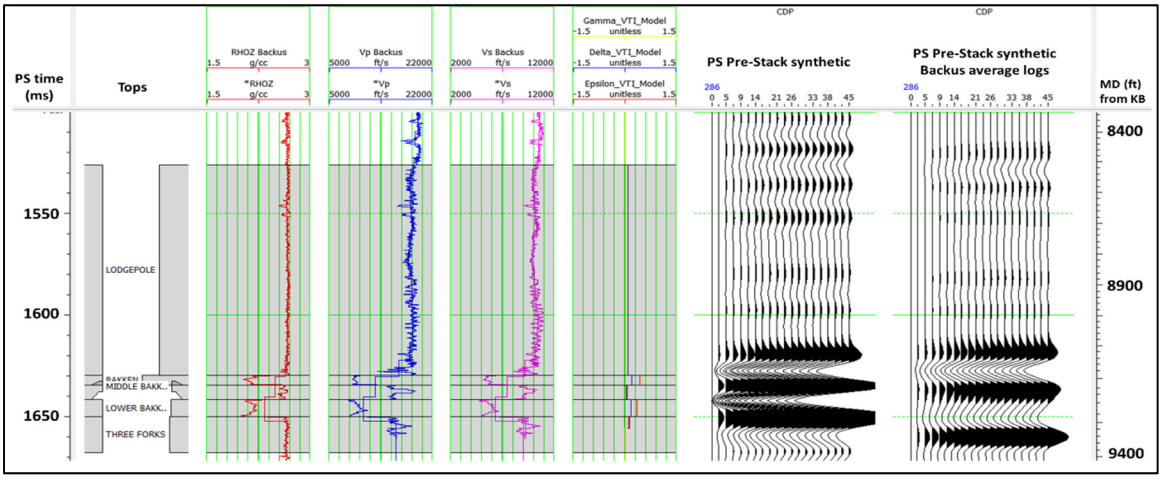

Figure 3.8: PS synthetic seismograms for Well V-1. From left to right, corrected and Backus-averaged density Vp and Vs logs, VTI modeled Thomsen's parameters logs, PS synthetic seismograms using the Vs log and its respective Backus average.

These synthetic seismograms are modeled with and without Backus averaging. Note the effect in the resolution of the tops of interest and the AVO response differences. In both wells, The Backus synthetic seismograms show what appears to be the same seismic response as the original synthetic but with a delay in time of about 5 ms. The seismic resolution does not appear to be compromised. In both cases, the reservoir tops of Middle Bakken, and Three Forks Formation can be detected with a 45 Hz wavelet convolved with the respective reflectivity series of both wells. This observation will be compared further to new synthetic seismic generated and the actual seismic data after well log correlations, statistical wavelet extraction and seismic to well ties in chapter 4.

AVO modeling is affected by transverse anisotropy causing a change in reflectivity and shape modification of the incident wave front. The Thomsen's dimensionless anisotropic parameters δ and ε can be used to predict AVO effects from anisotropy (Thomsen, 1986). For simple models, when $\delta>0$ or $\varepsilon>0$, AVO effects decrease and when $\delta<0$ or $\varepsilon<0$, AVO effects increase. However, the incident wave front shape can be significantly affected too. Because the wave travels faster in either the vertical or the horizontal direction, the plane wave has different travel times and incidence angles for anisotropic layers and for the Zoeppritz modeling that calculates plane wave propagation, the reflection coefficient decreases because of anisotropic effects, increasing the AVO effect (Hampson and Russell., 1999). This increase of amplitude with offset that can be associated with anisotropy can be observed as well in the PP synthetic seismograms at depths of Middle Bakken and Three Forks Formations.

Figures 3.9 and 3.10 show the AVA response picked at the Upper and Lower Bakken troughs (negative amplitude) in the well V-1. The red curve corresponds to the amplitudes picked in the PP synthetics generated for the well V-1. These amplitudes were fitted using the three-term Aki-Richards approximation of the Zoeppritz equations to help us determine the class of the AVO anomaly. Coefficients values are shown in Table 3.7. In both curves note how the amplitude becomes less negative with offset showing a negative intercept and a positive gradient caused by a low-impedance rock below a hard cap rock. This anomaly corresponds to an AVO Class IV classified by Castagna and Swan (1997) and it is also reported in computed half-space AVA models for the tops of other U.S. shales such as Eagle Ford, Barnett Shale and Marcellus Shale in Vernik and Khadeeva (2013), Yenugu and Han (2013) and Ruiz (2016), respectively. For the top of Upper Bakken, the amplitude increases with offset and starts to increase at approximately 30° where the Aki-Richards approximation is no longer valid.

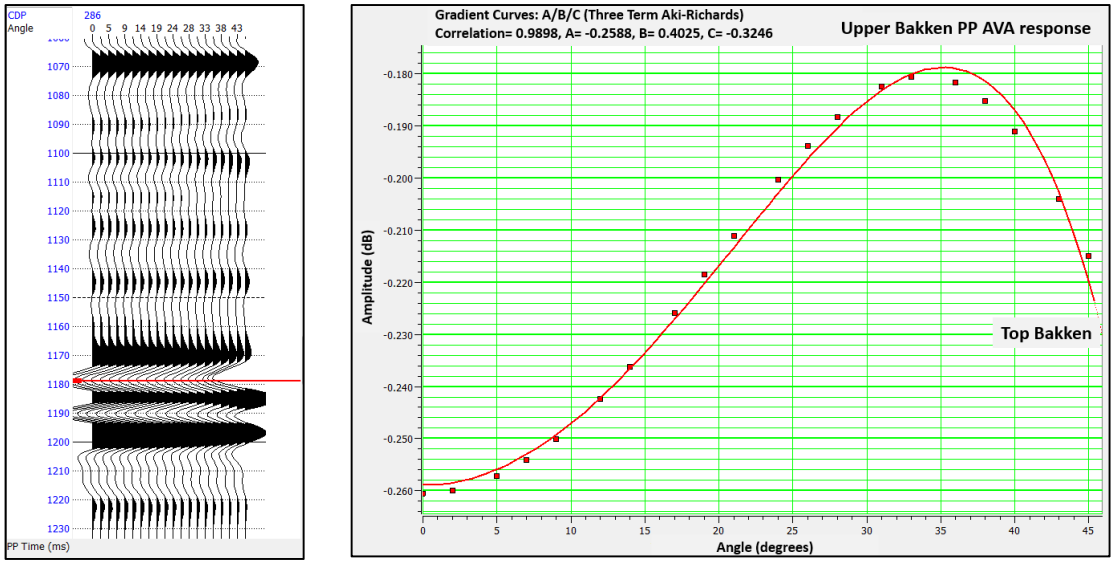

a) PP Pre-stack synthetic

b) Upper Bakken PP AVA response

Figure 3.9: PP AVA response for the top of the Upper Bakken. The negative intercept and positive gradient correspond to an AVO Class IV.

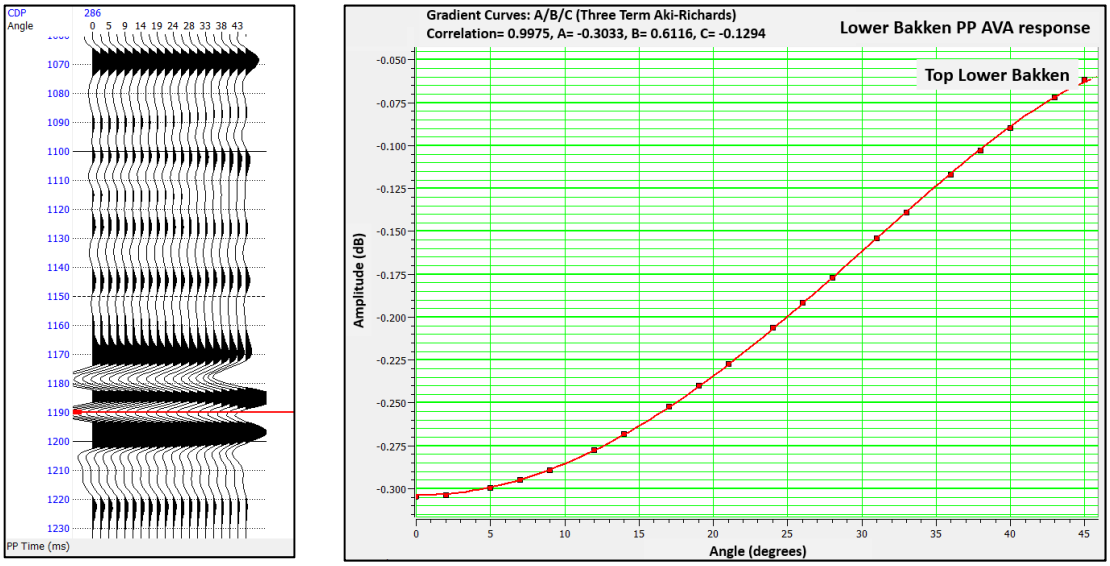

a) PP Pre-stack synthetic

b) Lower Bakken PP AVA response

Figure 3.10: PP AVA response for the top of the Lower Bakken. The negative intercept and positive gradient correspond to an AVO Class IV.

Top of Shale	Intercept (A)	Gradient (B)	Curvature (C)
Upper Bakken	-0.259	0.403	-0.325
Lower Bakken	-0.303	0.612	-0.129

Table 3.7: Coefficients for the fitting of the Aki-Richards AVO approximation of the Zoeppritz equation for the Upper and Lower Bakken AVA curves.

3.3 Fluid substitution

Seismic velocity and impedance are affected by pore fluids, these fluids when substituted cause two main effects: a change in rock compressibility and a change in bulk density. In this study, to model the effect of fluid substitutions on the log data, and later use those logs to create and compare synthetic gathers on different fluid cases, it is necessary to define the properties of the constituents of the rock matrix in the Middle Bakken member using an effective porosity log, the averages ε, γ, δ, and the mineral Bulk modulus (Ko), shear modulus (Mu) and P-wave modulus (M) values from the averages Rho, Vp and Vs previous calculated for the Upper Bakken shale member of the Well V-1 (Table 3.8).

Mineral	Ko (GPa)	Mu (GPa)	Rho (g/cc)	M (GPa)	Vp (ft/s)	Vs (ft/s)
Quartz	36.6	45	2.65	96.6	19808.46	13,519.74
Shale	8.69	6.31	2.13	17.11	9,295.49	5,645.33
Calcite	76.80	32	2.71	119.47	21.783.31	11,273.93

Table 3.8: Mineral set for the fluid substitution in the middle Bakken Member. The elastic properties of the upper shale are used to define the properties of the constituents of the rock matrix in the Middle Bakken. The values for quartz and calcite, change very little with depth and are laboratory derived, so these are usually left at the default values.

Gassmann's fluid substitution has been an important tool in the interpretation of the seismic data on sedimentary materials for understanding of the relation between the elastic properties of a porous medium with fluid-filled and that same medium with empty pores. Gassmann (1975) considered a material in which all the pores that contribute the porosity are interconnected and have an irregular shape. This material is assumed to be homogeneous on a macroscopic scale with an isotropic background mineral, and the fracture systems contribute to negligible porosity to the rocks (Huang, 2016). Hence, for rocks with moderate or strong anisotropy, conventional Gassmann's equations might not be useful. Several theories have been developed for fluid-substitution in anisotropic media (Huang, 2016; Brown and Korringa, 1975) and should be used to evaluate the fluid substitution effects in log and seismic data in unconventional plays.

Figure 3.11 shows the resulting well logs after fluid substituting oil and gas into the Middle Bakken reservoir with an extension of the Gassmann Fluid Substitution for anisotropic VTI rocks using the Brown and Korringa (1975) algorithm that requires the Thomsen's parameters ε, γ, and δ to be specified as inputs. The calculation is performed in two steps: from the initial saturation to dry model and then from dry model to the final saturations of pure oil, pure gas, and pure brine.

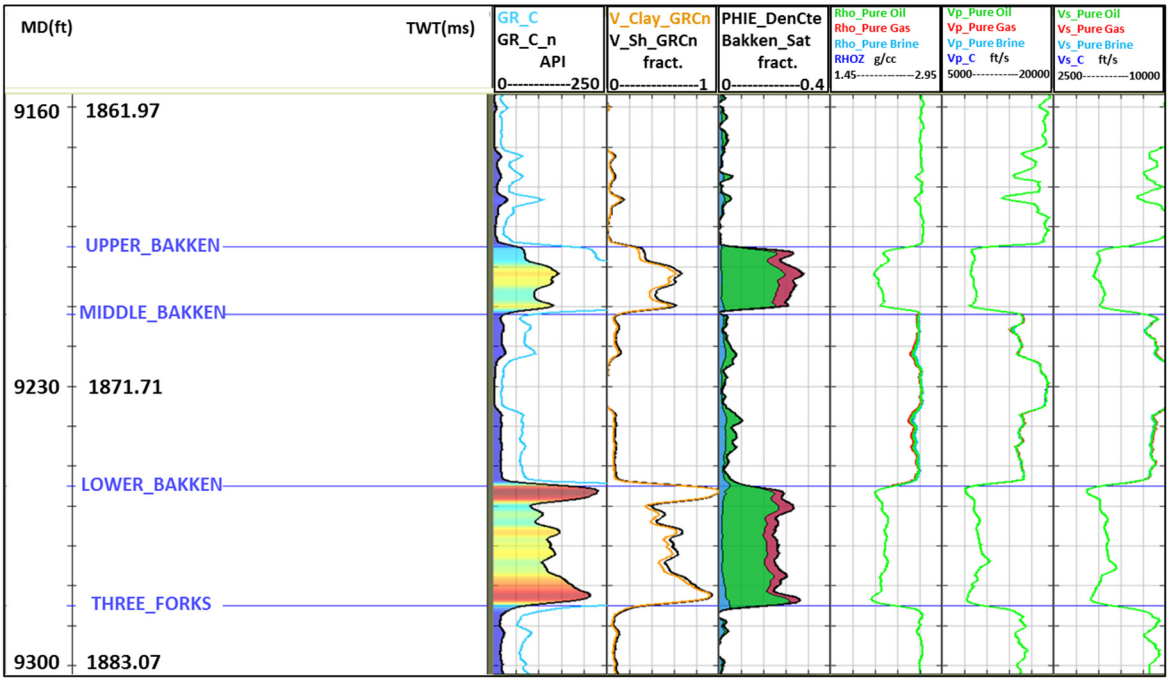

Figure 3.11: Effect of the Middle Bakken fluid substitution of Well V-1. From left to right, the comparison of the Rho, Vp, Vs resulting from the five fluid substitution cases: 100% Oil, 100% gas, 100% brine.

Minor changes in velocities Vp and Vs appear to define the fluid scenarios, however, when substituting for oil and/or gas, the expected decrease in density is noticeable. To have a better understanding of the potential effects of hydrocarbon on the elastic properties at the top reservoir interface between the Upper and Middle Bakken members, a blocky fluid substitution is performed. The QC plots are shown in Figure 3.12. Note in both the scenarios when the reservoir fluid is substituted by hydrocarbon, Vp, and density decreases. Vs appears to increase 1% as the direct result of density variation when gas is substituted and reaches a saturation of 70%.

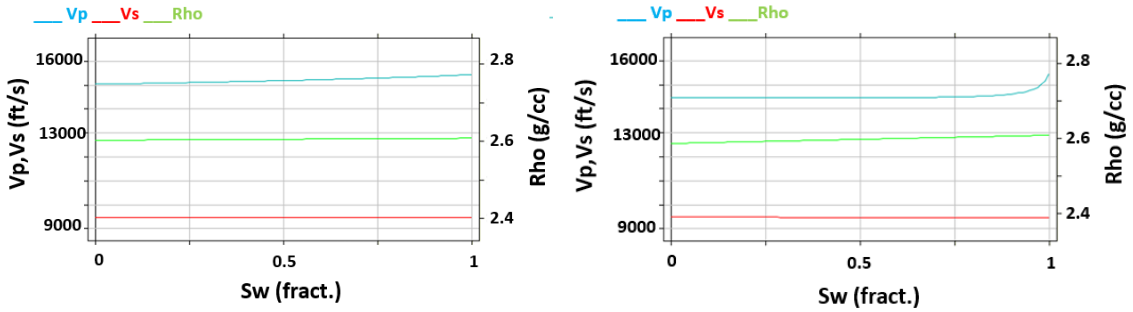

(a) Oil case (b) Gas case

Figure 3.12: Gassmann QC Sw vs. Vp, Vs plots for a) fluid substitution of oil, and b) fluid substitution of gas. Note how in both case scenarios, the higher the hydrocarbon saturation, the lower the Vp. Vs increases when substituting the reservoir with gas and remains constant in case of oil substitution. The density decreases proportionally to the hydrocarbon saturation.

To model the AVO effect of the fluid substitutions in seismic domain, the three calculated fluid scenarios are defined as different fluid combinations within the target

reservoir of the Middle Bakken. Figure 3.13 shows the comparison between the in situ and pure fluids PP pre-stack synthetic seismograms with a maximum angle of 45° in the vicinities of well V-1. The AVO effect is larger when the rock is saturated with gas and oil than with brine due to the difference in fluid densities that causes the P-wave velocity to decrease and so does the P-impedance of the rock.

Various macroscopic parameters of the system without the requirement of macroscopic homogeneity or isotropy have been defined in the Bakken shale using the anisotropic formulations for fluid substitution of Brown and Korringa (1975). The principal restrictions on the validity of their equations are that the pore system is assumed to be completely connected. Even though Middle Bakken sandstones vary in depositional facies and lithology, and locally exhibits good matrix porosity (as much as 14%) but with low permeability characteristics of tight reservoirs (Pollastro et al., 2011), a few isolated producing fields are characterized by extensive natural fractures and exceptional reservoir quality in the Middle Bakken member (Gerhard et al., 1982). Therefore, the minor fluid substitution effects observed on log and seismic data may be considered as a fair representation of the possible changes in density and velocities that can result after substituting brine for oil or gas in one of those isolated zones with considerably high porosity and permeability.

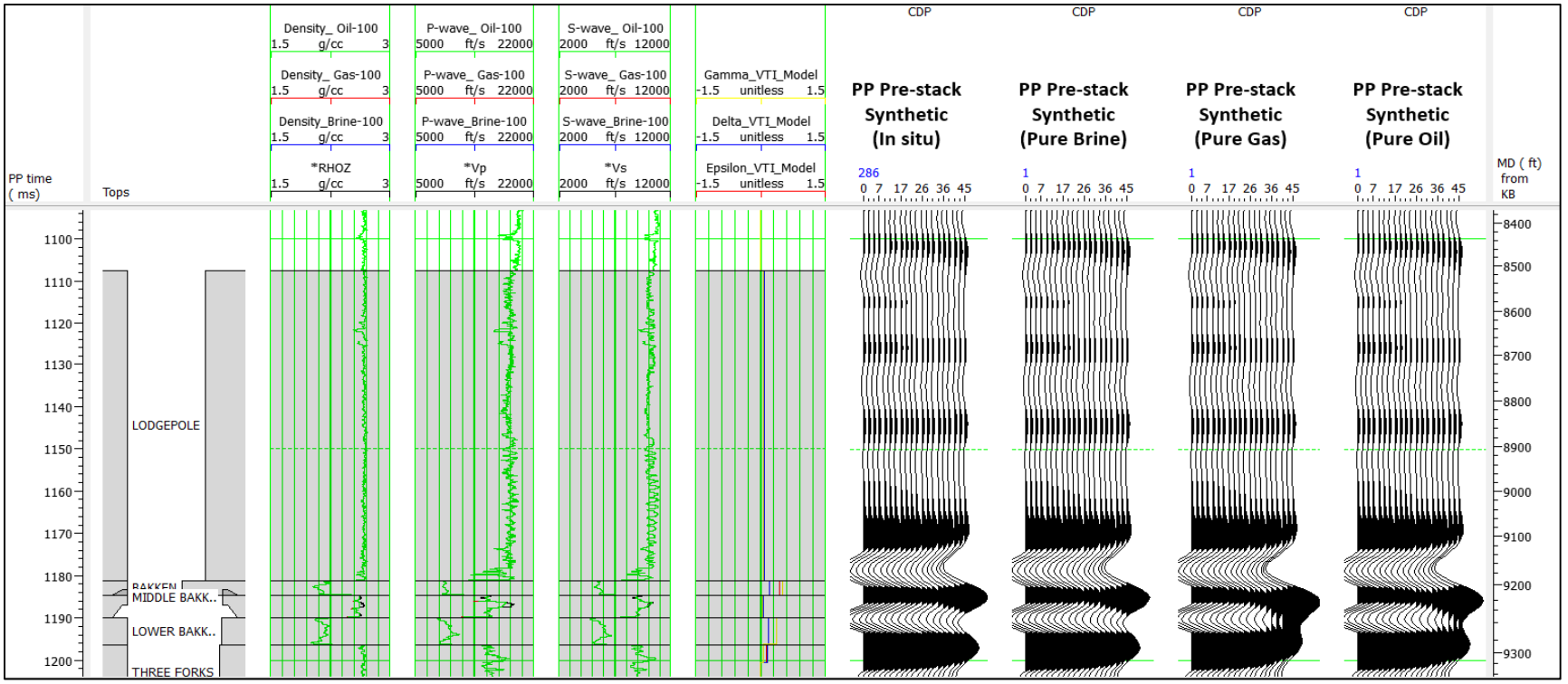

Figure 3.13: Comparison between the in situ PP synthetic of well V-1 and all the fluid substitution cases. From left to right: Density, Vp and Vs logs and their corresponding fluid-substituted values, Thomsen's parameters logs and synthetic seismograms for the in situ, 100% brine, 100% gas, and 100% oil cases.

Chapter 4

Seismic inversion

In general terms, using seismic data plus velocity and density information from well logs, and a velocity model of the earth's subsurface aims to determine a reliable model of the geology. Also understood as the reverse of synthetic seismogram modeling, seismic inversion is the process of calculating a subsurface impedance model consistent with the seismic data and other constraints. However, there are some issues related to this practice. Seismic data are frequency bandlimited and therefore is challenged in terms of providing fine resolutions as well as absolute background values, and inversion models are not unique solutions, as every set of data can be generated with a number of models and the determination of the best model requires geological information. Hence, in the process of seismic inversion, this additional information is usually entered by an initial guess low-frequency model and the given constraints on the deviation of the final from the initial model.

According to Savic et al., (2000) some advantages are related to the practice of model-based inversions such as: the resulting impedance section or volume has a broader bandwidth which maximizes the vertical resolution and minimizes tuning effects, since reflections are caused by impedance differences (and not velocity or wavelet differences), the impedance matches the reflectors better and measures the intervals, the recognition of subtle features is improved, and the calibrated impedance values can predict petrophysical properties through the seismic volume.

The inversion scheme to be used in this work is a model-based generalized linear inversion (GLI) algorithm that attempts to modify the model until the resulting derived synthetic matches the seismic trace within acceptable bounds. This method is based on the convolutional model and is an initial low-frequency P-impedance, S-impedance or density models, generated from well data and horizons. The approach is to minimize the following function:

$$J = weight_1 * (T - W * r) + weight_2 * (M - H * r) \quad (4.1)$$

Where, $T =$ the seismic trace, $W =$ wavelet, $r =$ final reflectivity, $M =$ initial guess model impedance, $H =$ the integration operator which convolves with the final reflectivity to produce the final impedance, $* =$ convolution operator.

The weight values determined how the inversion is balanced. A solution that models the seismic trace is forced by minimizing the first part $(T - W * r)$ of the equation

4.1, and a solution that models the initial guess impedance is forced by minimizing the second part ($M - H * r$). The seismic trace and the wavelet are known and the noise is random and uncorrelated with the signal. The method solves for the reflectivity iteratively, looking for differences between the real seismic trace and the synthetic generated from the model, and modifying the model to compensate (Hampson-Russell, 2014).

The stochastic model inversion approach merges the trace and initial guess model to provide the final inversion result. It considers that both the seismic trace and the initial guess impedance could be conflicting data and the model can deviate from the initial guess which is considered a soft constraint (Hampson-Russell, 2014). On the other hand, in constraint model inversion, boundaries for how far parameters can deviate from the initial guess are set, the maximum impedance change is a percentage of the average impedance of the log and the model cannot go beyond these values.

This chapter presents further analysis of the 2D-3C seismic interpretation project undertaken in the Bakken shale dataset. From Well V-1, a model-based joint PP-PS inversion of a 2D seismic line is conducted to estimate P-impedance, S-impedance, density, and Vp/Vs. As a first approach, a post-stack inversion of the PP data is performed to establish some constraints for the inversion parameters and its results, are qualitative and quantitatively compared to the joint inversion outputs.

The main purpose of the PP-PS inversion is to characterize each member of the Bakken Formation in terms of the extrapolation of rock properties in the seismic extent by improving vertical resolution and to relate the elastic properties to locate zones with TOC content according to the study of Chapter 2. The inversion analysis is performed

4.1 PP seismic interpretation

4.1.1. Well-to-seismic tie and seismic resolution

A 2D seismic PP section and two log curves available in the well: P-wave velocity and density are used to extract a wavelet, to optimize the depth-time relationship between the well and seismic, and to compare with the resulting synthetic. In the study area, only the Well V-1 crosses the 2D seismic line available and their tie is fundamental to achieve reliable inversion results. The log correlation process begins with the estimation of the amplitude spectrum from the seismic data by means of a statistical wavelet extraction in an interval that includes the reservoir (1500 – 2000 ms). In this first step, an assumption of constant zero-phase is made and the tie is performed to achieve a high correlation between the synthetic and the real seismic. Secondly, a full wavelet is then extracted in the same window that includes the reservoir using the sonic and density logs from the well to calculate the frequency, phase spectra, and resolution limit of the seismic. Table 4.1 shows the extraction parameters for the statistical wavelet. The preliminary PP statistical wavelet and its corresponding frequency spectrum are seen in Figure 4.1.

Extraction parameters	PP wavelets
Window length	500 ms
Wavelet length	200 ms
Taper length	25 ms
Sample rate	2 ms

Table 4.1: Parameters for the PP statistical and full wavelet extraction at the Well V-1.

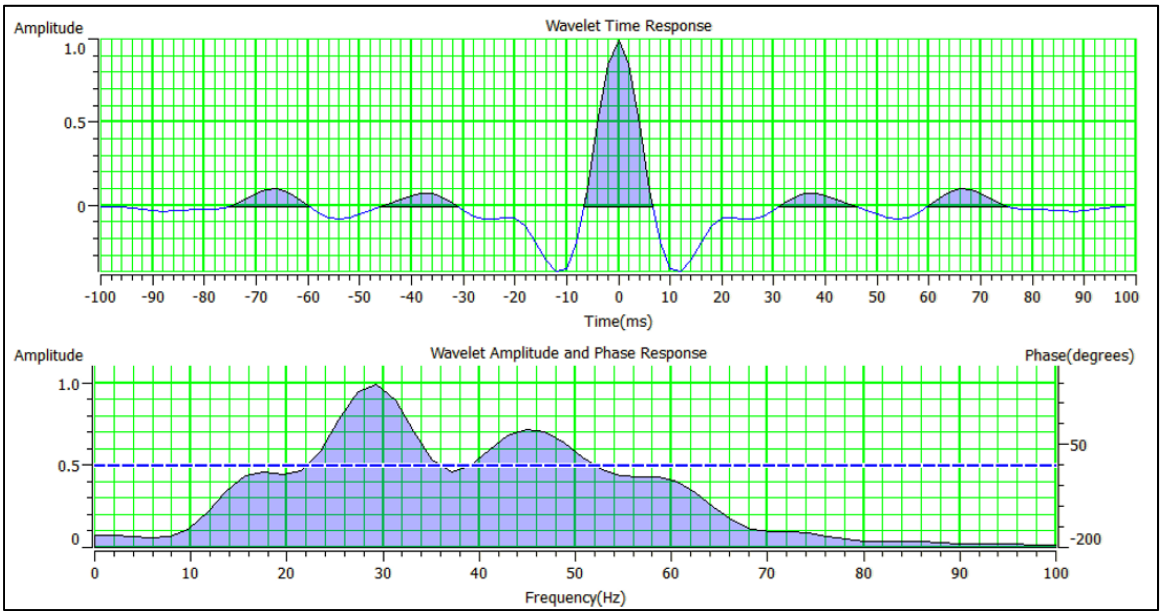

Figure 4.1: PP statistical wavelet extracted from the seismic and its corresponding frequency spectrum. The wavelet extraction is performed in a window from 1500 to 2000 ms (a 500 ms window length). The dotted shows a zero-phase angle.

The Bakken Formation is generally very thin compared to other shale plays in the U.S. and its closely spaced interfaces could be characterized by constructive or destructive interference caused by tuning effects. At the well location, the Lodgepole limestone is 683 ft and overlies the Bakken Formation and its upper, middle, and lower intervals of only

17 ft, 43 ft, 30 ft thick, respectively. The reciprocal of the dominant period of the extracted PP statistical wavelet (34 ms) corresponds to a dominant frequency of 29 Hz for the vertical resolution estimation of the PP data. Thus, the resolution limit of about one-quarter of the wavelength (Widess, 1973) is calculated to be around 91 ft for the PP seismic using the P-wave average RMS velocity for the Bakken Formation of 10,600 ft/s calculated from the dipole sonic interval velocities at the reservoir level.

According to this calculation, only Lodgepole and Three Forks Formations should be possible to be resolved in the seismic data. The 90 ft-thick Bakken Formation, on the other hand, might not be completely resolved in the vicinities of the well. A full wavelet extraction (Figure 4.2) in the window that includes the reservoir is then carried out using not only the seismic but the sonic and density logs from the well to calculate both, the frequency and phase spectra and to give an idea about the highest seismic vertical resolution limit. In this case, the dominant frequency calculated from the dominant period of the extracted PP full wavelet corresponds to 50 Hz and the resolution limit results around 82 ft indicating that Bakken Formation could be resolved in the seismic data. This observation agrees with the horizon interpretation and the results of the synthetic seismic modeling discussed in Chapter 3 where the tops of the Bakken and Three Forks Formations were resolved with a lower frequency Ricker wavelet of 45 Hz convolved with the respective reflectivity series of the vertical well.

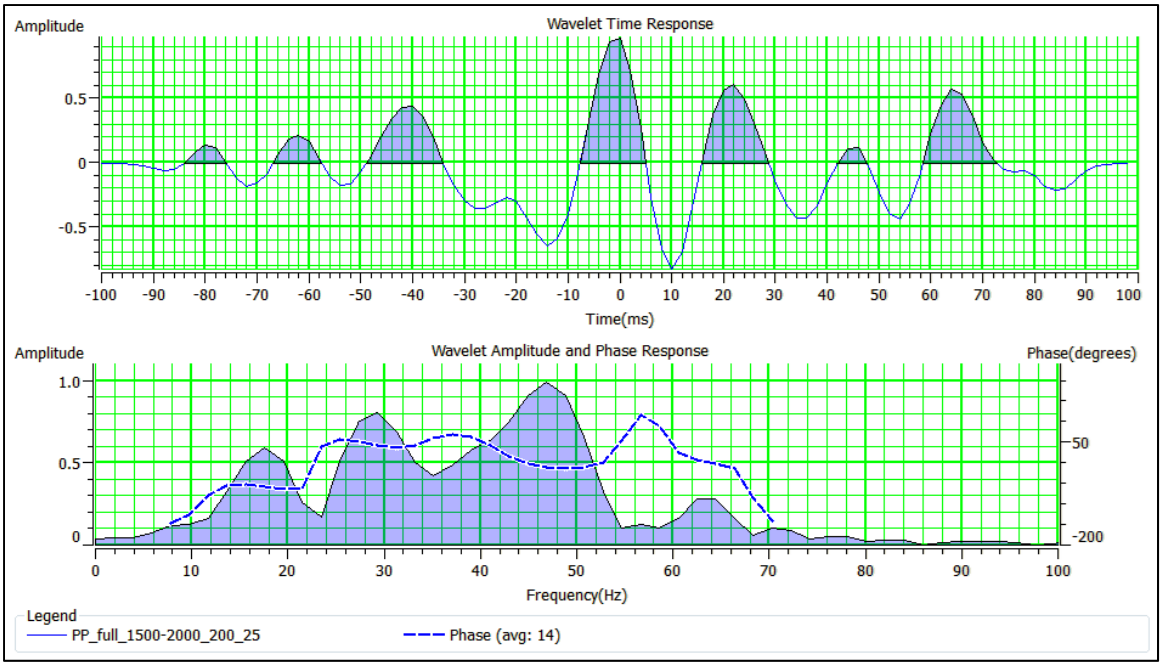

Figure 4.2: PP full wavelet extracted from the seismic and its corresponding frequency spectrum. The wavelet extraction is performed in a window from 1500 to 2000 ms (a 500 ms window length). The dotted shows an average phase angle of 14 degrees.

The process of log correlation examines the current depth-time conversion and optimizes it so that the derived synthetic matches the seismic data optimally. The composite trace is created by averaging the traces around the borehole location we are using for the seismic correlation. For a vertical well, such as V-1, that means averaging a selected set of neighboring traces around the borehole.

Although the full wavelet gives a better resolution limit, the statistical wavelet is used for well-to-seismic ties purposes, it gives a better correlation since it does not take into account the effect of the several side lobes enough to allow matching of surface

multiples as well as primary signal. Figures 4.3 shows the log correlation results for the well-to-seismic tie with the statistical wavelet. The blue traces are copies of the synthetic trace. This trace was calculated from the sonic and density logs in this well, the depth-time curve currently stored in the database, and the respective wavelet we have previously extracted. The red traces are repeated copies of the average (or composite) trace extracted from the seismic data. The cross correlation between the synthetic trace and the composite trace shows, in both well-to-seismic ties a roughly symmetrical peak at zero lag time, with a maximum correlation of 75%.

Two provided horizons of the tops of the Bakken and Three Forks Formations that correspond to a published interpretation of a 3D seismic survey in the area of study are taken only as a reference of the approximate PP time of these two formations of interest for horizon picking and log correlation purposes. New horizons are then interpreted for the top of Lodgepole, Bakken and Three Forks Formations specifically at the zero-crossing (1790 ms), trough (1860 ms) and peak amplitude (1880 ms), respectively in the vicinities of the well.

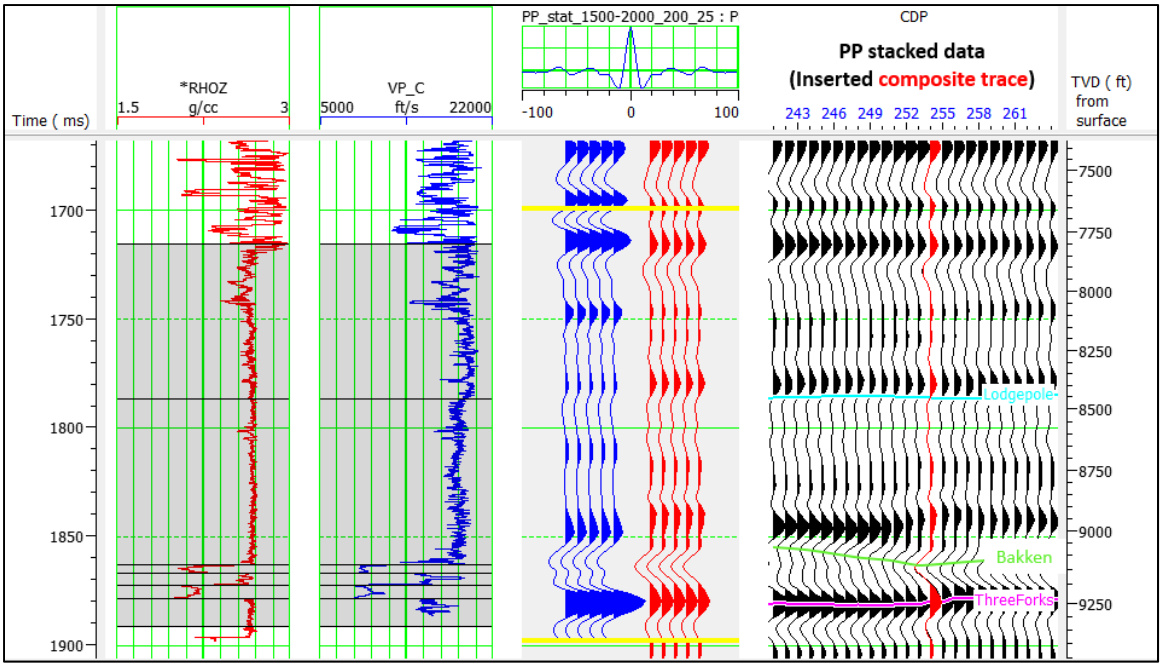

Figure 4.3: Well-to-seismic tie of the well V-1. From left to right, tracks show density and P-wave velocity logs, zero-offset synthetic computed with statistical wavelet extracted from the seismic (blue traces), trace extracted from real seismic at the well location (red) and real PP seismic going through the well location with the interpreted horizons for the top of the Lodgepole, Bakken and Three Forks Formations. The correlation coefficient between the synthetic computed with the statistical wavelet and the seismic is 0.756 under the correlation window (yellow lines).

4.2 Post-stack inversion

The post-stack inversion technique is carried out to determine the seismic P-impedance by scaling the wavelet that comes from acquisition and processing steps and

restore its low-frequency component through well control. An initial guess at the velocity structure is represented by the model. The final result is a velocity profile that deviated as little as possible from the initial guess while modeling the real data as closely as possible. The interpretative process is summarized in three main steps: 1) determine a layer model of reflection coefficients with a source wavelet and seismic data assuming a set of homogeneous plane layers, 2) calculate the resulting impedances, and 3) ensure that the model meets the constraints. (Hampson-Russell software manual). Figure 4.4 shows the model-based post-stack inversion workflow.

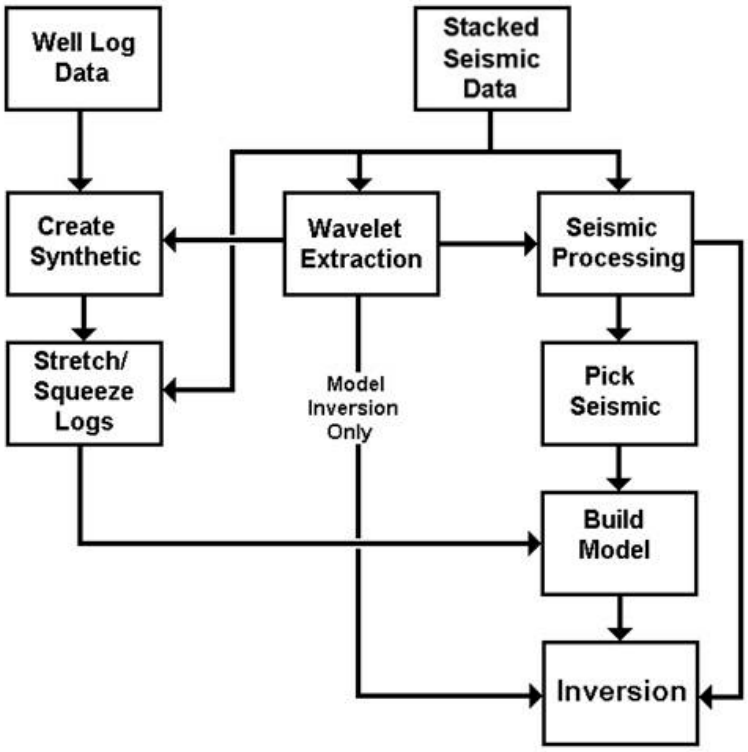

Figure 4.4: Model-based post-stack inversion workflow. Modified from the Hampson-Russell manual.

Once the general processes of statistical wavelet extraction, composite synthetic traces generation, well correlation and P-wave velocity log correction are achieved, it is time to build the initial stratigraphic model, test the inversion parameters and invert the post-stack data.

4.2.1 Initial models

With the objective of overcoming instability issues and constraining the inversion process, seismic models are obtained by extrapolating the well logs using the Lodgepole and Three Forks horizons as a guide. After interpolating the well log curves, the interpolated models are generated in two ways. On one hand, the models are not modified any further than the interpolation from the control points. On the other hand, a low –pass frequency filter is applied passing all frequencies up to 15 Hz, filtering all frequencies above 20 Hz and interpolating the filter between those limits.

Figures 4.5 to 4.8 show the P-impedance, S-impedance, density, and Vp/Vs models generated in both ways for them to be used as input in the inversion. The inserted logs at each profile correspond to their respective calculated impedances, density, and Vp/Vs properties and the matching well-log filtered to the frequency of the model.

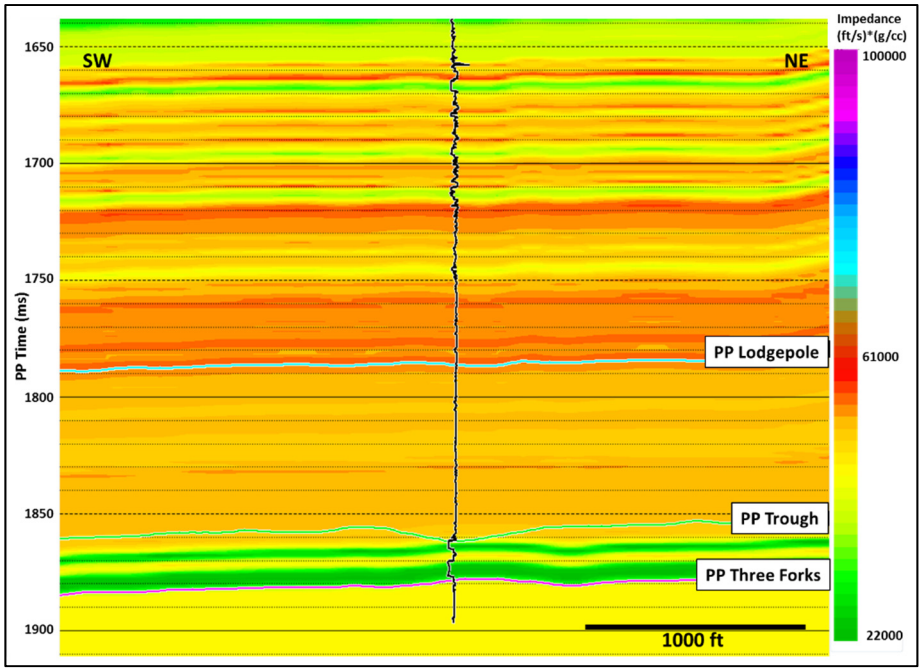

(a)

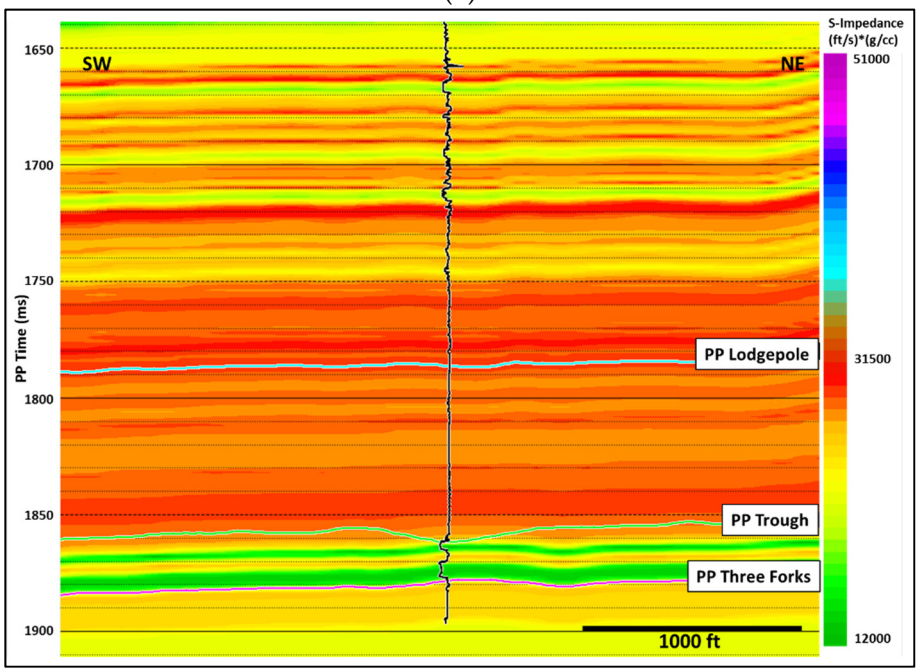

(b)

Figure 4.5: SW-NE sections of (a) P-impedance (Zp) and (b) S-impedance (Zs) models going through the Well V-1 location. The displayed curves are (a) P-wave velocity (b) S-impedance.

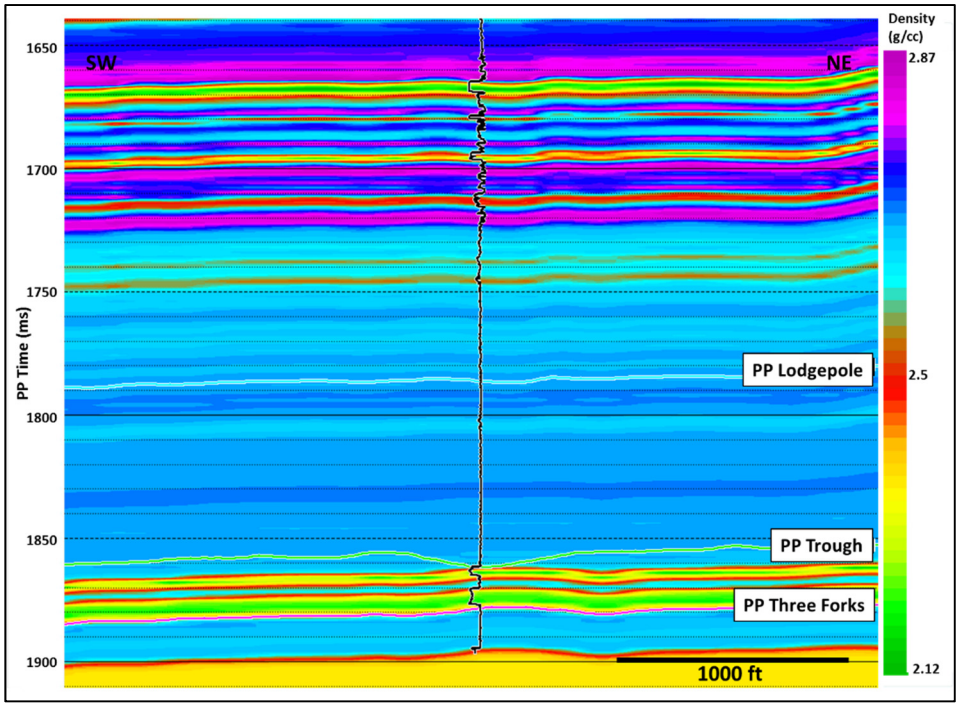

(a)

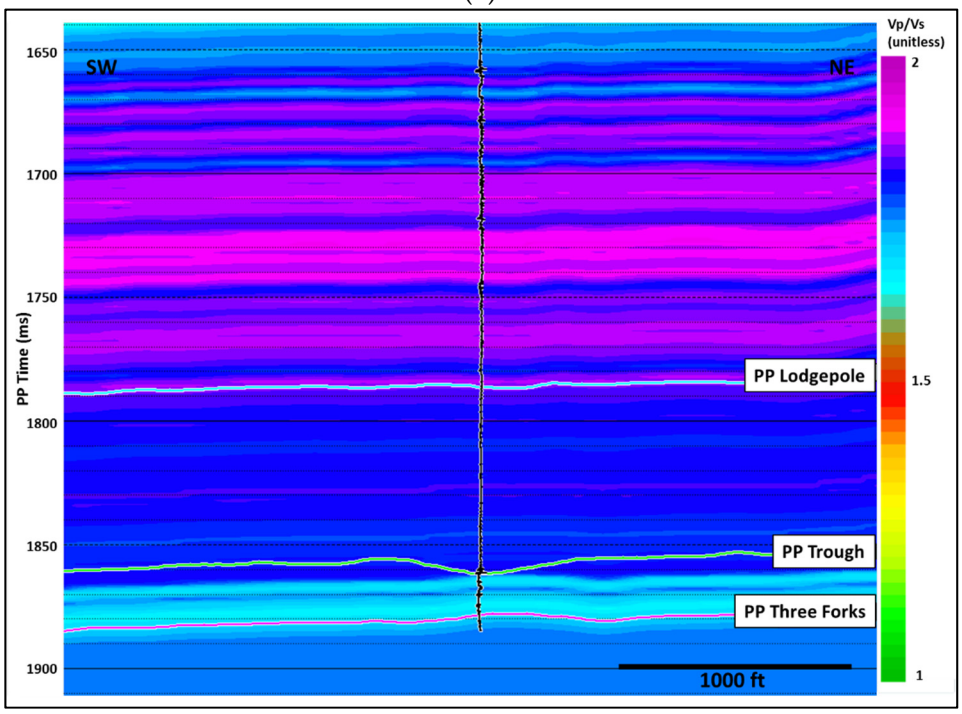

(b)

Figure 4.6: SW-NE sections of (a) density and (b) Vp/Vs models going through the Well V-1 location. The displayed curves are (a) density (b) Vp/Vs.

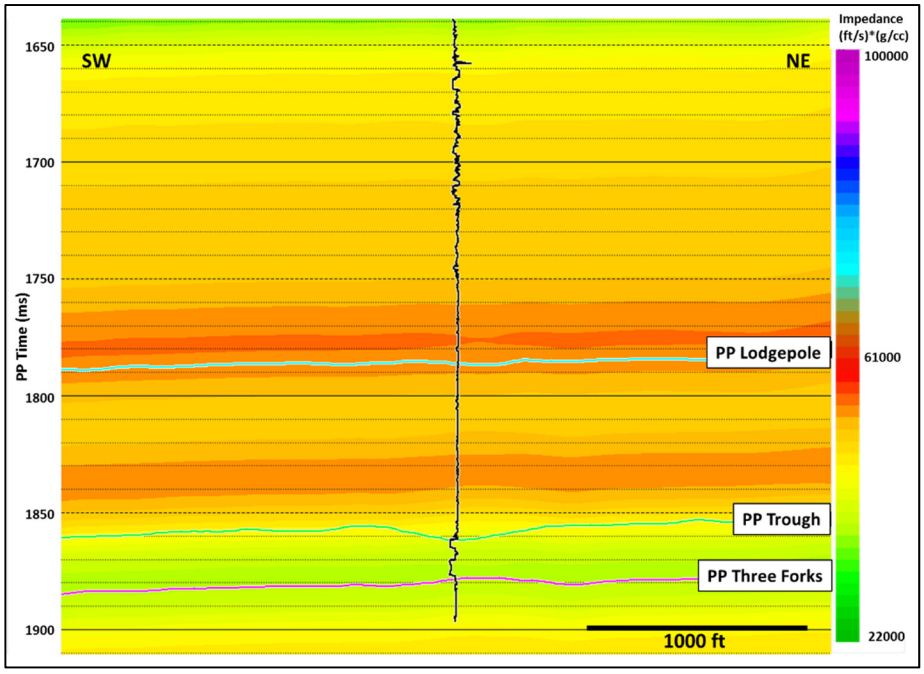

(a)

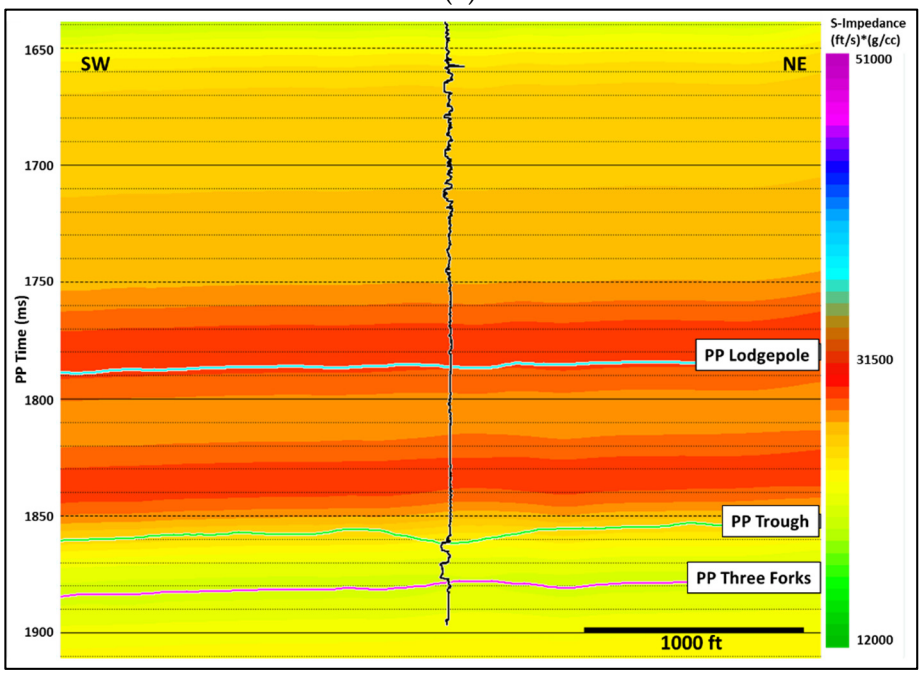

(b)

Figure 4.7: SW-NE sections of (a) P-impedance (Zp) and (b) S-impedance (Zs) low-frequency models going through the Well V-1 location. The displayed curves are (a) P-wave velocity (b) S-impedance.

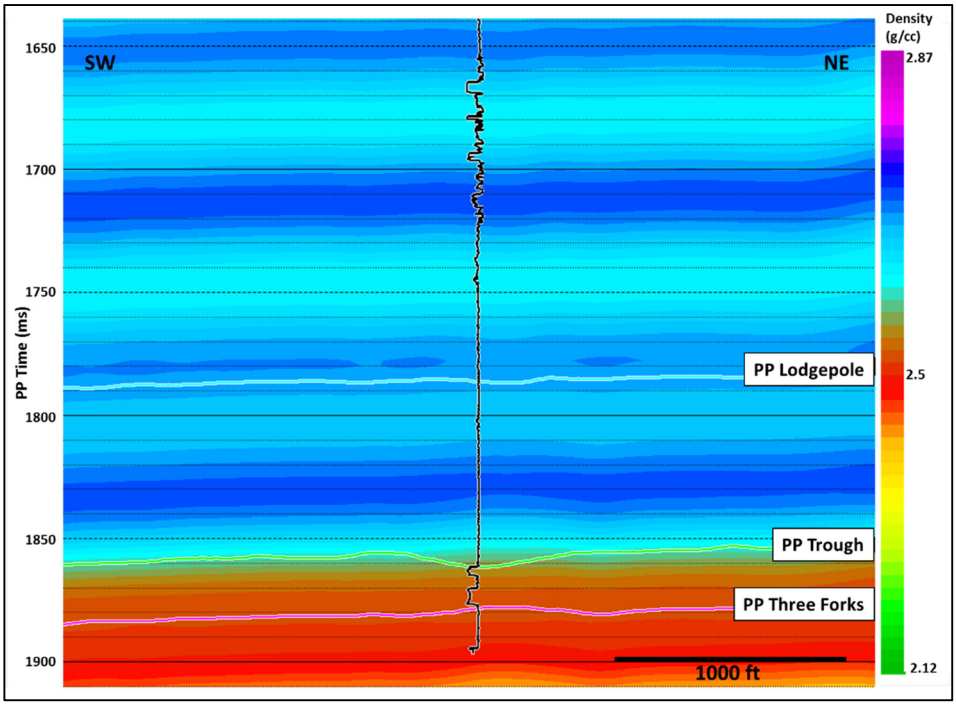

(a)

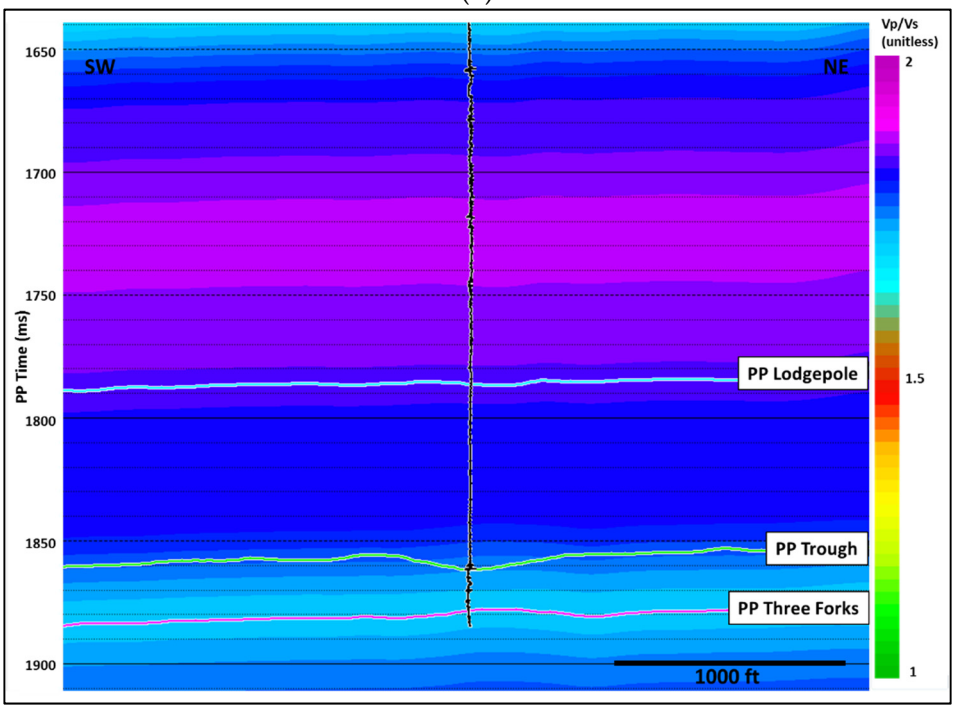

(b)

Figure 4.8: SW-NE sections of (a) density and (b) Vp/Vs low- frequency models going through the Well V-1 location. The displayed curves are (a) density (b) Vp/Vs.

The initial models show a fair extrapolation of the well information, including its high-frequency content. P and S impedances, density and Vp/Vs resulting properties of the Lodgepole, Three Forks and Bakken thin members agree with the log values and can be visualized and interpreted in the seismic domain. However, since seismic data are limited to a specific band of frequencies and log data include frequencies that are higher and lower than that of seismic data, the filtered models are preferably used for the post-stack inversion process. These models honor the well log data for the low-frequency band which avoids using frequencies higher than the seismic and hence, does not allow to introduce too much model influence into the inversion that cannot be confirmed by the post-stack section.

4.2.2 Inversion analysis

The inversion is performed on selected traces from the post-stack seismic data to quickly test a range of inversion parameters that will constraint later the PP-PS joint inversion. The process creates inverted synthetics for the well location to compare to the actual velocity and density well curves.

The geological model is perturbed until the error between the synthetic and the original seismic data is minimized. The wavelet in the seismic data is known and, in fact, is the statistical wavelet extracted for the well-to-seismic tie. A synthetic seismogram is calculated for each trace using this wavelet and the initial guess impedance. The

impedance is then modified gradually until the synthetic trace matches the real trace within some tolerance level. The model inversion algorithm produces a pseudo-P-wave-velocity log by dividing the zone into layers or blocks. The average size of block is set to 2 ms and as a result, this log has a coarser resolution than the sonic log from the well information. Constrained model inversion is undertaken to prevent small amounts of noise in the data, or modeling errors (Hampson-Russell manual).

The inversion results at the Well V-1 is seen in Figure 4.9. The inversion window corresponds to 500 ms (from 1500 to 2000 ms in time) and its resulting log (in red) is overlying the impedance log-filtered to the approximate seismic frequency plus the model frequency band (0-0-50-60). The RMS error of 7,586.21 ft/s*g/cc is calculated in the entire window for the inverted P-impedance, however, with a practically zero error of 0.104, the error trace, which is the difference between the synthetic traces generated and the original composite trace at the well location indicates that the inversion is mathematically correct and can be applied to the entire line. Note how the inverted log has the same trend of the impedance log at depths of the Bakken Formation. However, it finds difficult to model the three Bakken members that are below seismic resolution.

Another inversion analysis is done using the unfiltered models with the objective to compare the results in high and low-frequency domains (Figure 4.10). In this case, the error trace increases in 16% but the inverted impedance log is picking up the Upper, Middle and Lower Bakken allowing us to use the inverted line to map their P-impedances

that later is are going to be useful for validating the PP-PS joint inversion results. Figure 4.11 shows the difference between the seismic and the synthetic at the 2D line going through the well location for the case of higher frequency. Note that the amplitude of the traces is almost zero which indicates that the synthetic seismogram and the real seismic are almost identical (error trace equal to 0.208).

The line going through the Well V-1 location in Figures 4.12a and 4.12b shows the inverted P-impedance sections of low and high frequency resulting from this preliminary post-stack inversion. Cold colors represent high property values and warm colors represent low-density values. In both cases, the resolution is improved compared to their respective model and the values of P-impedance are accurately represented in the inversion for the Lower Bakken member at the vicinity of the vertical well with around 25,000 ft/s*g/cc. The high-frequency inversion additionally shows values around 25,000 and 40,000 ft/s*g/cc for the Upper and Middle Bakken, respectively.

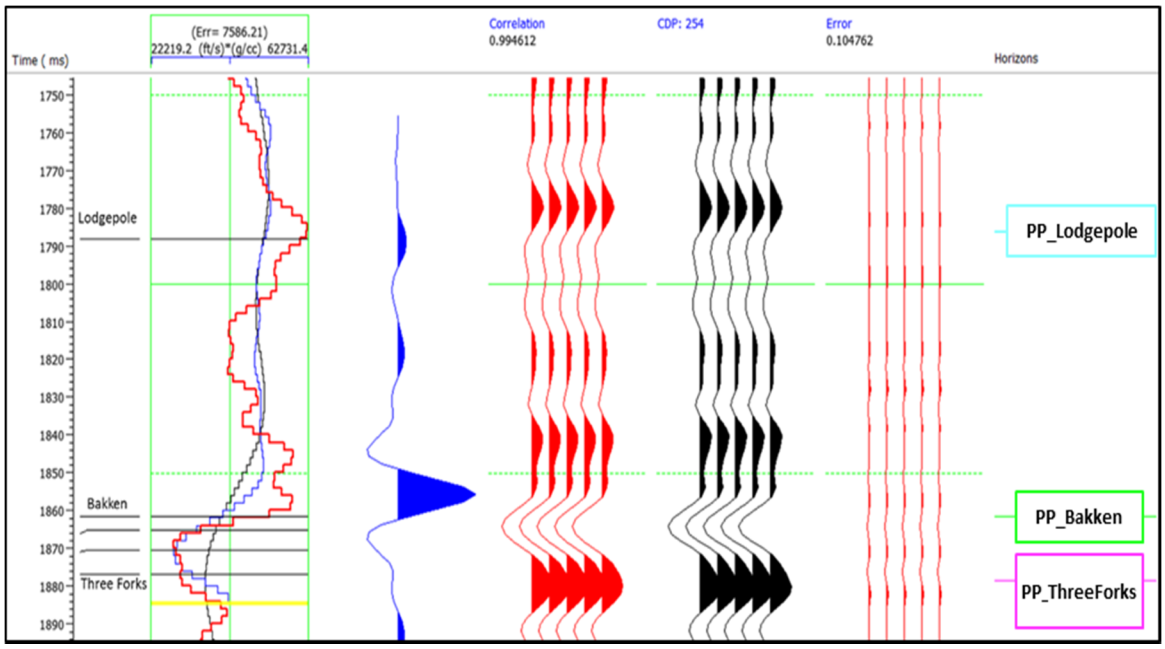

Figure 4.9: PP post-stack inversion results for the interest intervals at the Well V-1 location using the low-frequency model. From left to right, tops from logs, inversion result (in red), filtered impedance log from the well (in blue), selected wavelet, synthetic traces calculated from the inversion result (red), original composite traces (black), repeated error trace (red) and picked horizons. There is a very good correlation between the inversion results and the trend of the original logs in the Bakken Formation.

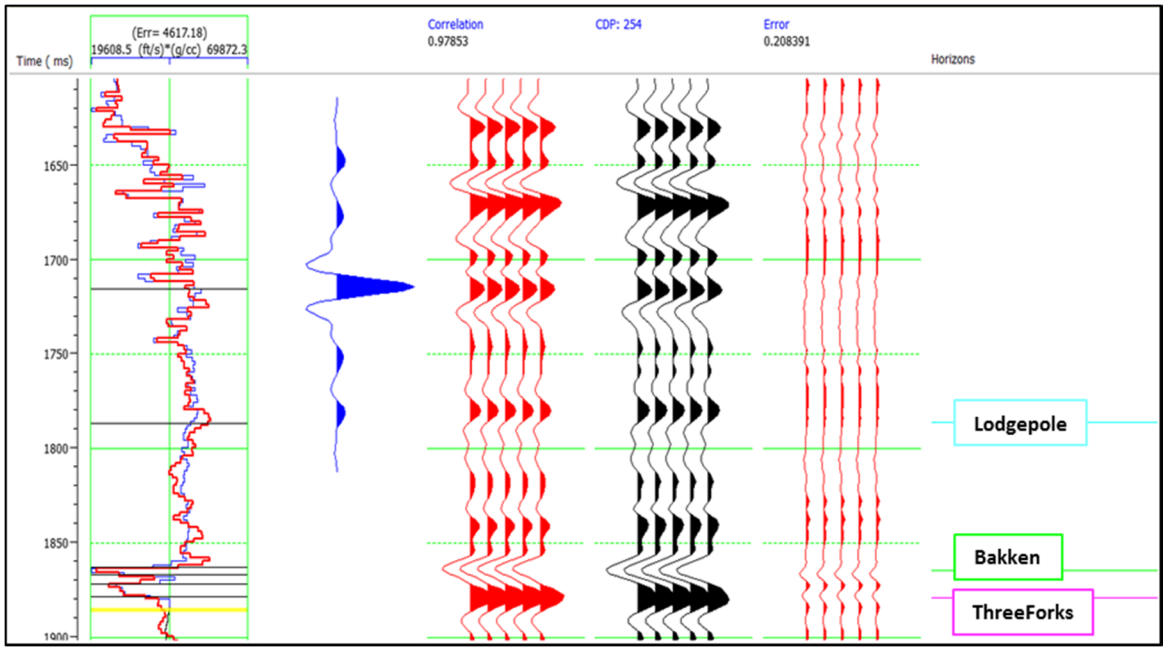

Figure 4.10: PP post-stack inversion results at the Well V-1 location. From left to right, inversion result (in red), filtered impedance log from the well (in blue), selected wavelet, synthetic traces calculated from the inversion result (red), original composite traces (black), repeated error trace (red) and picked horizons. There is a very good correlation between the inversion results and the original logs. The Bakken members are resolved.

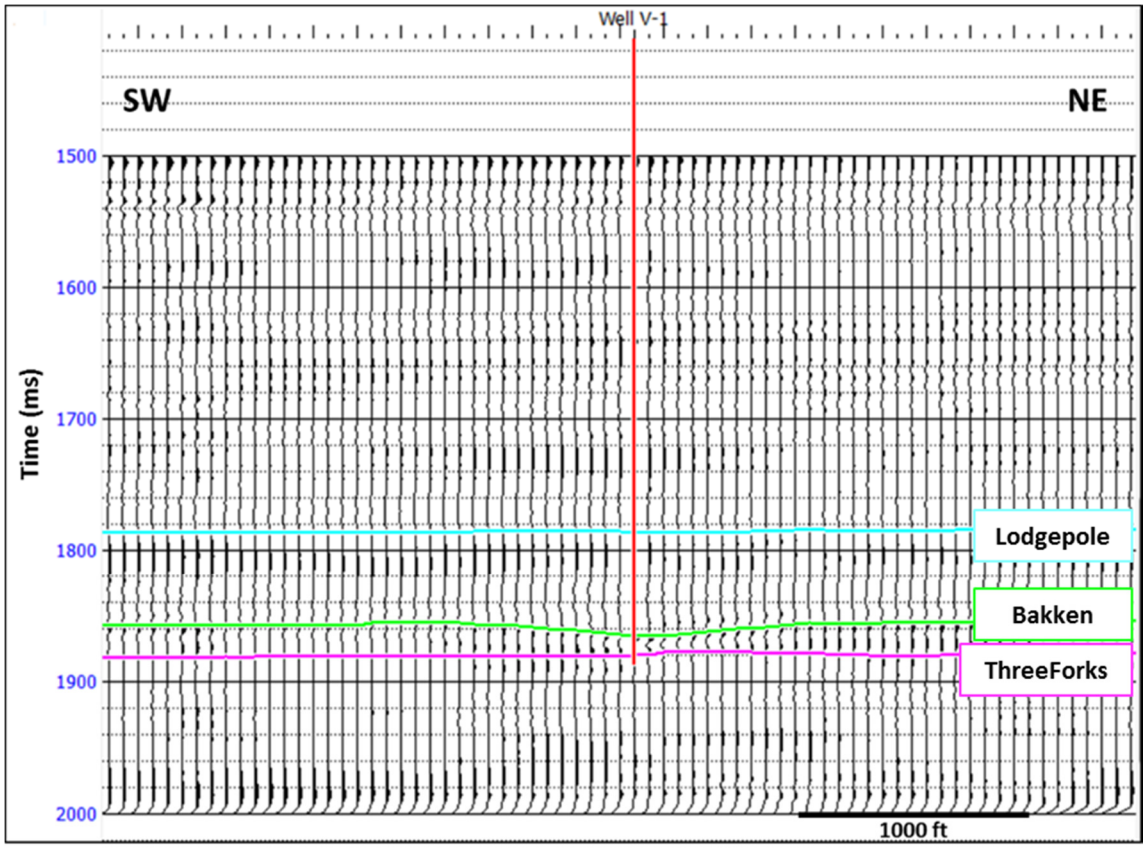

Figure 4.11: Difference between the PP seismic and the PP synthetic at the line going through the well location. Note that the amplitudes of the traces are almost zero which indicates that the synthetic seismogram and the real seismic are almost identical (error trace equal to 0.208).

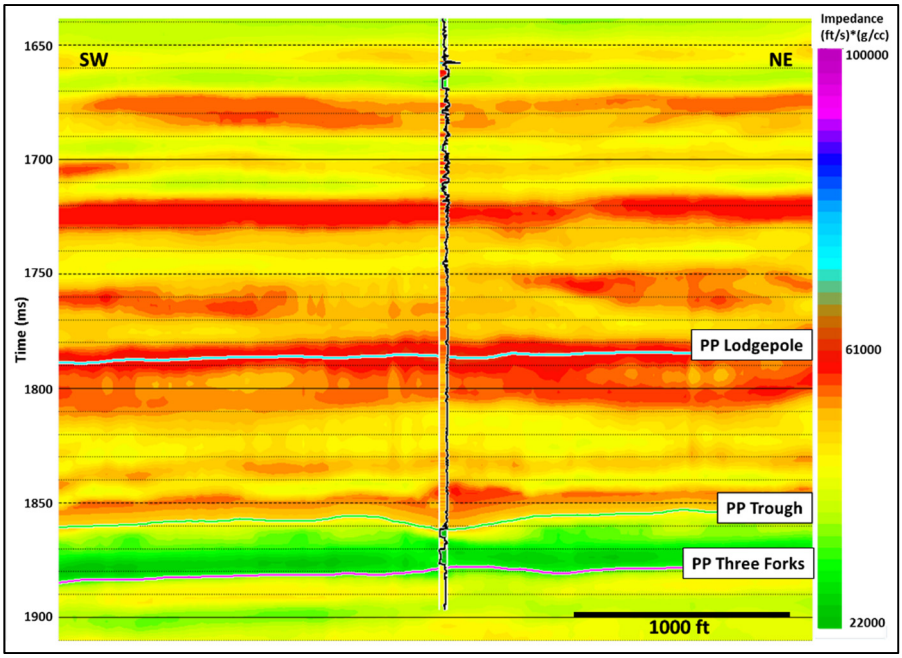

(a)

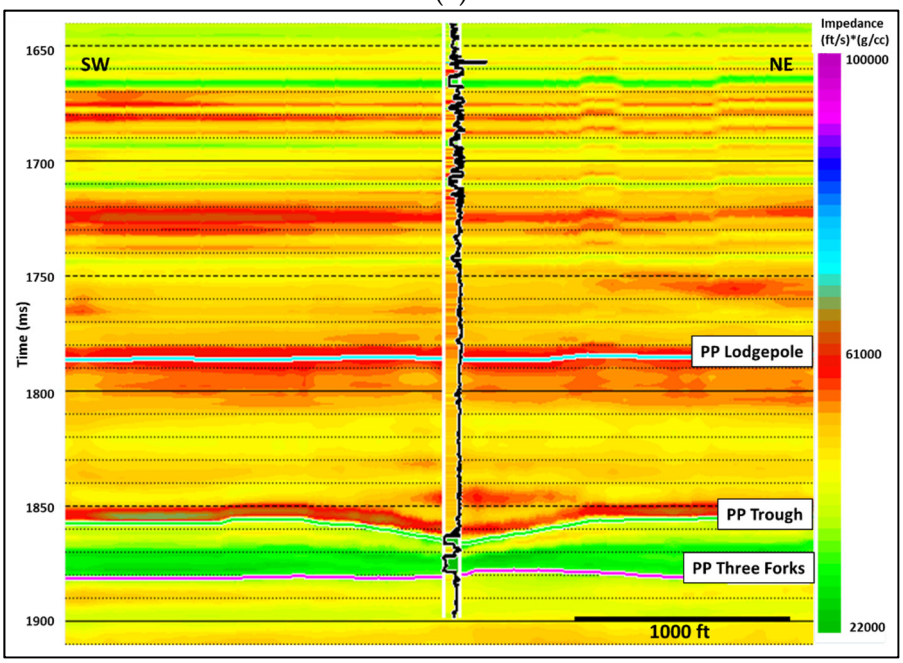

(b)

Figure 4.12: SW-NE inverted sections of (a) filtered P-impedance and (b) high-frequency P-impedance going through the Well V-1 location. The displayed log corresponds to the computed P-impedance log.

4.3 PP-PS post-stack joint inversion

PP-PS Joint Inversion is one of the most common inversion approaches when multicomponent seismic data are available and it allows to transform seismic reflection data into quantitative properties that can describe the subsurface such as the acoustic impedance (P-impedance) and the shear-wave impedance (Hampson-Russell, 2014). Given a long-offset seismic data, it is possible to potentially estimate a density volume if an unconventional reservoir characterization is a goal.

A model based linearized inversion is implemented for the joint inversion of the available Bakken Shale dataset. Russell (2014) states three main assumptions of the analysis:

1. The linearized approximation of reflectivity holds.
2. PP and PS reflectivity as a function of angle can be given by the Aki-Richards linearized equations.
3. The background trend can be described by a linear relationship between the logarithm of P-impedance and both S-impedance and density. The algorithm tries to solve for deviations away from a linear fit in logarithm space (Hampson and Russell, 2013).

A linearized inversion of the modified Aki-Richards linear approximations for the angle dependent PP and PS reflection coefficients $R_{pp(\vartheta)}$ and $R_{ps(\vartheta)}$ allows the estimation of P, S and density reflectivities (R_p , R_s and R_D) (Russell et al., 2005; Russell, 2014).

$$R_{pp(\theta)} = c_1 R_p + c_2 R_s + c_3 R_D \tag{4.1}$$

$$R_{ps(\theta,\Phi)} = c_4 R_s + c_5 R_D \tag{4.2}$$

$$R_p = \frac{1}{2}\left[\frac{\Delta V_P}{V_P} + \frac{\Delta \rho}{\rho}\right] \tag{4.3}$$

$$R_S = \frac{1}{2}\left[\frac{\Delta V_S}{V_S} + \frac{\Delta \rho}{\rho}\right] \tag{4.4}$$

$$R_D = \frac{\Delta \rho}{\rho} \tag{4.5}$$

Coefficients c_1 to c_5 are functions of the angle of incidence, angle of reflection and the Vp/Vs ratio (Russell et al, 2005).

The inputs for the inversion are the PP seismic data, PS seismic data registered to PP time, the interpreted seismic horizons, the two wavelets extracted from both seismic volumes and the low-frequency initial models of P-impedance, S-impedance, and density are generated using the available well. The models will then be perturbed in each iteration until the error between the observed and modeled data is minimized and the joint inversion outputs will correspond to P-impedance, S-impedance, and density lines. The multicomponent joint inversion workflow is seen schematically in Figure 4.13.

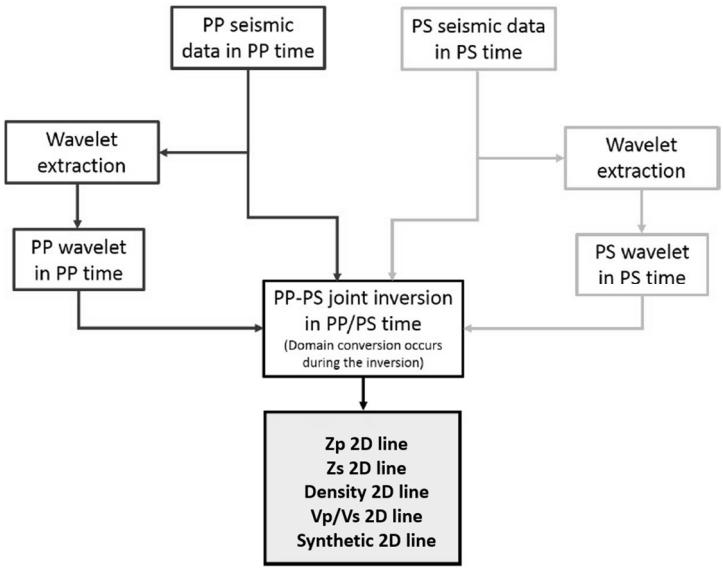

Figure 4.13: PP-PS joint inversion workflow. (Modified from Ruiz, 2016).

4.3.1 PP and PS joint interpretation

The PP seismic interpretation defines a similar process for the PS effort. A wavelet was statistically extracted from the PS seismic in a 1500 ms window that includes the reservoir and a constant zero-phase was assigned. The wavelet-extraction parameters are seen in Table 4.2. Figure 4.14 shows the comparison between the final PP and PS wavelets and their corresponding frequency spectra, with dominant frequencies around 29 Hz and 14 Hz, respectively.

Extraction parameters	**PS wavelet**
Window length	1500 ms
Wavelet length	200 ms
Taper length	25 ms
Sample rate	2 ms

Table 4.2: Parameters for the PS statistical wavelet extraction at the Well V-1

The PS seismic vertical resolution is estimated in the same way as the PP data. Using the dominant frequency of 14 Hz and the S-wave average RMS velocity calculated at the reservoir level (6,200 ft/s), the vertical resolution for the PS data corresponds to approximately 110 ft, that is 20 ft lower than the PP seismic resolution.

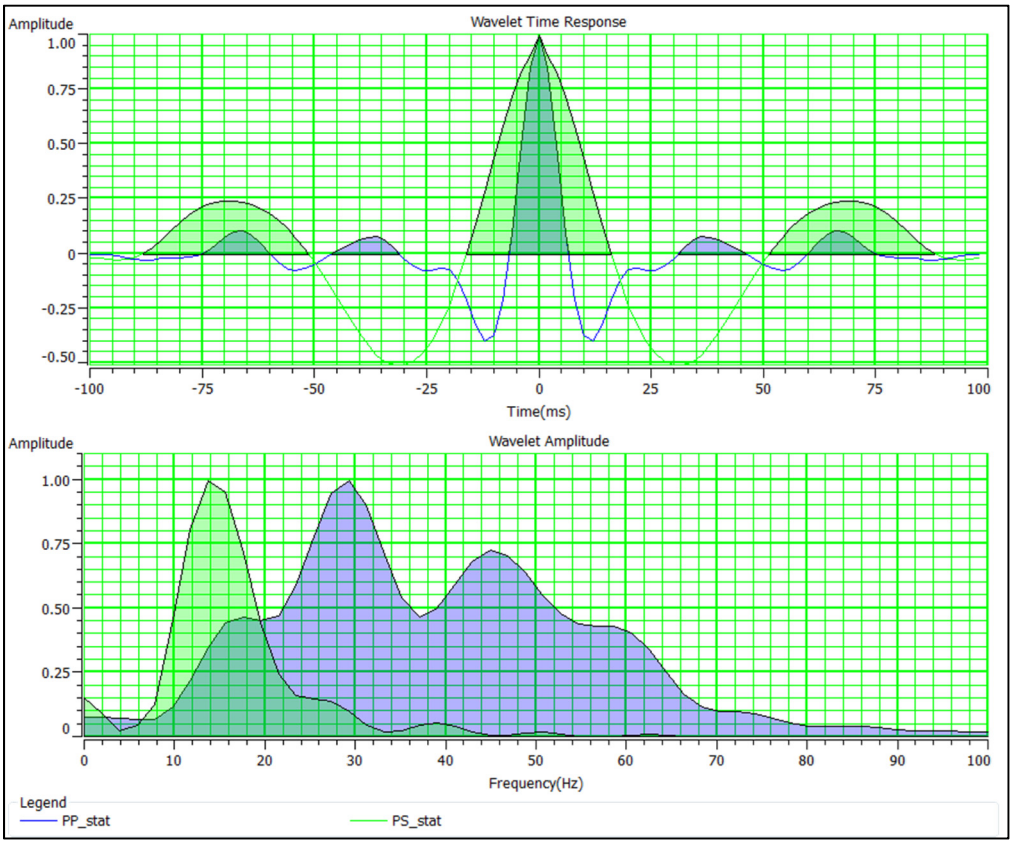

Figure 4.14: PP (green) and PS (blue) full wavelets and their corresponding frequency spectra. The PS frequency spectrum shows a higher peak frequency than the PP spectrum but the PP data show bigger bandwidth which translates into better seismic resolution.

Figure 4.15 shows the PS well-to-seismic tie for the vertical well. From left to right, well tops, density, P-wave velocity and S-wave velocity logs are shown. PS and PP stacked

data are also shown in PS time. Since there is no mode-conversion at zero-offset, the PS synthetic traces in blue are generated at an incidence-angle of 20° to approximate zero-offset. There is a fair correlation between the converted-wave data and the synthetic seismogram with a coefficient of 0.727.

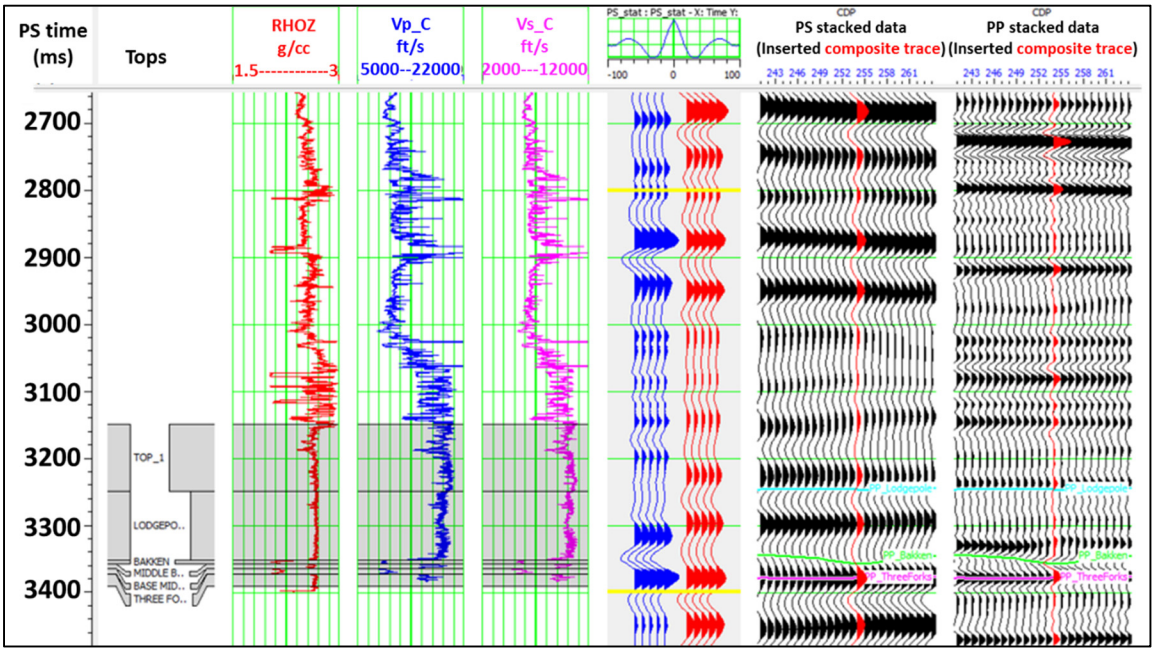

Figure 4.15: PS data well-to-seismic tie for the well V-1. From left to right, tracks show tops from logs, density, P-wave and S-wave velocity logs, 20° incidence-angle synthetic seismogram computed with statistical wavelet extracted from the seismic (blue traces), trace extracted from real PS seismic at the well location (red) and real PS seismic going through the well location with the interpreted horizons for the top of the Lodgepole, Bakken and Three Forks Formations. The correlation coefficient between the synthetic and the seismic is 0.727 under the correlation window (yellow lines).

4.3.2 PP-PS registration

The joint inversion process requires the alignment of the geological events in both PP and PS lines. In order to do that, a domain conversion is achieved at the well location through depth-time curves generated from the corrected P-wave and S-wave velocity logs resulting from their corresponding correlation process with the PP and PS seismic data (Figure 4.16).

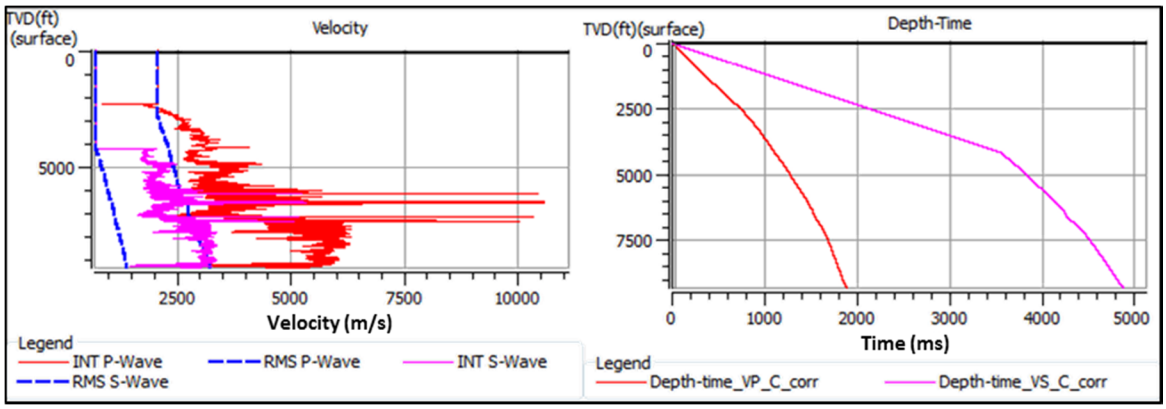

Figure 4.16: Velocity field model used for the domain conversion. From left to right, P-wave and S-wave RMS and interval velocities, depth-time curve corresponding to the corrected P-wave velocity log (red), the depth-time curve corresponding to the corrected S-wave velocity log (purple).

The interpreted PP seismic horizons do not match the PS data anywhere but at the well location which indicates that the Vp/Vs ratio is changing laterally and it needs to be extrapolated through the entire seismic survey through the PP-PS horizon matching

process. Figure 4.18 shows the events matched at the well location and the correct horizons tracked and interpreted on the PS seismic. These horizons can be used to match the times between the PP and PS seismic data and determine the spatial changes in Vp/Vs ratio. The horizons corresponding to the tops of Lodgepole and Three Forks Formations are interpreted as zero-crossing (1780 ms) and peak amplitude (1880 ms), respectively. The top of Bakken Formation is picked as an amplitude trough around 1860 ms in PP time. Only the Lodgepole and Three Forks horizons picked in both volumes were used for the event-matching process because small picking errors in horizons that are very close together such as the amplitude trough and the top of Three Forks can cause large errors in the estimated Vp/Vs (Ruiz, 2016).

It is well stablished that similar vertical wavelength ranges must be preserved in multicomponent data (Garotta and Granger, 1988) and that wavelengths of P- and S-waves must match in order to sample the reflectivity sequence in an equivalent manner (Gaiser, 1996). According to Gaiser and Verm (2011), this has not been properly achieved in Vp/Vs analyses where is common to perform a complementary band-pass filtering of P-waves and reflected P-to-S-waves (C-waves) (Gaiser, 1996), or where the C-wave is scaled through a least-square functions in order to match the P-wave amplitudes (Fomel and Backus, 2003). As a frequent approach, the PP data are filtered to the frequency of the PS data to reduce the uncertainty of horizon picking. However, reducing the bandwidth of the PP seismic for it to be similar to the PS data will translate to a loss of vertical

resolution. The Bakken Formation and its thin members of interest may not be correctly interpreted even after improving seismic resolution with the PP-PS joint inversion. The comparison between frequency spectra from the PP seismic data in PP time and the PS seismic data converted to PP time supports this statement. The apparent frequency content of the PS data increases when converted to PP time indicating that the PS volume may help increase resolution in the joint inversion results while incorporating the shear-wave information into the analysis (Figure 4.17). Based on that, the amplitude trough is picked as a reference location for the top of the Bakken Formation but the actual interpretation of its shales and siltstones depths will be done later on in the inversion results.

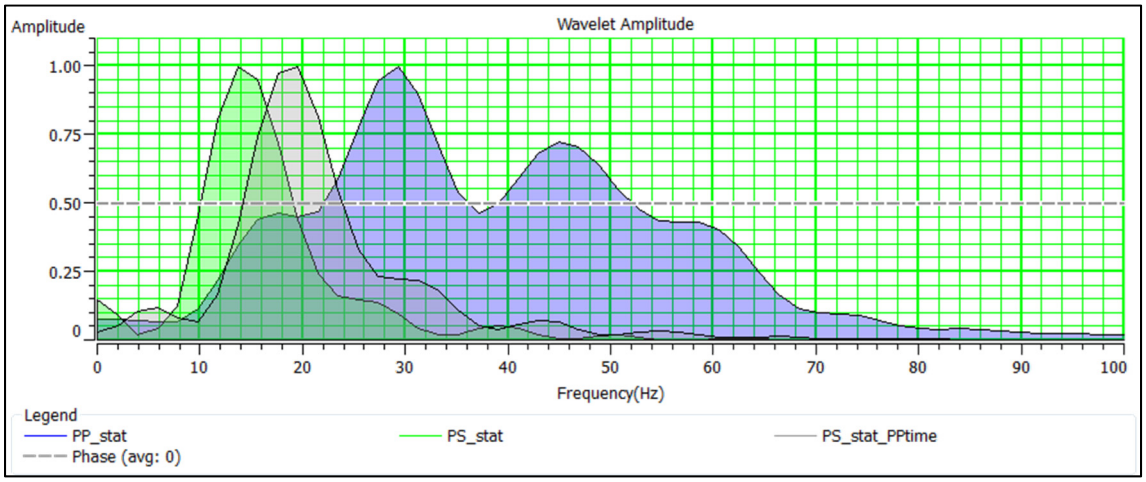

Figure 4.17: Comparison between frequency spectra from the PP seismic data in PP time (blue), the PS seismic data in PS time (green), and the PS seismic data converted to PP time (gray). Note the increase in both bandwidth and dominant frequency of the PS data when converted to PP time.

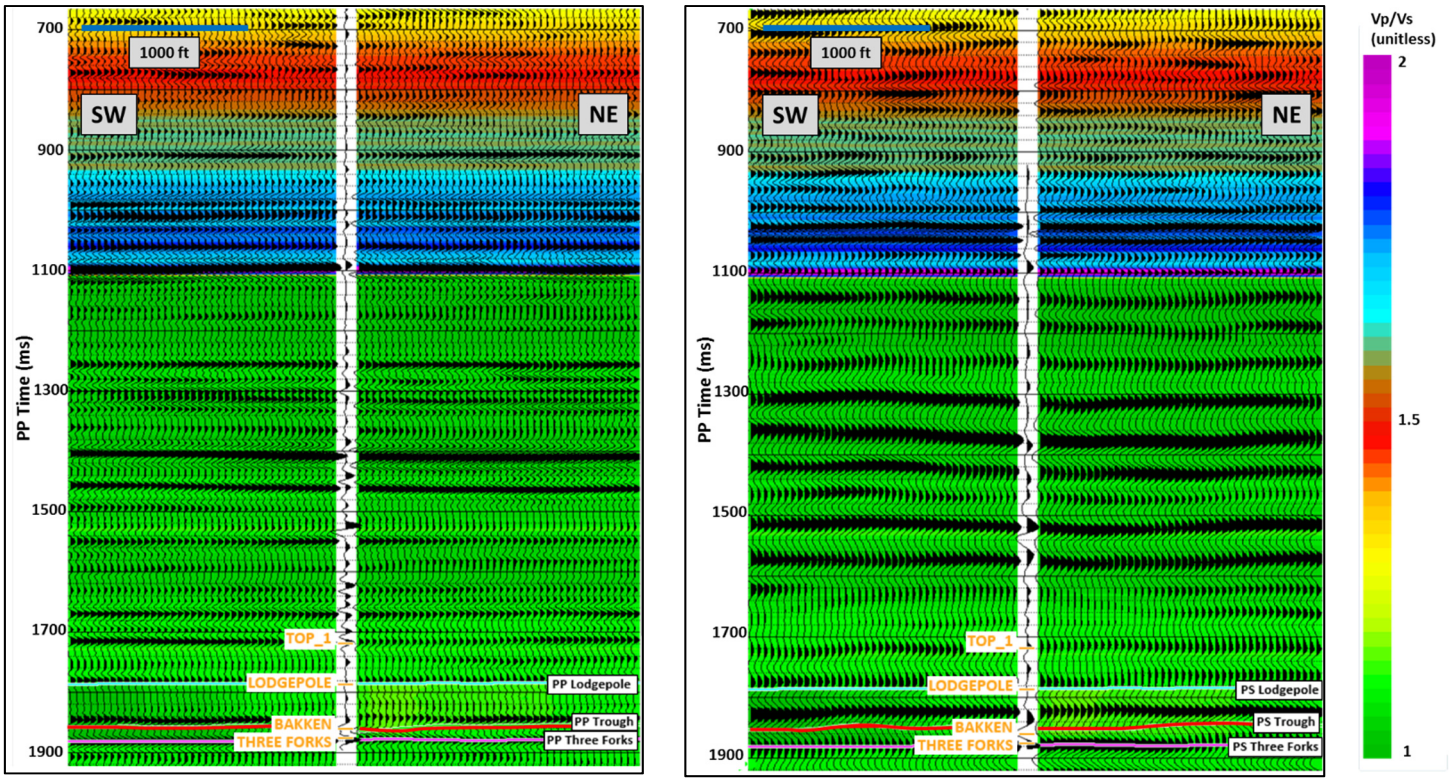

Figure 4.18: PP-PS horizon picking and event registration. PP section on PP time (left), PS section on PP time (right) and their interpreted horizons of the amplitude trough of interest and the Lodgepole and Three Forks Formations. The inserted curves correspond to the PP and PS synthetic traces at the well V-1 location.

4.3.3 Low-frequency models and joint inversion analysis

The generation of low-frequency models follows a similar procedure as the PP post-stack inversion process. After determining the layer model of reflection coefficients with the source wavelets and PP and PS seismic data, a set of few homogeneous plane layers is assumed to determine only the major impedance boundaries. The resulting P and S impedances, densities and Vp/Vs ratios are calculated ensuring that the model meets the constraints. The P-wave velocity and density low-frequency models are obtained by extrapolating the well logs using the Lodgepole and Three Forks horizons as a reference. The resulting Vp/Vs from the event-matching process is then used to calculate the S-impedance model. The models were filtered using a 15-20 Hz high-cut filter to add the low-frequency content, constraint the inversion and overcome instability.

The non-uniqueness of the inversion problem is constrained by using a background trend that is described by the linear relationship between the natural logarithm of P-impedance (Zp) and both S-impedance (Zs) and density (ρ) (Russell, 2014) that follow these equations, respectively:

$$\ln(Zs) = k\ln(Zp) + k_c + \Delta\ln(Zs) \tag{4.6}$$

$$\ln(\rho) = m(Zp) + m_c + \Delta\ln(\rho) \tag{4.7}$$

Where coefficients $k, k_c, m,$ and m_c are linear-fitting parameters corresponding to the background trend. $\Delta\ln(Zs)$ and $\Delta\ln(\rho)$ correspond to the deviations from the linear fit. The inversion tries to solve for those deviations related to the non-water saturated rocks. Table 4.3 shows the coefficients values and their associated cross-plots are seen in Figure 4.19.

k	k_c	m	m_c
0.870634	0.789678	0.230359	-1.51036

Table 4.3: Background linear trend coefficients used in the PP-PS post stack joint inversion.

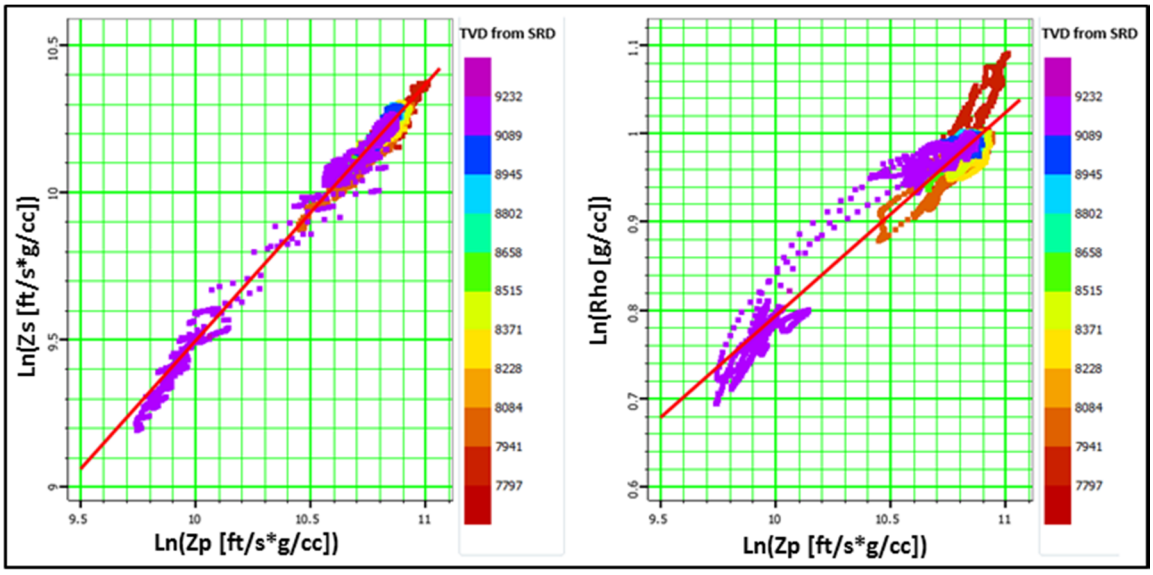

Figure 4.19: Cross-plots between the natural logarithm of P-impedance (Zp) and both S-impedance (Zs) and density (ρ) colored by the true vertical depth. The linear regressions of both plots are the background models for the inversion.

The inversion results at the Well V-1 are seen in Figure 4.20. The PP stacked seismic data are assumed to be equivalent to a PP angle-gather at zero degrees and that the PS

stack is equivalent to a PS angle stack at 20 degrees. The inversion window corresponds to 500 ms (from 1500 to 2000 ms in PP time) and its resulting log (in red) is overlying the impedance log-filtered to the approximate seismic frequency plus the model frequency band (0-0-50-60) (in blue). The RMS error for each inverted property is calculated in the entire window. There is an excellent agreement between the well-logs and the inverted results, especially for the Bakken and Three Forks Formations. However, the Upper, Middle and Lower Bakken members that are below seismic resolution are not completely picked up by those inverted properties which questions the feasibility of those inverted properties to accurately map the TOC intervals in the Bakken Formation thin members.

The line going through the well V-1 in Figures 4.21 to 4.24 shows the generated low-frequency P-impedance, S-impedance, density, and Vp/Vs models and their corresponding inverted volumes. Cold colors represent high property values and warm colors represent low property values. In both cases, the resolution is improved compared to their respective model and the values of P-impedance and Vp/Vs are accurately represented in the inversion for the Lower Bakken member at the vicinity of the vertical well with around 28,000 ft/s*g/cc and 1.71, respectively. Note that when compared the P-impedance inverted results of the post-stack PP inversion and the PP-PS joint inversion, the error still decreases by 14% when incorporating the shear-wave information in the inversion process.

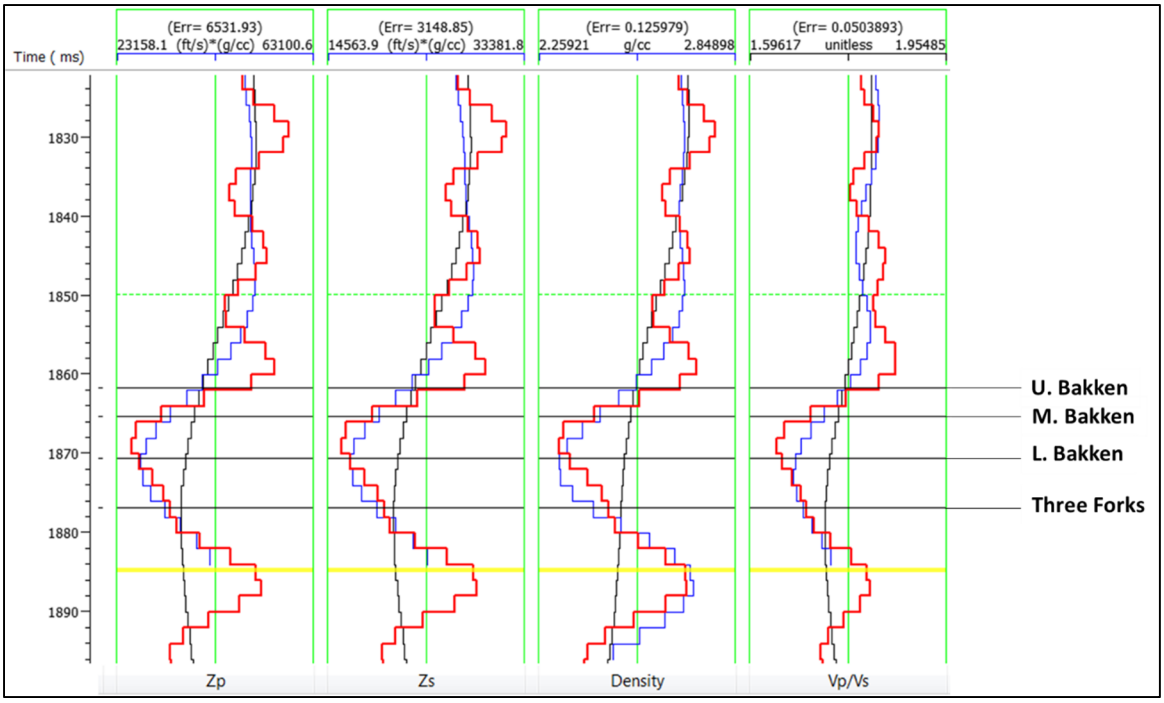

Figure 4.20: PP-PS post-stack joint-inversion results at the well V-1 location. The initial models, filtered original logs, and the inverted results correspond to the black, blue, and red logs, respectively. Note how the inverted P-impedance, S-impedance, density, and Vp/Vs follow the general trend of the Bakken Formation. P-impedance, S-impedance, and density inverted results seem to average the original response of Bakken Formation due to the effect of the low-frequency model.

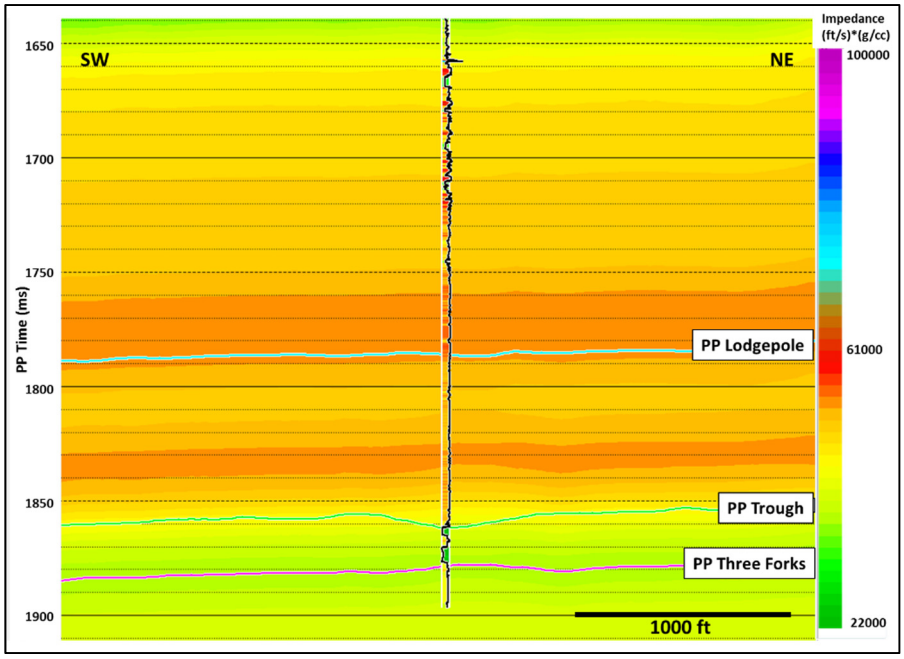

(a)

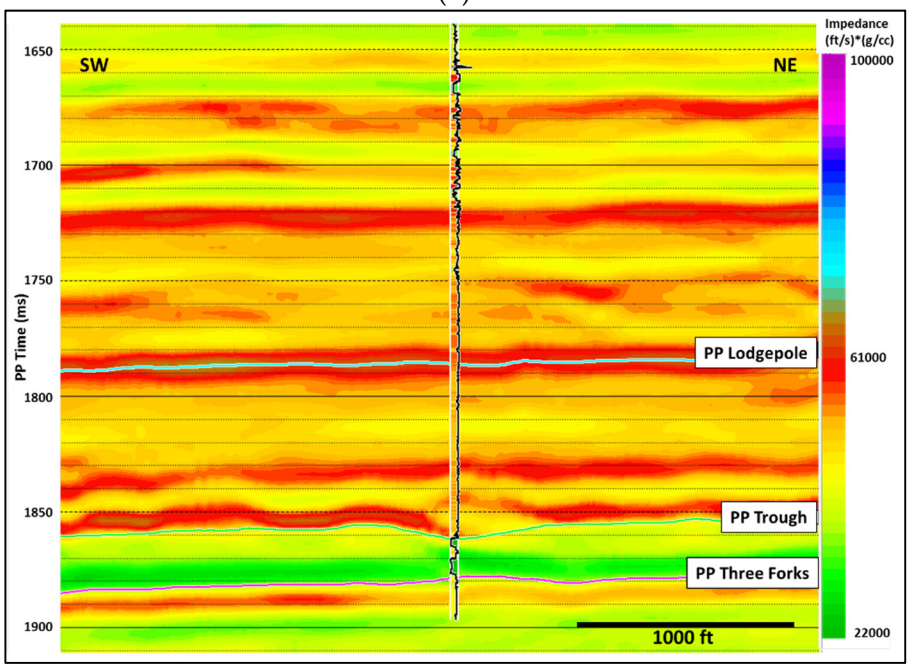

(b)

Figure 4.21: SW-NE seismic sections of (a) filtered P-impedance low-frequency model and (b) inverted P-impedance going through the Well V-1 location. The displayed logs correspond to the computed P-impedance.

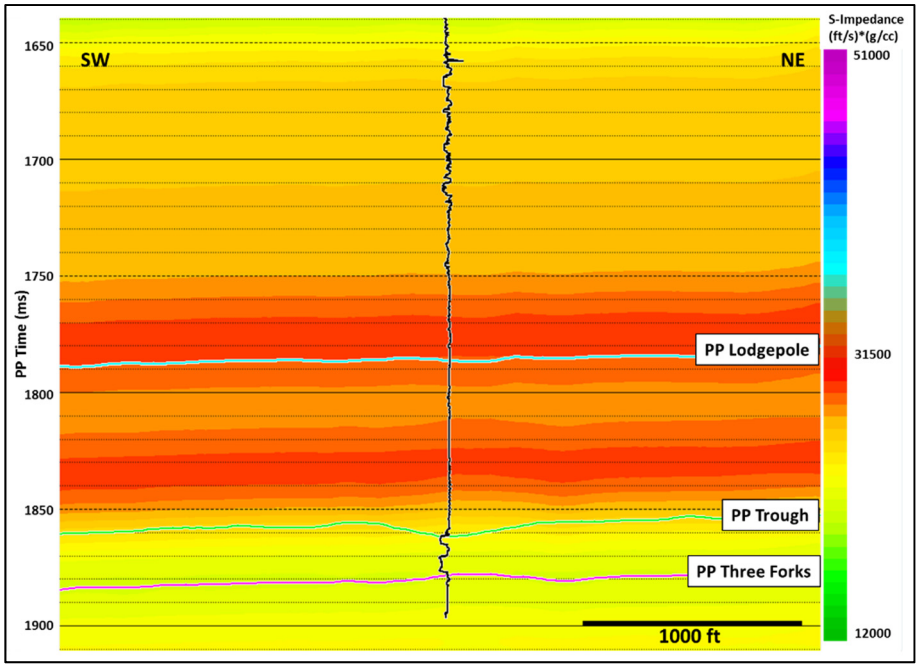

(a)

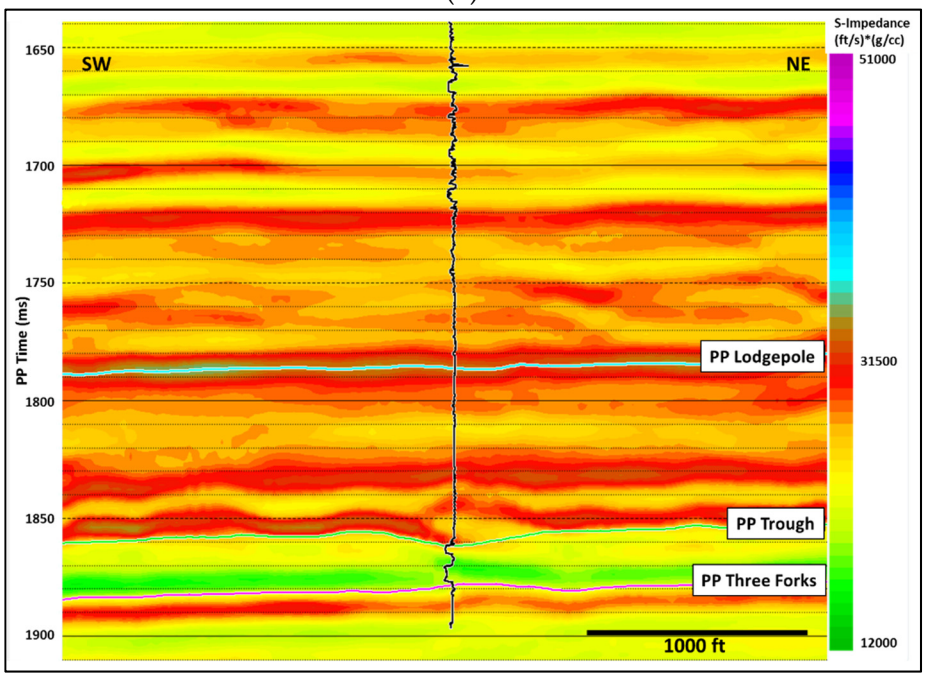

(b)

Figure 4.22: SW-NE seismic sections of (a) filtered S-impedance low-frequency model and (b) inverted S-impedance going through the Well V-1 location. The displayed logs correspond to the computed S-impedance.

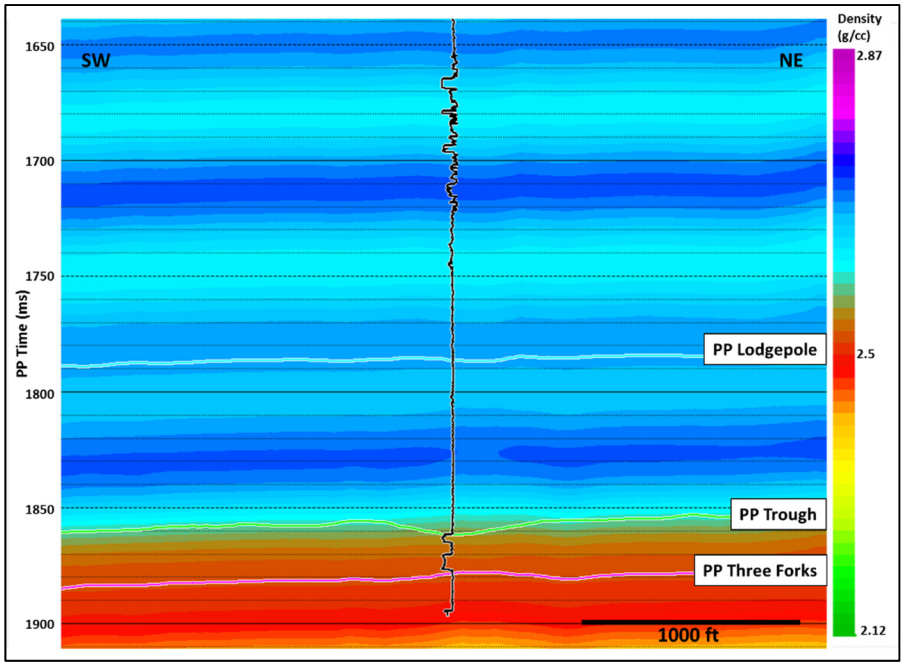

(a)

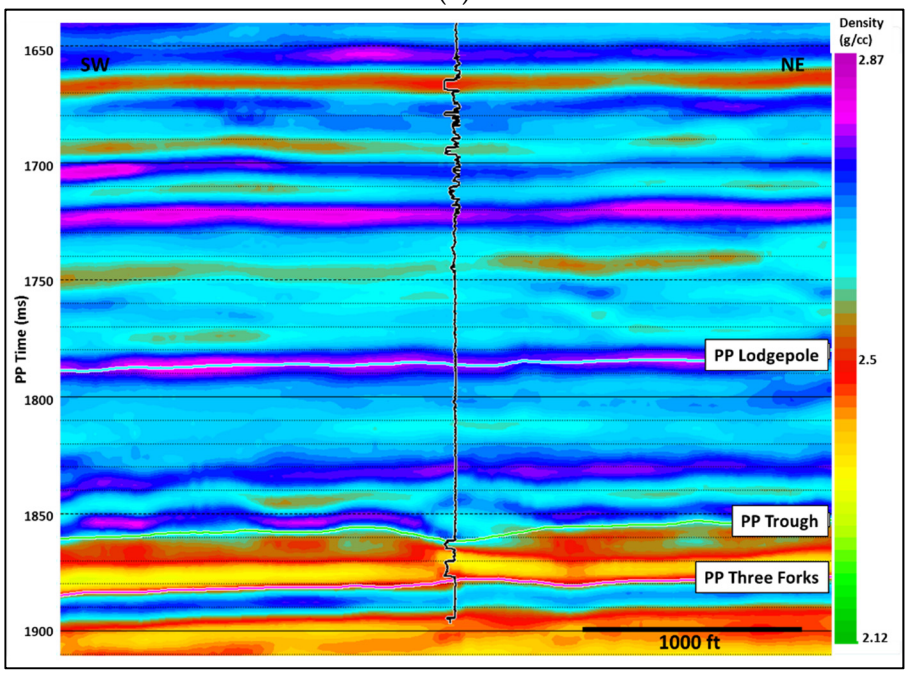

(b)

Figure 4.23: SW-NE seismic sections of (a) filtered density low-frequency model and (b) inverted density going through the Well V-1 location. The displayed logs correspond to the density log.

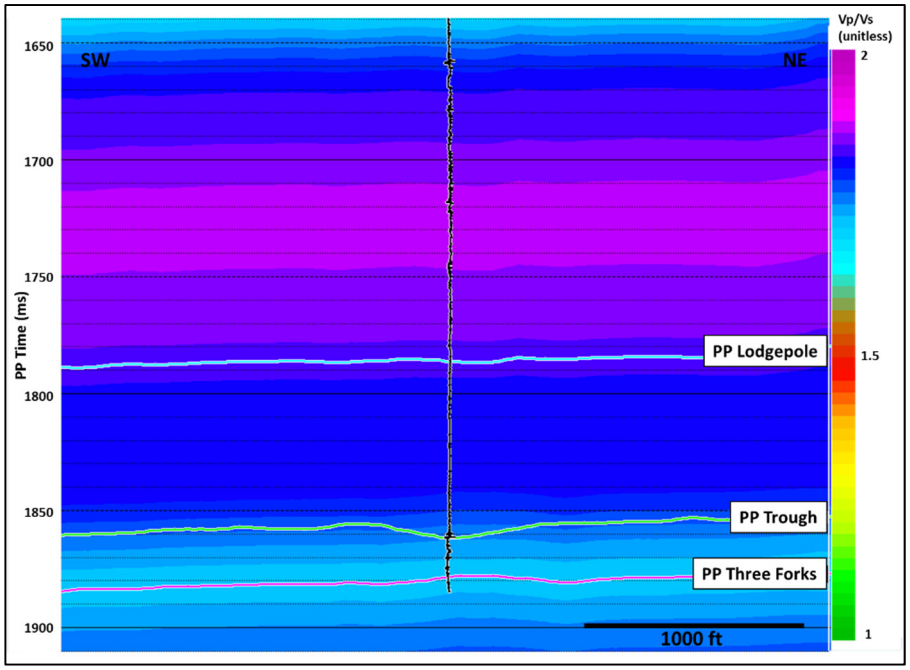

(a)

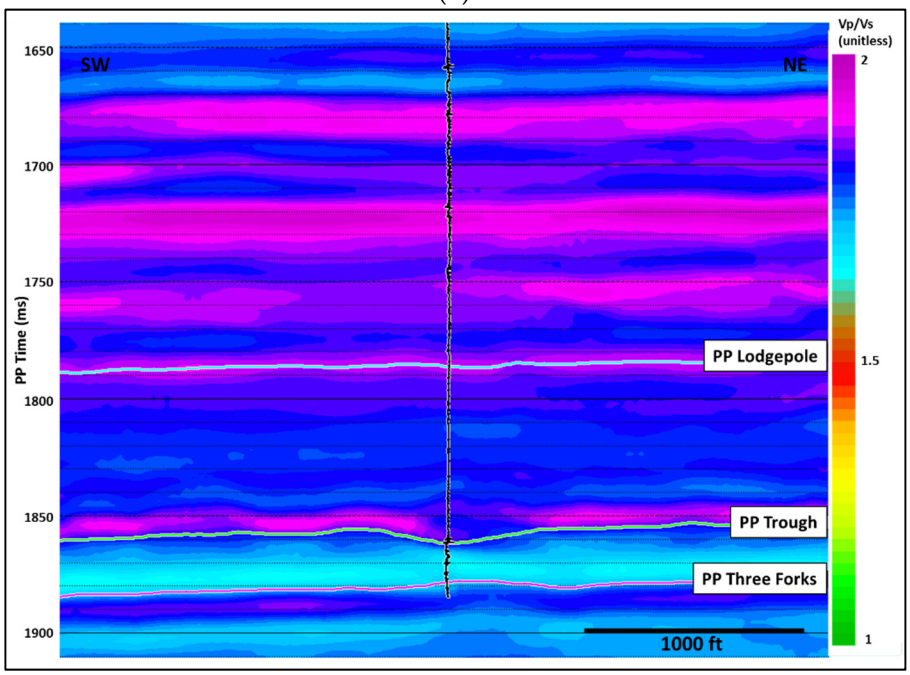

(b)

Figure 4.24: SW-NE seismic sections of (a) filtered Vp/Vs low-frequency model and (b) inverted Vp/Vs going through the Well V-1 location. The displayed logs correspond to the computed Vp/Vs.

The difference between the PP seismic and the PP synthetic at an inline going through the well location is seen in Figure 4.25, Note that the amplitude of the traces corresponding to the residual seems to be quite high which differs from the expected results. In the case of the joint inversion, the real seismic and the synthetic seismograms are considerably different for the inversion to be completely valid. The differences of the frequency content of both PP and PS seismic data may be causing these significantly high trace errors. However, filtering the bandwidth of the PP seismic for it to be similar to the PS data for the joint inversion analysis, not only reduces considerably the vertical resolution but also results in poorly inverted P-impedance, S-impedance, density and Vp/Vs properties that follow the trend of the low-frequency models instead of capturing the respective well log information (Figure 4.26).

Figure 4.27 shows the comparison between the PP, PP filtered and PS seismic sections in PP time at the vicinities of the vertical well. A high-cut filter is applied to the PP seismic (0-0-20-30) to mimic the bandwidth of the PS data. Note how most of the P-wave data are filtered which indicates that the PS frequency content is not sufficient for the joint inversion. The statistical wavelet extracted from the PP filtered seismic is seen in Figure 4.28. On the other hand, even though the processing of the stacked data managed to preserve the amplitude of both the PP and PS components, two different imaging techniques were applied. To test the feasibility of these domain in discriminating areas below seismic resolution by means of post-stack inversion and to stablish a correlation

between the PP and PS stacked lines, a cross-plot of PP amplitude vs. PS amplitude was generated for the Bakken Formation interval (Figure 4.29). The cross-plot shows how different both amplitudes are. There appear to be no relationship between the two of them indicating that a statistical estimation or inversion is a better attribute that could be potentially used as the next step of the PP-PS joint inversion for the thin-beds characterization in the study area.

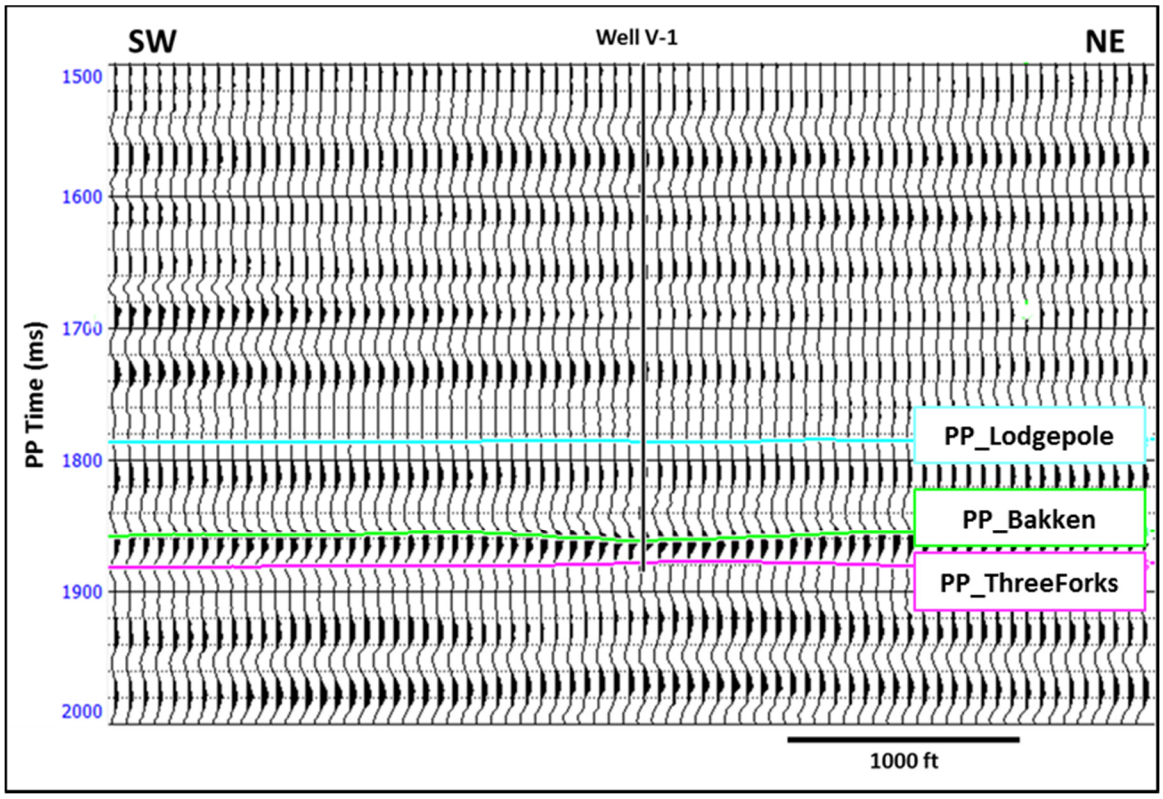

Figure 4.25: Difference between the PP seismic and the PP synthetic at the line going through the well location. Note that the amplitude of the traces is quite high. The real seismic and the synthetic seismograms are considerably different (error trace equal to 0.391).

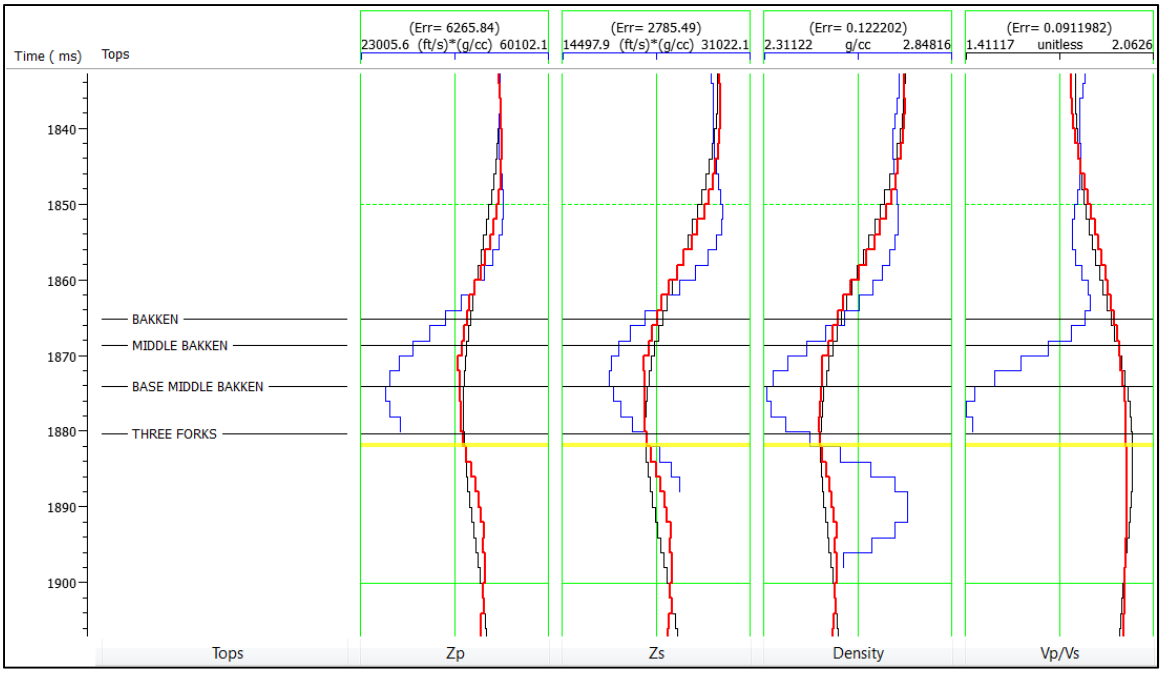

Figure 4.26: PP-PS post-stack joint-inversion results at the well V-1 location using the PP stacked seismic filtered to the approximate seismic frequency of the PS data. The initial models, filtered original logs, and the inverted results correspond to the black, blue, and red logs, respectively. Note how the inverted P-impedance, S-impedance, density, and Vp/Vs follow the general trend of the low-frequency models instead of capturing the respective well log information in the Bakken Formation.

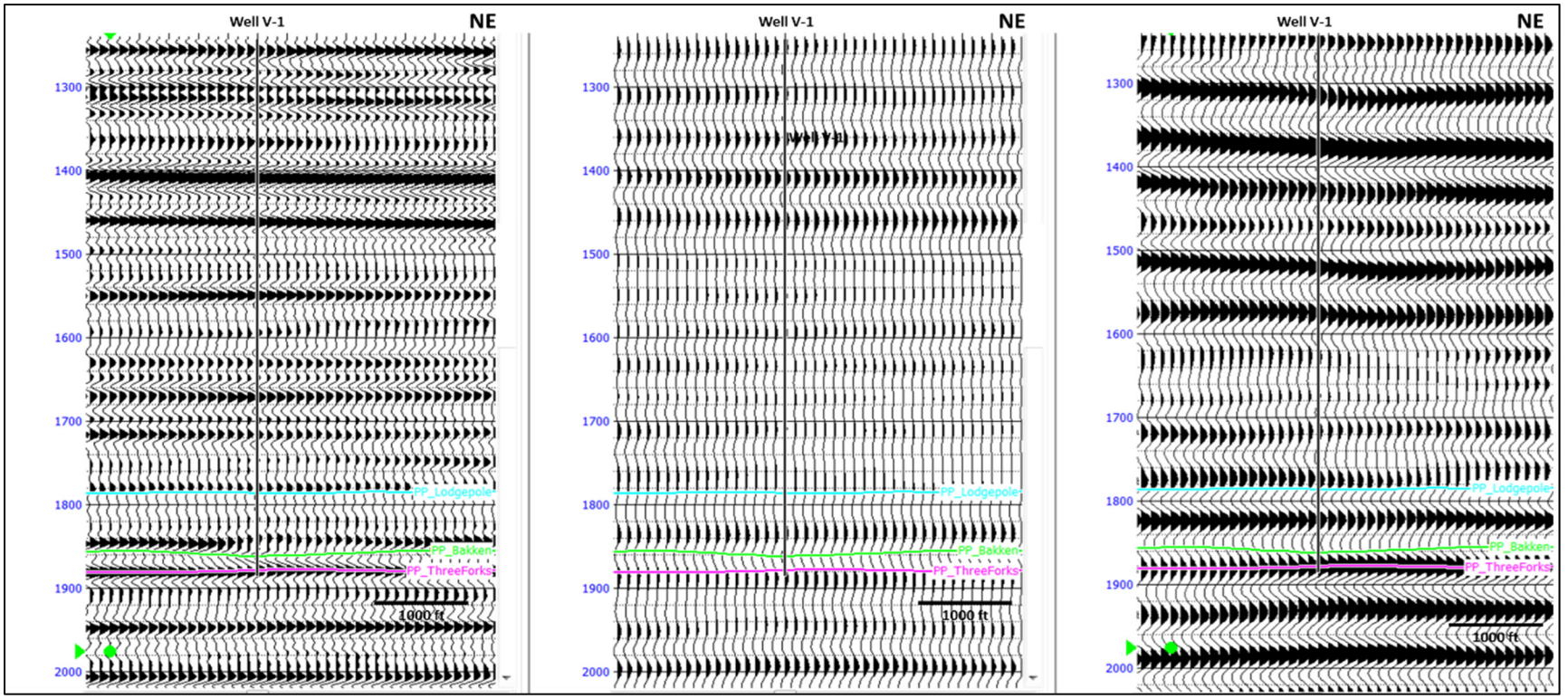

Figure 4.27: Comparison between the PP, PP filtered and PS seismic sections in PP time at the vicinities of the vertical well. From left to right, the PP seismic data, PP seismic data filtered to the approximate seismic frequency of the PS data, the PS seismic data. Note how most of the P-wave data are filtered which indicates that the PS frequency content is not sufficient for the joint inversion.

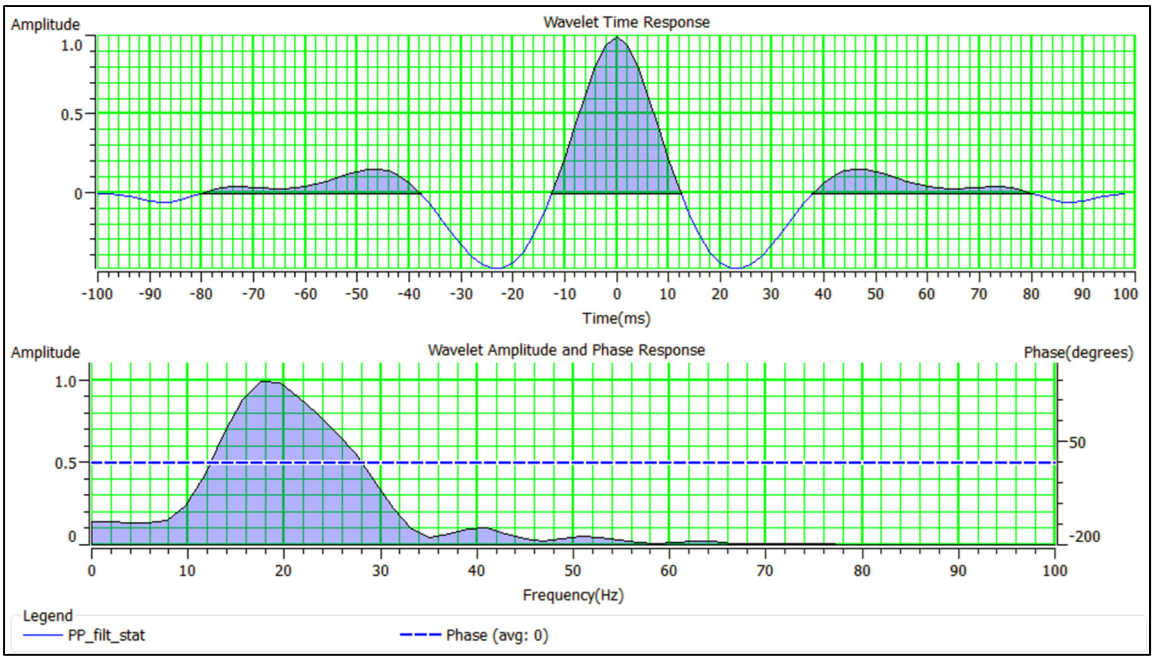

Figure 4.28: PP statistical wavelet extracted from the PP seismic filtered to the approximate frequency of the PS seismic data. The corresponding frequency spectrum is also shown. The wavelet extraction is performed in a window from 1500 to 2000 ms (a 500 ms window length). The dotted shows a zero-phase angle.

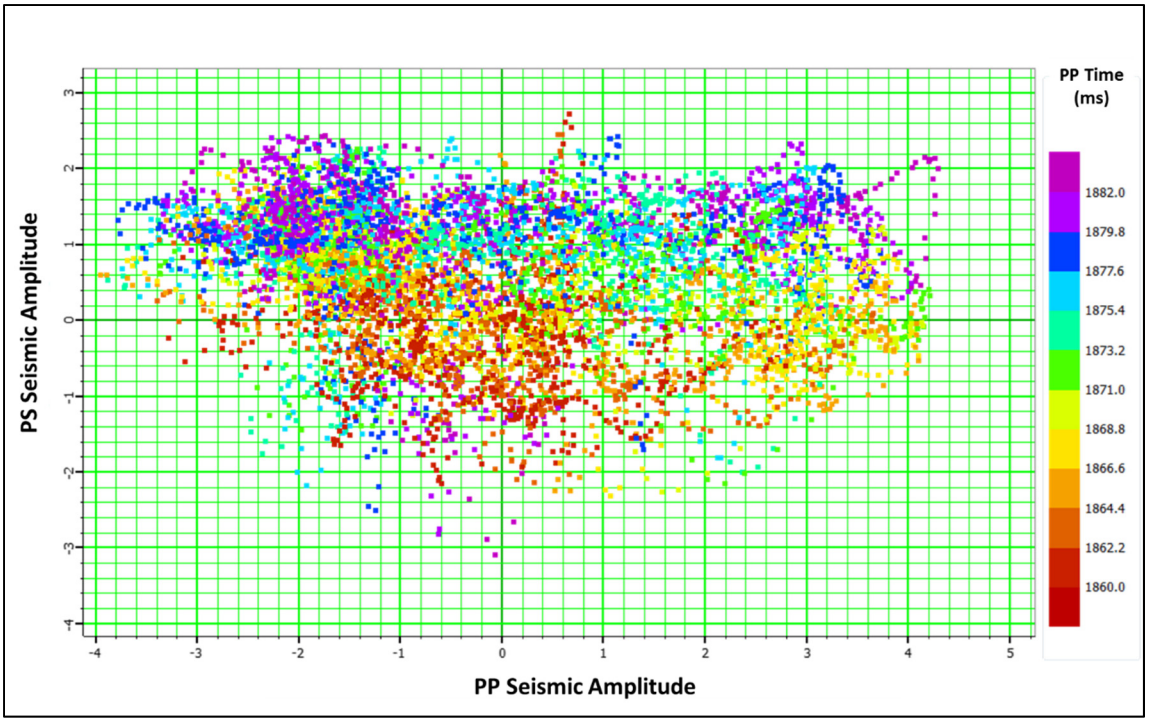

Figure 4.29: PP seismic amplitude vs. PS seismic amplitude cross-plot of the Bakken Formation interval, colored by PP time. The amplitude values are normalized. There appear to be no relationship between the two of them indicating that a statistical estimation or inversion is a better attribute that could be potentially used as the next step of the PP-PS joint inversion for the thin-beds characterization in the study area.

The PP-PS joint inversion computes inverted logs that fairly match the original (filtered) logs. However, the high residual from the synthetic seismograms and the seismic data suggest that the inversion is not completely feasible for using the inverted-density to map the TOC intervals in the Bakken Formation. A post-stack inversion of PP data was also performed and shows an excellent agreement with the original P-impedance log suggesting that not only the statistical wavelet extraction from the PP data and the P-wave log correlation for the seismic-to-well tie, but also the frequency content, and the seismic quality of the PP stack are indeed adequate to predict elastic properties for the Lodgepole, Bakken and Three Forks Formations. Thus, a PP-PS joint inversion using an enhanced PS data with similar frequency content than that of the PP seismic may not merely reduce the residuals but improve the vertical resolution as well. In this case, Bakken Formation and its thin members of interest may be recognizable, interpreted and correctly characterized in terms of the vertical/spatial distribution of impedances and density.

Since the estimation of elastic properties by means of inversion analysis is data-driven and frequency-dependent, and the study aims to investigate the properties that characterize the thin members of Upper, Middle and Lower Bakken (below seismic resolution), a refined estimation of the elastic properties should follow the conventional PP-PS joint inversion. Therefore, a statistical approach using multi-attribute analysis and neural networks is carried out to define and delimit zones of interest.

4.4 Statistical estimation of inverted properties

As an extension of the PP-PS post-stack inversion, a well log and seismic data analysis at the well V-1 location are performed to find a relationship between both the logs and seismic which can be used to predict or estimate a volume of the log property at all the other locations of the seismic volume.

The 2D seismic line going through the vertical well location, P-impedance and density logs, the depth-time curve resulting from the well correlation and the external attributes in form of seismic data such as the low-frequency models of P-impedance and density generated in the joint inversion process are used as input for the statistical prediction of their corresponding properties in the Bakken Shale members.

As opposed to the joint inversion that employs the convolutional model, this statistical prediction determines arbitrary relationships between the logs and the seismic without needing *a priori* model. That is, the wavelet extraction is not necessary. In this case, the resolution is not limited by the seismic bandwidth, instead, it can be enhanced by neural network analysis such as the Probabilistic Neural Network (PNN). In the case of thin layers such the Bakken members, this method is a good approach for estimating its acoustic properties and relate them to TOC content and brittleness.

The general flow of the statistical analysis consists of the following steps:

1. Load well log and seismic data for training

2. Analyze the target log and seismic data at the well location to derive a statistical relationship between them (training stage)
3. Apply the derived multi-attribute relationship to the entire line to create log values throughout it (application stage)
4. Perform neural training for this relationship

The list of the attributes with the best correlation and lowest error for each of the target properties are seen in Tables 4.4 and 4.5. Note that the minimum error results from taking simultaneously five attributes that combine to discriminate subtle P-impedance and density features on the respective target logs which none of the individual attributes could predict by themselves.

The search for the group of attributes that can be combined to predict the target is done by step-wise regression process. First, a single attribute that predicts best by itself (lowest RMS error) is searched, then the best pair of attributes is determined following the same principle and so on. This is done by trial and error, solving the system of equations as many times as there are other attributes to pair up with the single attribute (Hampson-Russell, 2014).

Target property	Attributes
P-impedance	P-impedance low-frequency model (External attribute)
	Amplitude weighted cosine phase
	Instantaneous frequency
	1/ PP stack
	Filter 45/50 – 55/60

Table 4.4: List of attributes used to derive the multi-attribute relationship for P-impedance prediction in the Bakken Formation.

Target property	Attributes
Density	Density low-frequency model (External attribute)
	Quadrature trace
	Filter 35/40 – 55/50
	Derivative
	Integrate

Table 4.5: List of attributes used to derive the multi-attribute relationship for density prediction in the Bakken Formation.

To improve the P-impedance and density estimation within the Bakken Formation and increase both the predictive power and the resolution of the derived properties, the neural network capabilities are constructed with the probabilistic approach using precisely the same attributes as those used in the multi-attribute selection process as follows:

1. Performing multi-linear regression with the same five attributes
2. Smoothing the predicted log from that calculation with a smoother length given in the neural network training window

3. Predicting the high-frequency component of the logs not contained within the smooth trend (residual)
4. Adding both trends from the multi-linear regression and the predicted residual from the PNN.

The cross-correlation values and errors corresponding to the single attribute, multi-attribute regressions, and PNN processes are shown in Tables 4.6 and 4.7 for the P-impedance and density estimations, respectively. Note that higher correlations are achieved using neural networks. This is usually the case because of the non-linear nature of the PNN operator.

Application type	**Cross-correlation**	**P-impedance error (ft/s)*(g/cc)**
Single attribute regression	0.847	5980.79
Multi attribute regression	0.903	4700.45
Probabilistic Neural Network - PNN	0.974	2528.06

Table 4.6: Cross-correlation and error values for the P-impedance estimation after the single attribute regression, multi-attribute regression, and PNN. Note that the best correlation of 97% is achieved using the probabilistic neural network.

Application type	Cross-correlation	Density error (g/cc)
Single attribute regression	0.638	0.092
Multi attribute regression	0.787	0.074
Probabilistic Neural Network - PNN	0.989	0.017

Table 4.7: Cross-correlation and error values for the density estimation after the single attribute regression, multi-attribute regression, and PNN. Note that the best correlation of 98% is achieved using the probabilistic neural network.

The statistical predictions of P-impedance and density after the PNN analysis in terms of the actual property vs target property cross-plot and the corresponding original and predicted logs are seen in Figures 4.30 and 4.31. The result of using five attributes achieves a 97% in the case of P-impedance estimation and 98% in case of density estimation. After deriving the neural network relationship between the seismic and the target logs, the result is applied to the seismic line between 1720 ms to 1900 ms. Figures 4.32 and 4.33 show the resulting seismic sections colored by the statistical prediction of P-impedance and density, respectively. The results show excellent correlations with the original logs. Even though the Upper, Middle and Lower Bakken members are below seismic resolution, the statistical prediction is picking up the thin intervals with their corresponding impedance and density values.

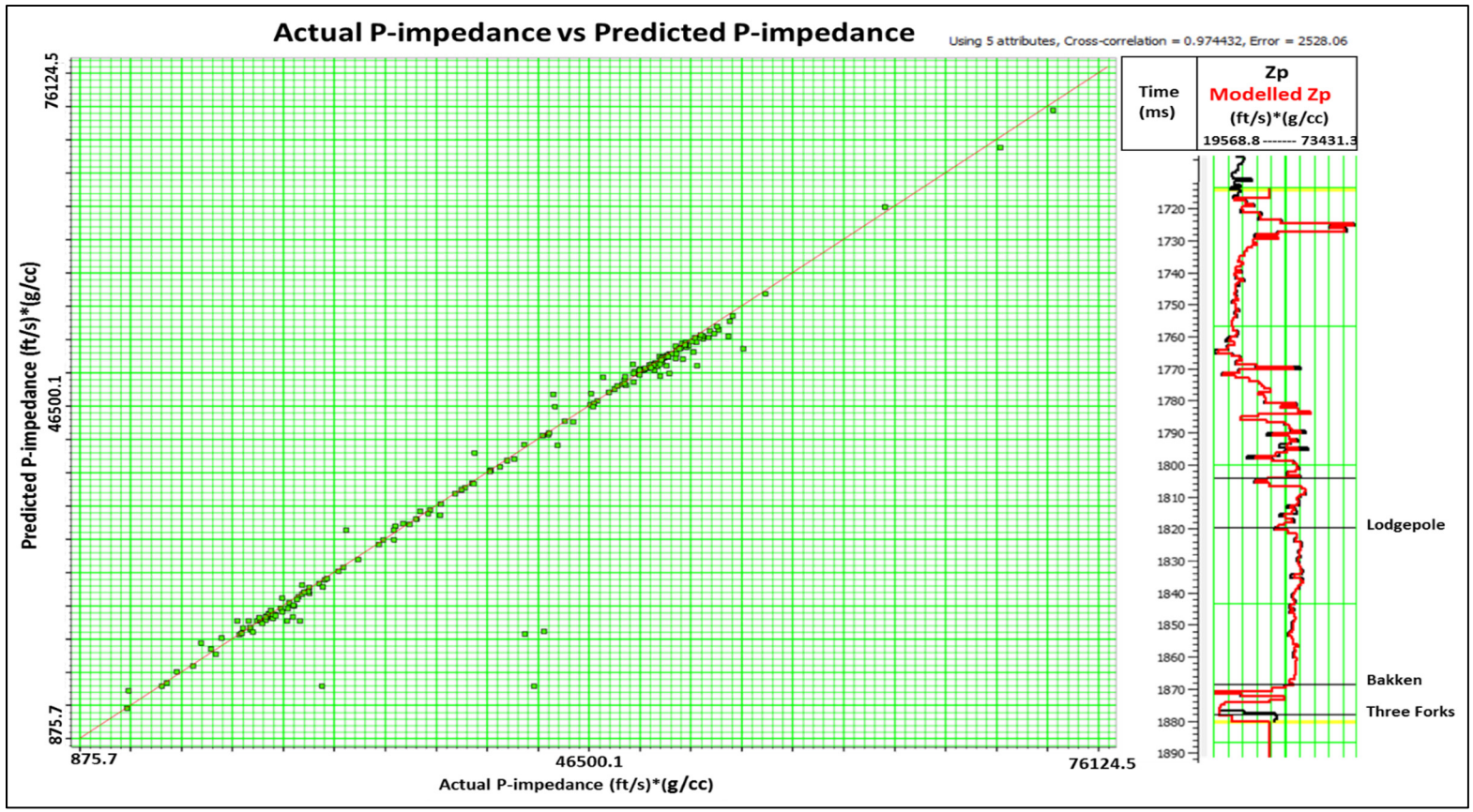

Figure 4.30: Statistical prediction of P-impedance. From left to right, actual P-impedance vs predicted target P-impedance cross-plot, and the P-impedance (Zp) log along with the predicted P-impedance log. The result of using 5 attributes achieves a 97% correlation.

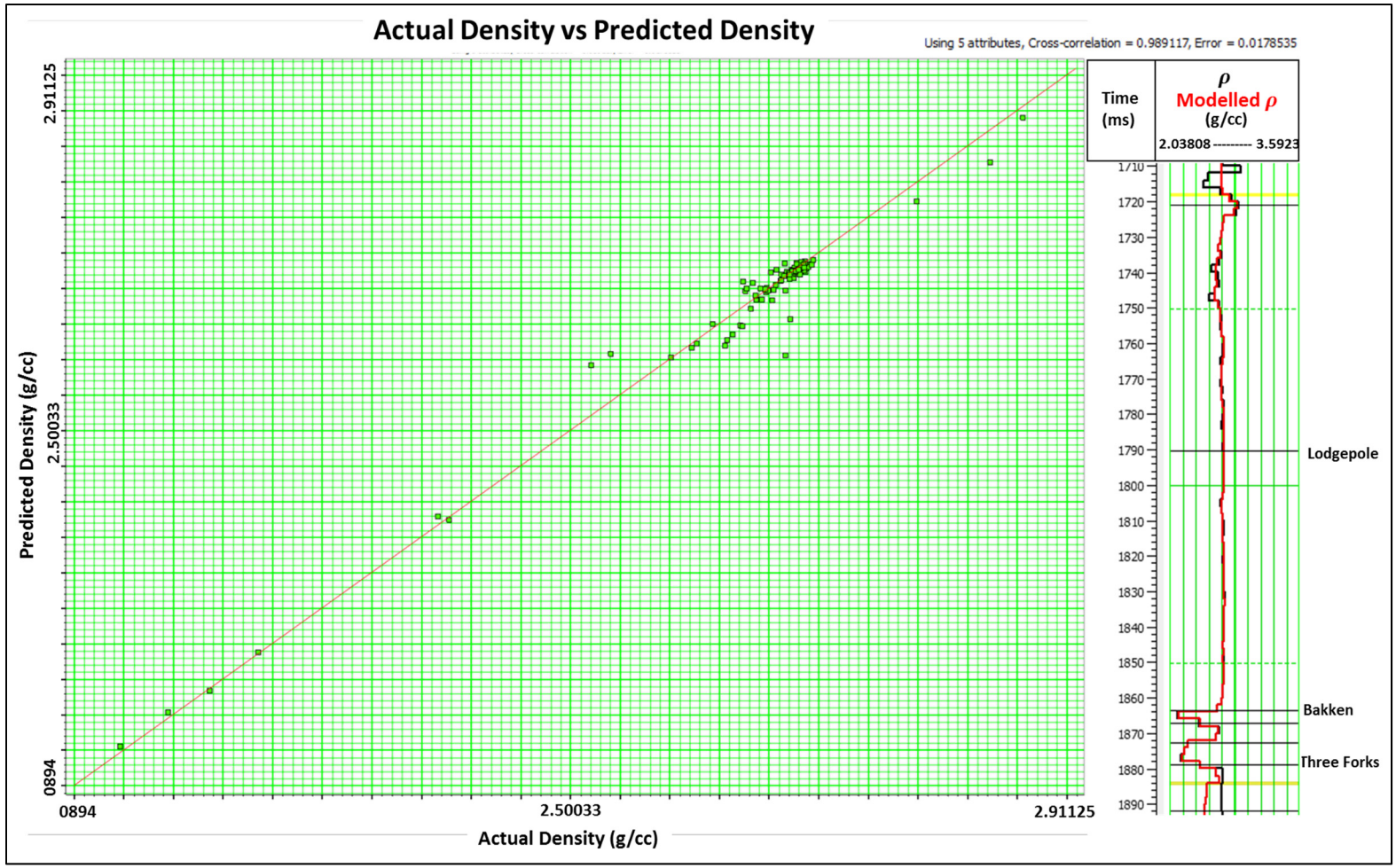

Figure 4.31: Statistical prediction of density. From left to right, actual density vs predicted target density cross-plot, and the density (ρ) log along with the predicted density log. The result of using 5 attributes achieves a 98% correlation.

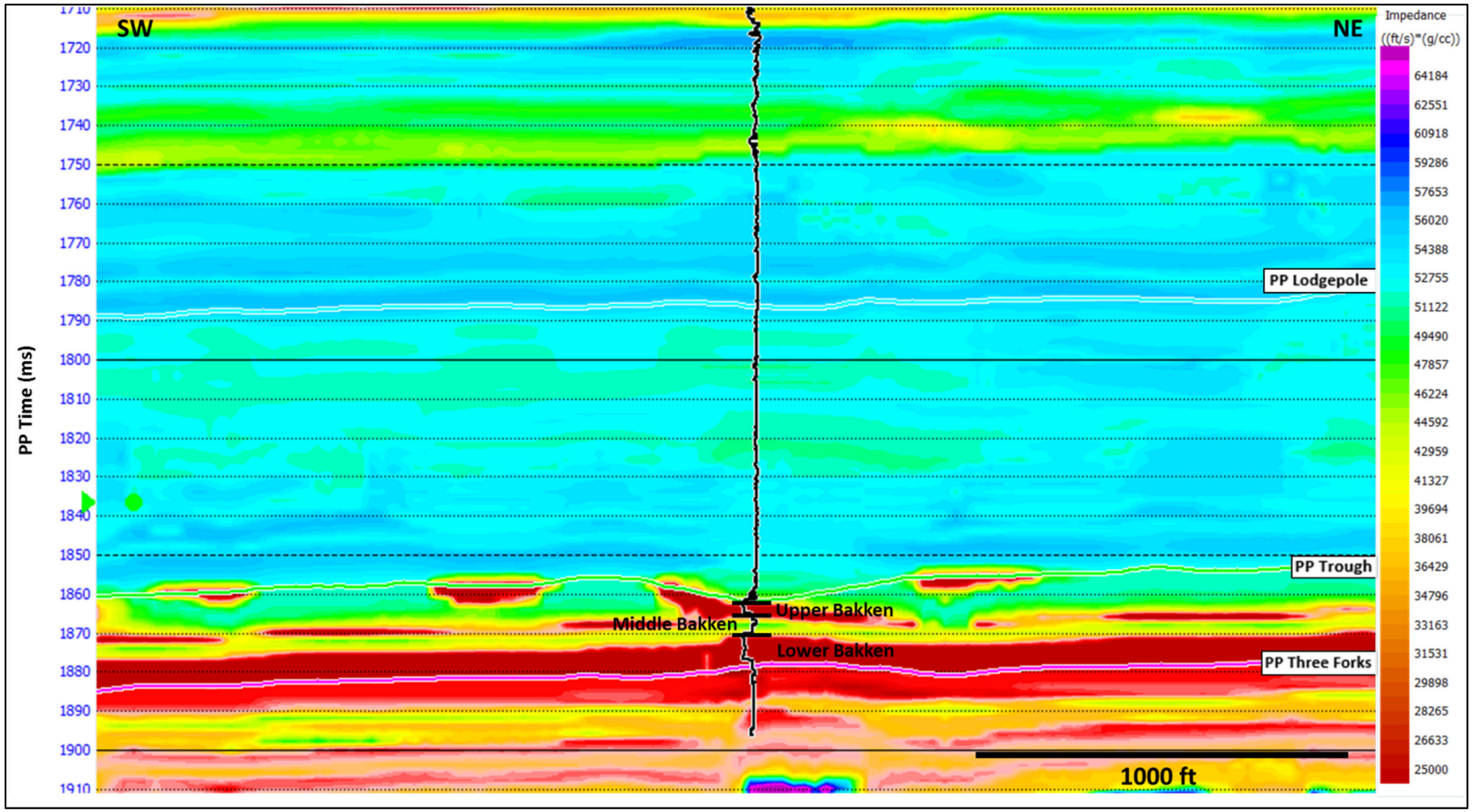

Figure 4.32: Vertical distribution of P-impedance by means of statistical prediction. The displayed log is the P-impedance log upscaled to the seismic frequency. Note how the Upper, Middle and Bakken member can be easily identified following the impedance changes.

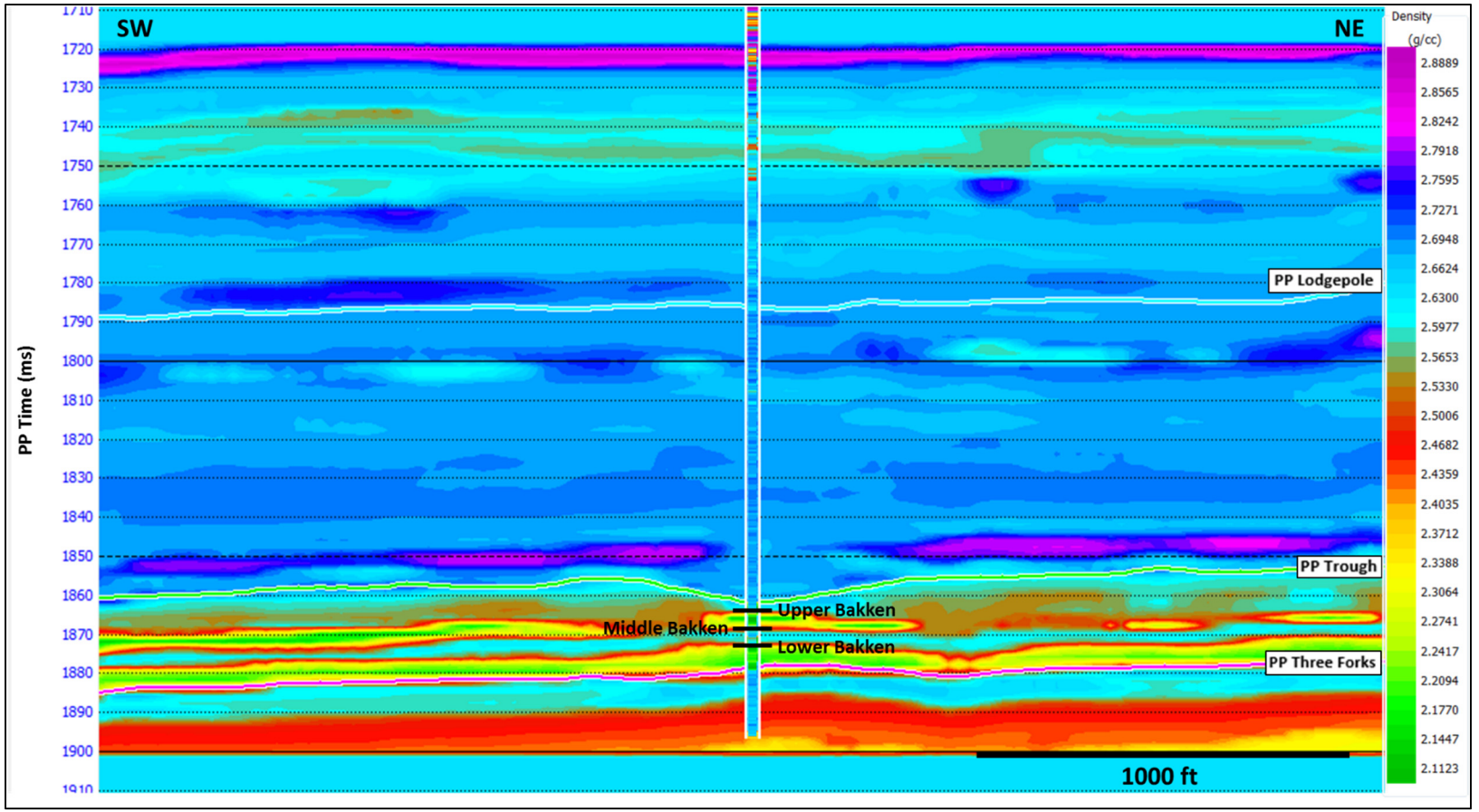

Figure 4.33: Vertical distribution of density by means of statistical prediction. The displayed log is the density log upscaled to the seismic frequency. Note how the Upper, Middle and Bakken member can be easily identified following the changes in density.

4.5 Identification of high-TOC and brittle zones within the Bakken Formation

Based on the statistical estimation of P-impedance and density and according to the analysis of the relationship between density and TOC content presented in Chapter 2, the low-frequency density models generated in the PP-PS joint inversion process are now used to start the statistical prediction and mapping of the vertical distribution of TOC content and brittleness within the Bakken Formation.

The list of the attributes with the best correlation and lowest error for each of the target properties are seen in Tables 4.8 to 4.9. Note that the minimum error results from taking simultaneously five attributes that combine to discriminate subtle TOC and brittleness features on the respective target logs.

Target property	**Attributes**
TOC	Density low-frequency model (External attribute)
	Quadrature trace
	Filter 35/40-45/50
	Second derivative
	Filter

Table 4.8: List of attributes used to derive the multi-attribute relationship for TOC prediction in the Bakken Formation.

Target property	Attributes
Brittleness	Density low-frequency model (External attribute)
	Integrate
	Derivative
	Quadrature trace
	Filter 5/10 – 15/20

Table 4.9: List of attributes used to derive the multi-attribute relationship for brittleness prediction in the Bakken Formation.

The cross-correlation values and errors corresponding to the single attribute, multi-attribute regressions, and PNN processes are shown in Tables 4.10 and 4.11 for the TOC content and brittleness estimations, respectively. The higher correlations are achieved using neural networks.

Application type	Cross-correlation	TOC error (wt. %)
Single attribute regression	-0.633	2.434
Multi attribute regression	0.772	1.997
Probabilistic Neural Network - PNN	0.990	0.432

Table 4.10: Cross-correlation and error values for the TOC content estimation after the single attribute regression, multi-attribute regression, and PNN. Note that the best correlation of 99% is achieved using the probabilistic neural network.

Application type	Cross-correlation	Brittleness error (GPa*g/cc)
Single attribute regression	0.639	88.836
Multi attribute regression	0.802	68.914
Probabilistic Neural Network - PNN	0.988	18.312

Table 4.11: Cross-correlation and error values for the brittleness estimation after the single attribute regression, multi-attribute regression, and PNN. Note that the best correlation of 98% is achieved using the probabilistic neural network.

Figures 4.34 and 4.35 show the cross-plots that relate the TOC and Brittleness properties with its respective predictions. The corresponding original and predicted logs are also seen. The result of using five attributes achieves a 99% in the case of TOC estimation and 98% in case of brittleness estimation.

After deriving the neural network relationship between the seismic and the target logs, the result is applied to the seismic line between 1720 ms to 1900 ms. Figures 4.36 and 4.37 show the resulting seismic sections colored by the statistical prediction of TOC content and brittleness, respectively. The results show excellent correlations with the original logs. Even though the Upper, Middle, and Lower Bakken members are below seismic resolution, the statistical prediction is picking up the thin intervals with accurate TOC content and brittleness.

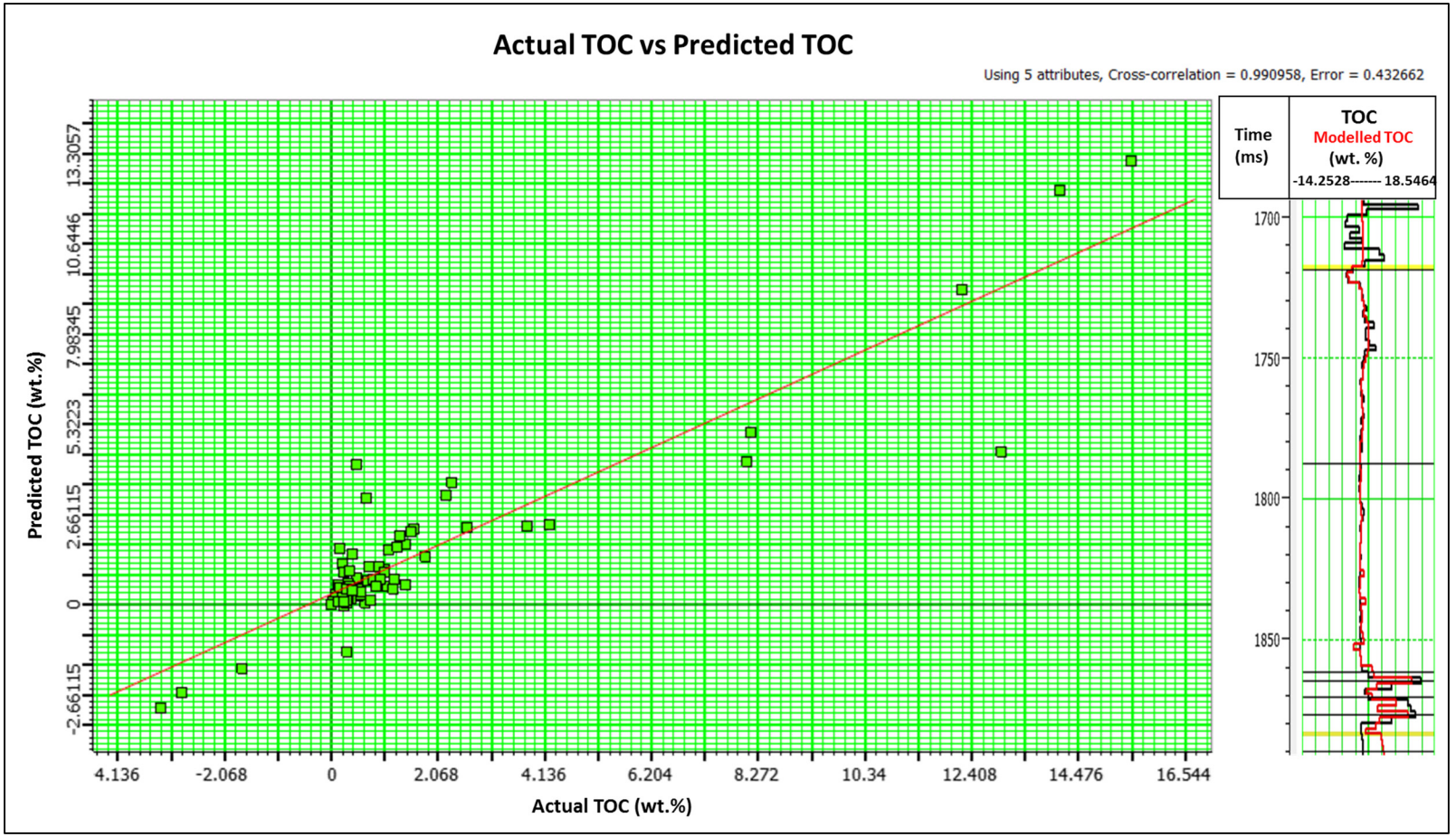

Figure 4.34: Statistical prediction of brittleness. From left to right, actual brittleness vs predicted target brittleness cross-plot, and the brittleness log along with the predicted brittleness log. The result of using 5 attributes achieves a 98% correlation.

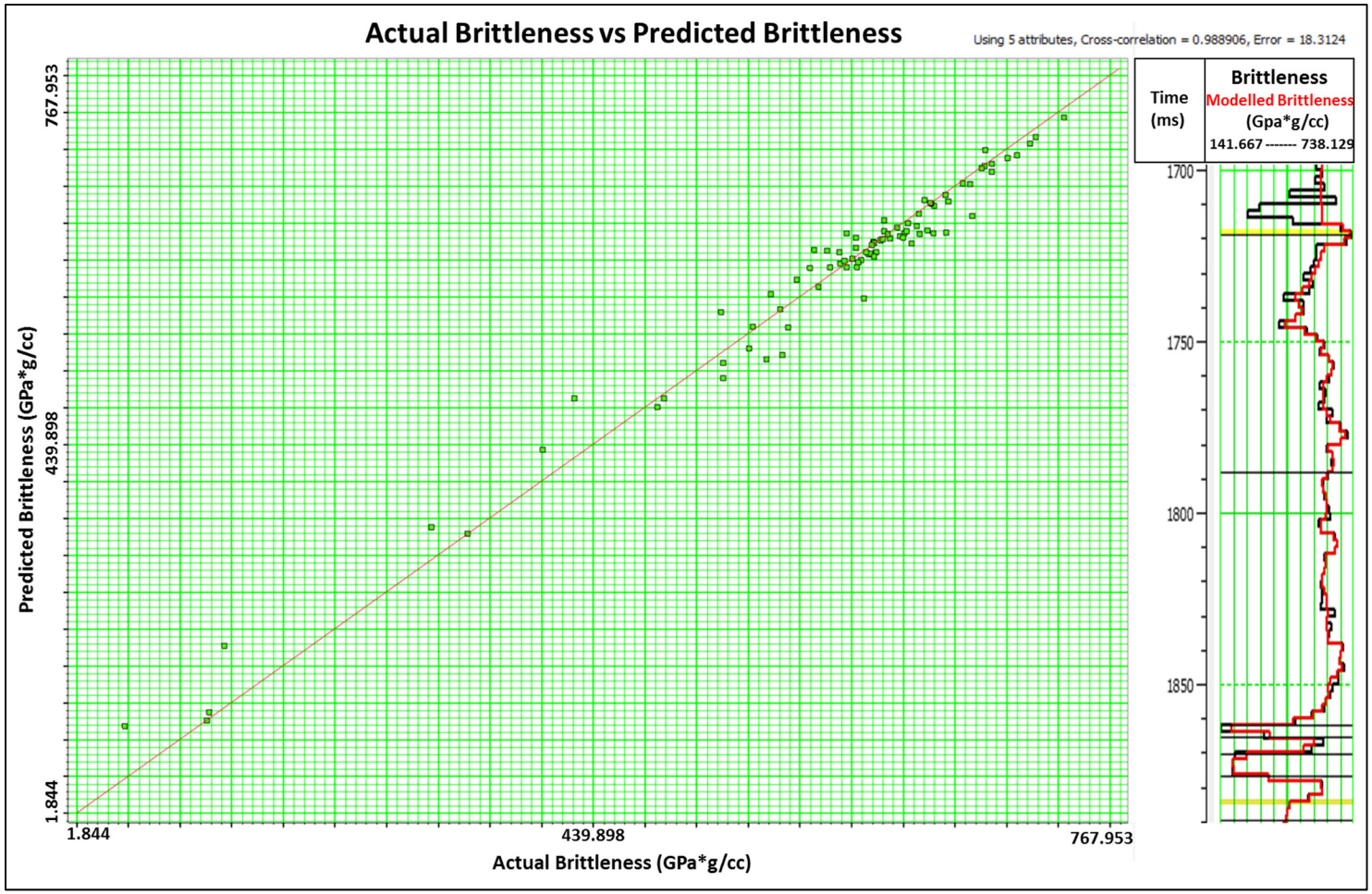

Figure 4.35: Statistical prediction of brittleness. From left to right, actual brittleness vs predicted target brittleness cross-plot, and the brittleness log along with the predicted brittleness log. The result of using 5 attributes achieves a 98% correlation.

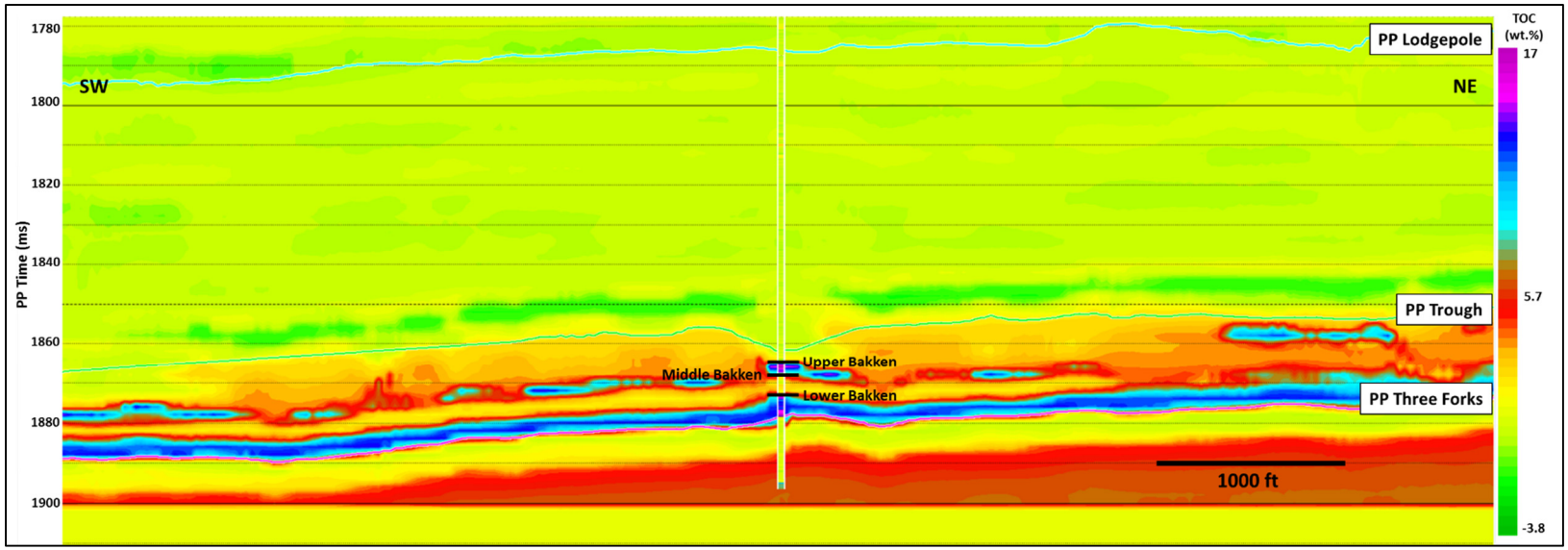

Figure 4.36: Vertical distribution of TOC content by means of statistical prediction. The displayed log is the TOC log upscaled to the seismic frequency. Note how the Upper, Middle, and Bakken member can be easily identified following the changes in TOC. The results show excellent correlations with the original log. Even though the Upper, Middle, and Lower Bakken members are below seismic resolution, the statistical prediction is picking up the thin intervals with accurate TOC content.

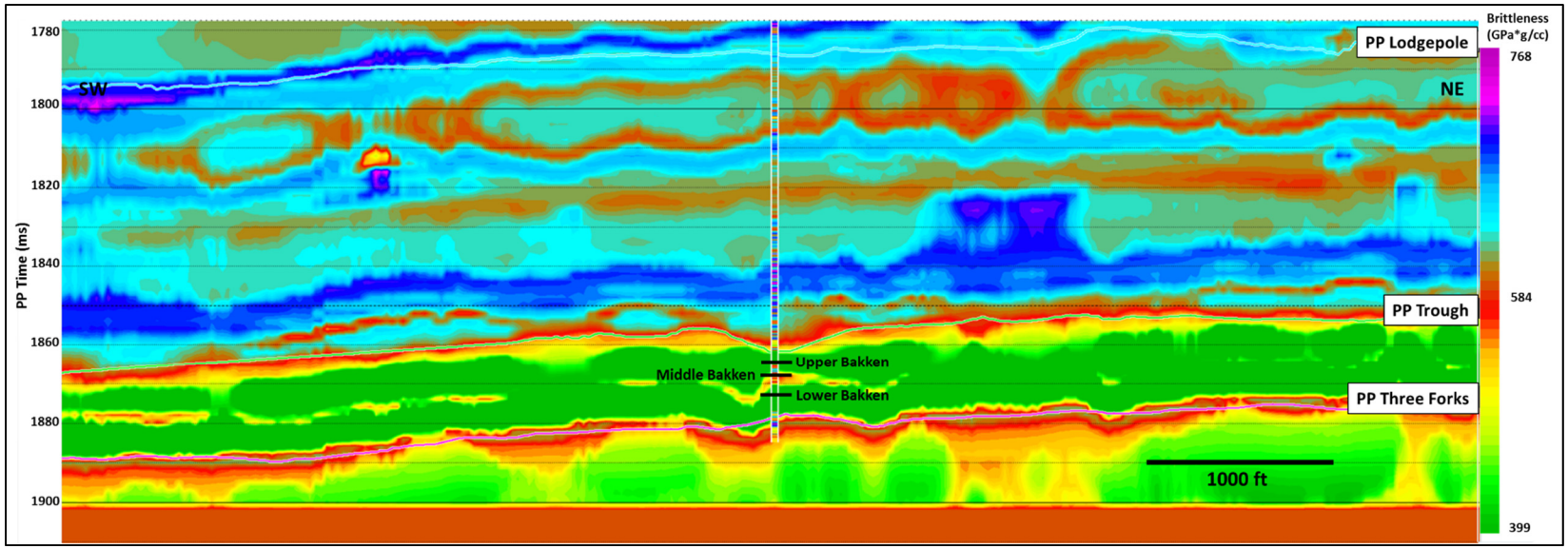

Figure 4.37: Vertical distribution of brittleness by means of statistical prediction. The displayed log is the $E\rho/\nu$ log upscaled to the seismic frequency. Note how the Upper, Middle, and Bakken member can be easily identified following the changes in brittleness. The results show excellent correlations with the original log. Even though the Upper, Middle, and Lower Bakken members are below seismic resolution, the statistical prediction is picking up the thin intervals with accurate brittleness value.

To further refine the location of the two organic-rich units, brittle zones and brittle facies within the Bakken Formation, cross-plots between density vs. acoustic impedance, Vp/Vs and TOC, are generated to aid in the mapping of the vertical distribution of the "hot" Upper Bakken and "hot" Lower Bakken according to the property ranges resulting from the cross-plot analysis in chapter 2 (Table 4.12).

Organic-rich units	**ρ (g/cm^3)**	**TOC (wt.%)**	**Vp/Vs**	**AI (g/ cm^3*ft/s)**
U. Bakken	2.0-2.15	> 14	1.65 - 1.75	<20,000
L. Bakken	2.2-2.30	10 - 13		20,000 – 25,000

Table 4.12: Density, TOC content, Vp/Vs, and acoustic impedance ranges that defined the two organic-rich zones of the Upper Bakken and Lower Bakken in the study area.

The vertical distribution of density, acoustic impedance, Vp/Vs and TOC content corresponding to both the "hot" Upper Bakken and "hot" Lower Bakken are seen in Figures 4.38 to 4.40. According to Perez (2013), low TOC zones are more brittle. Cross-plotting the results of the statistical estimation of density and TOC allows the location of low-TOC (< 7.5 wt.%) and high-brittle (> 400 GPa*g/cc) areas (Figure 4.41).

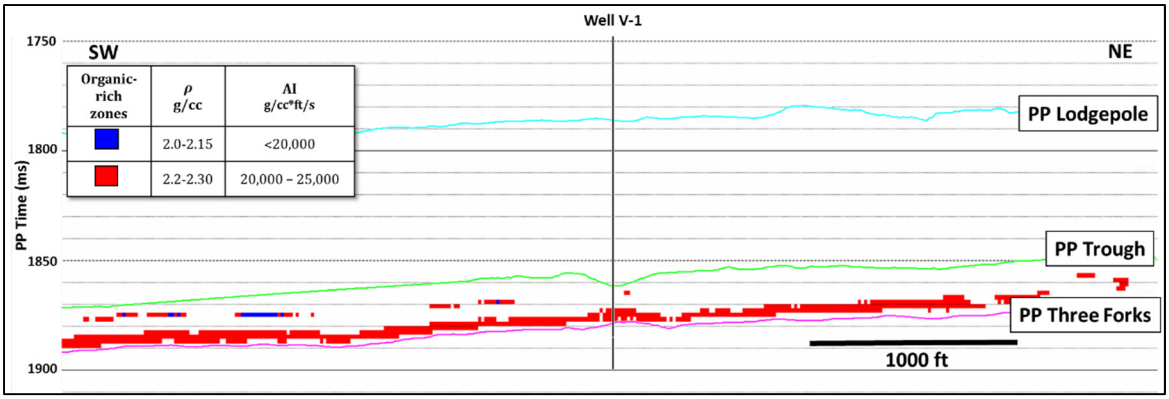

Figure 4.38: Vertical distribution of the two organic-rich zones in the density and acoustic impedance domains. Blue zones are characterized by densities ranging between 2.0 to 2.15 g/cc and acoustic impedance lower than 20,000 g/cc*ft/s ("hot" Upper Bakken). Red zones are defined by densities between 2.2 – 2.3 g/cc and acoustic impedance from 20,000 to 25,000 g/cc*ft/s ("hot" Lower Bakken).

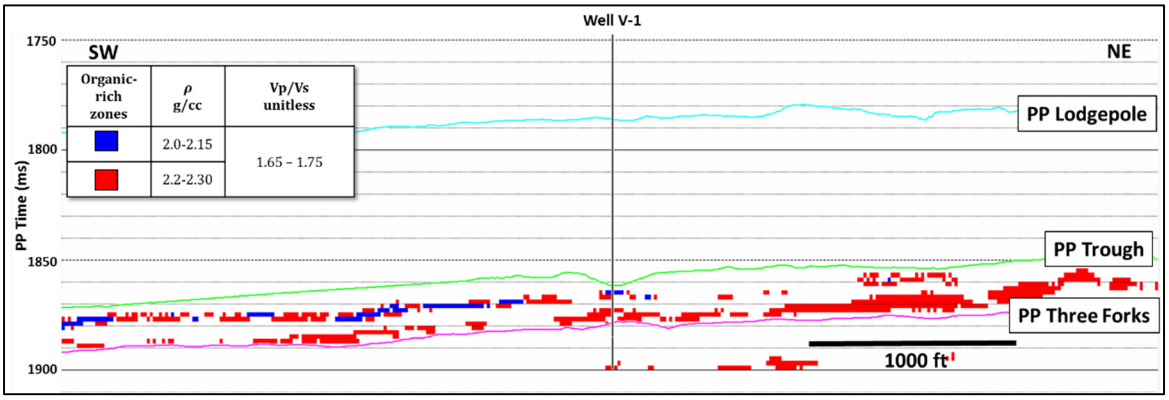

Figure 4.39: Vertical distribution of the two organic-rich zones in the density and Vp/Vs domains. Blue zones are characterized by densities ranging between 2.0 to 2.15 g/cc and Vp/Vs from 1.65 to 1.75 ("hot" Upper Bakken). Red zones are defined by densities between 2.2 – 2.3 g/cc and Vp/Vs from 1.65 to 1.75 ("hot" Lower Bakken).

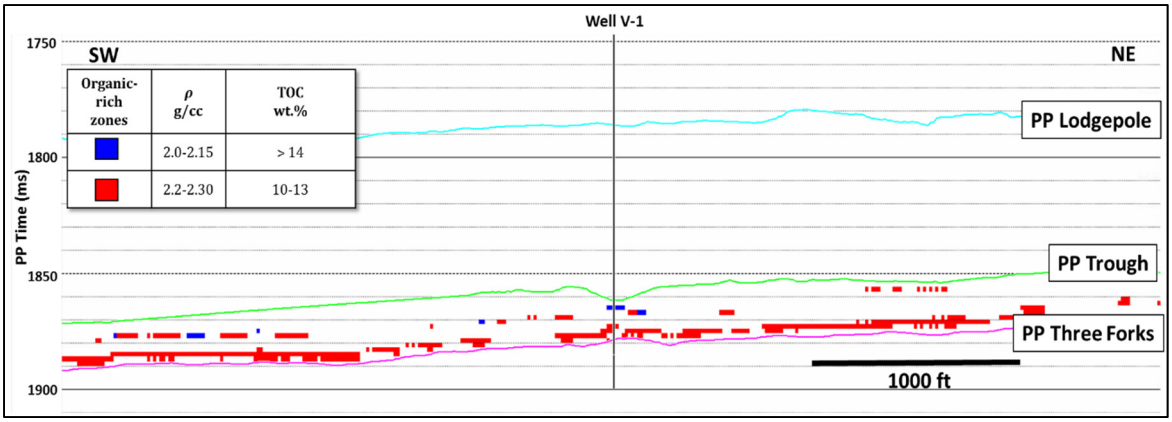

Figure 4.40: Vertical distribution of the two organic-rich zones in the density and TOC content domains. Blue zones are characterized by densities ranging between 2.0 to 2.15 g/cc and TOC greater than 14 wt.% ("hot" Upper Bakken). Red zones are defined by densities between 2.2 – 2.3 g/cc and TOC from 10 to 13 wt.% ("hot" Lower Bakken).

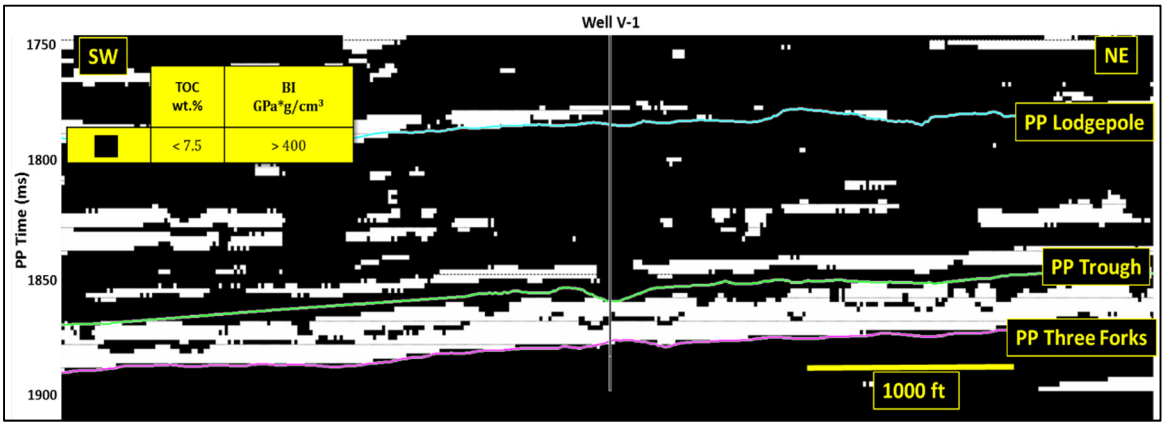

Figure 4.41: Vertical distribution of the low-TOC (< 7.5 wt.%) and high-brittle (> 400 GPa*g/cc) zones (in black).

An additional identification of brittle and ductile facies is carried out by cross-plotting the statistical estimated density vs. brittleness within the Bakken Formation in the 2D line that goes through well V-1. The selection of data points to highlight the

different facies in cross-section is made using cutoffs values of 2.5 g/cc and 400 GPa*g/cc to discriminate the ductile or brittle shales from the rest lithology within the Bakken Formation.

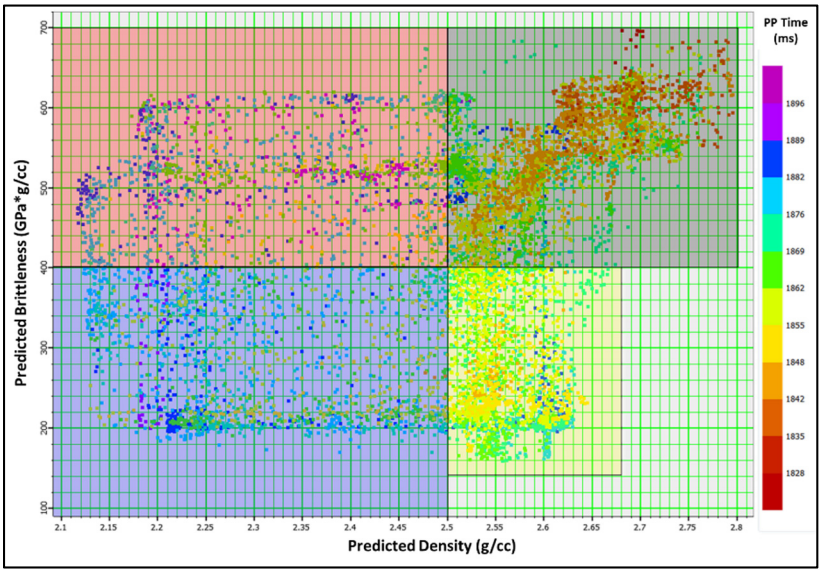

Figure 4.42: Density vs. brittleness cross-plot. The selection of data points to highlight the different facies in cross-section is made using cutoffs values of 2.5 g/cc and 400 GPa*g/cc to discriminate the ductile or brittle shales from the rest lithology within the Bakken Formation.

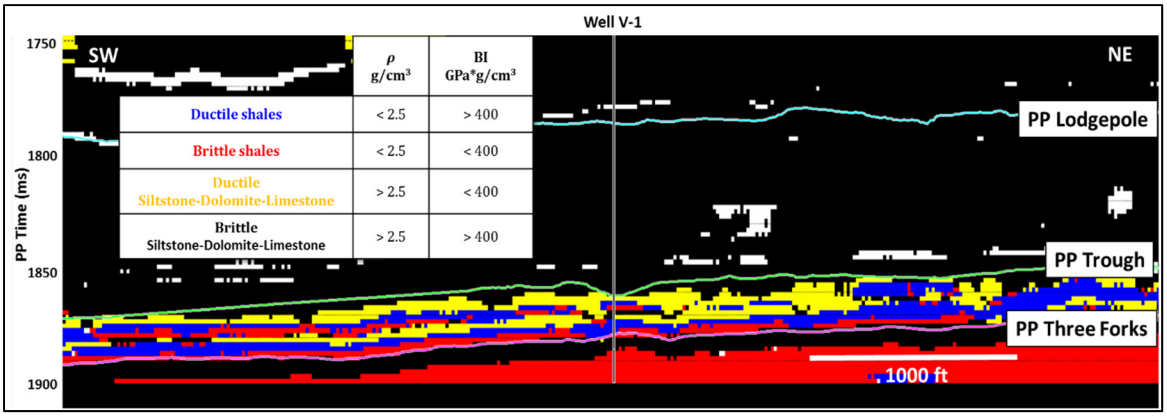

Figure 4.43: Vertical distribution of the brittle facies within the Bakken Formation.

Chapter 5

Conclusions, recommendations, and future work

To understand the relationship between rock properties and their elastic response, petrophysical and rock-physics analysis, seismic modeling, fluid substitution, seismic inversion and multi-attribute analysis are integrated to delimit prospective intervals and areas with high TOC content within the Bakken Formation.

This study draws the following conclusions:

- Shale volume estimated from the normalized corrected GR log can be used as a guide of the relative volume of shale in the formation of interest, and the Vshale calculated from the porosity logs should be interpreted as an underestimation of the shale volume especially in the upper and lower shale members. Vsh_{GRn} and Vsh_{NPHI} are taken as better

representations of the relative volume fraction of shales in the formation of interest (around 60%).

- The crossover between the GR and Rt curves is indicative of the high TOC content in the upper and lower shale members of the Bakken Formation, and the hydrocarbon potential is observed on logs as lower density relative to shale density, high GR response, increased P-wave sonic (DT) relative to shale DT, and increased neutron porosity relative to shale neutron.
- TOC logs are valuable for identifying and quantifying organic richness in the Bakken shale. Schmoker and Hester empirical method, derived from the calculations in 266 wells in the Williston Basin, is considered to be more reliable to define the TOC of the upper and lower shales with 13 and 14 wt.%, respectively in the vicinities of the vertical well V-1 where higher organic-carbon content and a less inert organic matter with better oil-generation potential can be found.
- The siltstones and sandstones of the Middle Bakken member plot toward high Vp/Vs values and the same occurs with the high-velocity carbonates of the Lodgepole and Three Forks Formations. Both Upper and Lower Bakken shales deviate significantly from the background trend and show lower P and S-wave velocities, and hence lower Vp/Vs around 1.6.
- The Lodgepole limestones, Three Forks dolomites, and Middle Bakken siltstones are recognized by their high velocities (> 15,000 ft/s), and organic-matter-rich shales from

Upper and Lower Bakken members can be easily discriminated in the density domain, showing values lower than 2.5 g/cc.

- Rocks with TOC content higher than 10 wt. % deviate from the ones that have lower TOC in the density domain and exhibit slightly lower velocities and lower densities (< 2.3 g/cc) within the Bakken Formation. These high TOC rocks show a generally higher shale content (> 40%). The well V-1 has the highest TOC content within the study area, especially at depths of the Upper Bakken with approximately 50% of clay volume.
- TOC is considered to be the principal factor affecting changes in density P-wave and S-wave velocities in the Bakken shale. Clay content does not appear to influence the elastic properties variations for the Bakken intervals.
- Two "hot" intervals are defined in the Upper and Lower Bakken in terms of TOC content and density. In the "hot" Upper Bakken where TOC is higher than 14 wt.% and density ranges between 2.00 g/cc and 2.15 g/cc, the general clay volume corresponds to values no lower than 0.5. In the "hot" Lower Bakken, TOC is higher 10 wt.%, density ranges between 2.20 g/cc and 2.30 g/cc, and cutoff values or a proportional relation between density and clay volume cannot be defined.
- Low Vp/Vs correlate to both organic-rich and organic-lean shales with high and low clay content. However, the two "hot" units previously defined in terms of TOC content and density show Vp/Vs values between 1.65 - 1.75.
- Acoustic impedance (AI) seems to be a good lithological indicator. The "hot" Upper Bakken AI is lower than the "hot" Lower Bakken AI. These two units can be discriminated

with a cutoff value of approximately 20,000 ft/s*g/cc. In general, the higher the TOC and shale/clay content, the lower the acoustic impedance.

- The domain $E\rho/\nu$ can be used as a brittleness indicator for the Bakken shale members. There are similar trends of increasing brittleness towards the base of the Upper and Lower Bakken but in general, the Lower Bakken is less brittle than the Upper Bakken and the Middle Bakken shows points with moderate brittleness.

- Interval ε, γ and δ estimations from the log data using Havens (2012) approach agree with documented core samples data and VSP processing results for the Bakken shale and allowed to build the log anisotropy model used for studying the AVO seismic modeling in the study area.
- AVA modeling shows that the tops of Upper Bakken, Middle Bakken, Lower Bakken, and Three Forks Formation can be detected with a 45 Hz Ricker wavelet convolved with the respective reflectivity series of the wells. The reflection coefficient decreases because of anisotropic effects, increasing the AVO effect in both the PP and PS synthetic seismograms at depths of Middle Bakken and Three Forks Formations.
- The AVA response picked at the Upper and Lower Bakken troughs (negative amplitude) in the well V-1 shows a negative intercept and a positive gradient caused by a low-impedance rock below a hard cap rock. This anomaly corresponds to an AVO Class IV.
- A full wavelet extraction in the window that includes the reservoir using not only the seismic but the sonic and density logs from the well allows to calculate both, the frequency

and phase spectra and to give an idea about the highest seismic vertical resolution limit. The dominant frequency calculated from the dominant period of the extracted PP full wavelet corresponds to 50 Hz and the resolution limit results around 82 ft indicating that Bakken Formation could be resolved in the PP seismic data. The vertical resolution for the PS data corresponds to approximately 20 ft lower than the PP seismic resolution.

- After the PP-PS joint inversion, the resolution is improved compared to their respective model and the values of P-impedance and Vp/Vs are accurately represented in the inversion for the Lower Bakken member at the vicinity of the vertical well with around 25,000 ft/s*g/cc and 1.71, respectively.
- A comparison between PP and PP-PS joint inversions shows that the P-impedance error decreases by 14% when incorporating the converted-wave information in the inversion process.
- The PP-PS joint inversion computes inverted logs that accurately match the original (filtered) logs. However, the high residual from the synthetic seismograms and the seismic data suggest that the inversion is not completely feasible for using the inverted-density to map the TOC intervals in the Bakken Formation.
- A statistical approach using multi-attribute analysis and neural networks permits to define and delimit zones of interest within the thin members of Upper, Middle, and Lower Bakken. The results show excellent correlations with the original logs. Even though the Upper, Middle and Lower Bakken members are below seismic resolution, the statistical

prediction is picking up the thin intervals with accurate P-impedance, density, TOC content, and brittleness.

- The integration of well log analysis, rock-physics, seismic modeling, constrained inversions and statistical predictions results can contribute in identifying promising reservoir quality areas within the Bakken Formation.

5.1 Recommendations and future work

Proposals for future work are suggested:

- Study the Q attenuation values from the sonic logs.
- Include a statistical multi-parameter estimation for TOC using more well logs.
- Propose a rock-physics model to understand the individual effect of variations in mineralogy, kerogen, and porosity in the rock's elastic response that takes into account anisotropy.
- Study the variations of mineral inclusions with different shale-limestone and shale-dolomite proportions followed by a fluid substitution analysis to evaluate brittleness zones for drilling purposes.
- Since the estimation of elastic properties by means of inversion analysis is data-driven and frequency-dependent, a PP-PS joint inversion using an enhanced PS data with similar frequency content than that of the PP seismic may not merely reduce the residuals but improve the vertical resolution as well. In this case, data from new wells and frequency

enhancements procedures are necessary to better discriminate the Upper, Middle and Lower Bakken by means of the following techniques:

- PP – PS seismic data processing employing Kirchhoff Migration if pre-stack data is available.
- Velocity-based wavelet corrections using non-stationary linear filters that depend on time-variant interval (local) and average (global) velocities (Gaiser and Verm, 2011).
- Geostatistical inversion
- Spectral inversion (bandwidth broadening).

References

Ahmed, U., and Meehan, N., 2016, Unconventional oil and gas resources exploitation and development: Baker Hughes, p. 8.

Alford, E., 2017, Dakota access pipeline to begin operations: webpage accessed: July 2017. <https://bakkenshale.com/bsp-news/dakota-access-pipeline-begins-operations>.

Amogles, 2010, The Bakken: "A non-shale shale play": ConocoPhillips report, August.

Brown, R., and Korringa, J., 1975, On the dependence of the elastic properties of porous rocks on the compressibility of the pore fluid: Geophysics, Vol. 40, No. 4, p. 608-616.

Castagna, J. P., and Swan, H.W., 1997, Principles of AVO crossplotting: The Leading Edge, Society of Exploration Geophysicists, Vol. 17, p. 337-342.

Castagna, J. P., Batzle, M. L., and Eastwood, R. L., 1985, Relationships between compressional-wave and shear-wave velocities in clastic silicate rocks: Geophysics, Vol. 50, p. 571-581.

Charsky, A., and Herron, S., 2013, Accurate, direct Total Organic Carbon (TOC) log from a new advanced geochemical spectroscopy tool: comparison with conventional approaches for TOC estimation: Search and Discovery Article, AAPG Technical Program Expanded Abstracts, No. 41162.

Crain, E. R., and Holgate, D., 2014, A 12-step program to reduce uncertainty inkerogen-rich reservoirs: CSPG-CSEG-CWLS GeoConvention.

Crain, E.R., 2000, Crain's Petrophysical Handbook: webpage accessed: January 2017. <http://www.spec2000.net>.

Crews, C.W., 2015, Relating stratigraphy, lithologic facies, and 3D seismic attributes to oil production in Bakken Formation wells, Red Sky area, Williston Basin, North Dakota: M.S. Thesis, University of Houston.

Du, Y., 2015, Borehole seismic analysis: up and downward continuation, migration velocity updating, and a Bakken shale case history: Ph.D. Dissertation, University of Houston.

Duhailan, M., and Sonnenberg, S., 2014, The curious case of hydrocarbon-expulsion fractures: Genesis and impact on the Bakken Shales. AAPG Search and Discovery article No. 80398.

EIA, 2017, Bakken Region drilling productivity Report: webpage accessed: July 2017. <http://www.eia.gov/petroleum/drilling/pdf/bakken.pdf>.

Ferla, M., and Milluzzo, V., 2014, New frontier for the seismic inversion: five reasons for the anisotropic approach: 84th Annual International Meeting, SEG, Expanded Abstracts, p. 3190-3194.

Fomel, S. and Backus, M.M., 2003, Multicomponent seismic data registration by least squares: 73rd SEG Annual Meeting, Expanded Abstract, Vol. 22, p. 781-784.

Gaiser, J.E., 1996, Multicomponent VP/VS correlation analysis: Geophysics, Vol. 61, p. 1137-1149.

Gaiser, J. and Verm, R., 2011, Velocity-based wavelet corrections for domain transformation: 73rd EAGE Conference & Exhibition incorporating SPE EUROPEC.

Garotta, R. and Granger, P.Y., 1988, Acquisition and processing of 3Cx3D data using converted waves: 58th SEG Annual Meeting, Expanded Abstract, Vol. 7, p. 995-998.

Gaswirth, S., Marra, K., Cook, T., Charpentier, R., Gautier, D., Higley, D., and Whidden, K., 2013, Assessment of undiscovered oil resources in the Bakken and Three Forks Formations, Williston Basin Province, Montana, North Dakota, and South Dakota: U.S. Geological Survey fact sheet, No. 3013, p. 4.

Gerhard, L. C., Anderson, S.B., and Fischer, D.W., 1990, Petroleum geology of the Williston Basin: Interior cratonic basins: AAPG Memoir, Vol. 51, p. 507-559.

Greenberg, M. L., and Castagna J. P., 1992, Shear-wave velocity estimation in porous rocks: Theoretical formulation, preliminary verification and application: Geophysical Prospecting, Vol. 40, p. 195–209.

Grover, P. W., 1996, Stratigraphy and diagenesis of the Mississippian Bakken Shale-Lodgepole Limestone sequence, Williston Basin, North Dakota: Ph.D. dissertation, Texas A&M University.

Hampson-Russell, 2014, User manual. Hampson-Russell software services limited, e-book.

Hampson, D., and Russell, B., 2013, Joint simultaneous inversion of PP and PS angle gathers: CSEG RECORDER, Vol. 38, p. 32-39.

Han, D.-H., Liu, J., and Sun, M., 2014, Velocity model development for heavy oils: SEG Technical Program Expanded Abstracts.

Havens, J., 2012, Mechanical properties of the Bakken Formation: M.S. Thesis, Colorado School of Mines.

Heslop, K.A., 2010, Generalized method for the estimation of TOC from GR and Rt: Search and Discovery Article, AAPG Technical Program Expanded Abstracts, No. 80117.

Huang, L., 2016, Estimating seismic anisotropy: fluid substitution theory, 3D-printed inclusion models, and multi-component 3D VSP in the Bakken shale: Ph.D. Dissertation, University of Houston.

KED Interests LLC, 2017, Bakken Shale news, market place, jobs: webpage accessed: July 2017. <https://bakkenshale.com/>.

LeFever, J. A., Martiniuk, C. D., Dancsok, E. F., and Mahnic, P.A., 1991, Petroleum potential of the middle member, Bakken Formation, Williston Basin: Sixth International Williston Basin Symposium.

Meissner, F.F., 1991, Petroleum geology of the Bakken Formation Williston Basin, North Dakota and Montana: MSG Guidebook to Geology and Horizontal Drilling of the Bakken Formation, p. 19-42.

Omoboya, O.K., 2015, Integrated anisotropy analysis of the Bakken shale: physical modeling and wide azimuth attribute analysis in the Williston Basin: Ph.D. Dissertation, University of Houston.

Passey, Q. R., Creaney, S., Kulla, J.B., Moretti, F.J., and Stroud, J.D., 1990, A practical model for organic richness from porosity and resistivity logs: AAPG Bulletin, Vol. 74, p. 1777-1794.

Passey, Q., Bohacs, K., Esch, W., Klimentidis, R., and Sinha, S., 2010, From Oil-Prone Source Rock to Gas-Producing Shale Reservoir - Geologic and Petrophysical Characterization of Unconventional Shale-Gas Reservoirs: SPE No. 131350, CPS/SPE International Oil & Gas Conference and Exhibition, Beijing, China, June 8-10.

Perez, R., and Marfurt, K., 2013, Brittleness estimation from seismic measurements in unconventional reservoirs: Application to the Barnett Shale: SEG Technical Program Expanded Abstracts, p. 2258-2263.

Pitman, J. K., Price, L. C., and LeFever, J. A., 2001, Diagenesis and fracture development in the Bakken Formation, Williston Basin: Implications for reservoir quality in the middle member: U.S. Geological Survey Professional Paper No. 1653.

Pollastro, R.M., Roberts, L.N.R., and Cook, T.A., 2011, Geologic assessment of technically recoverable oil in the Devonian and Mississippian Bakken Formation, chap. 5 *of* U.S. Geological Survey Williston Basin Province Assessment Team, Assessment of undiscovered oil and gas resources of the Williston Basin Province of North Dakota, Montana, and South Dakota, 2010: U.S. Geological Survey Digital Data Series DDS–69–W, p. 34.

Prasad, M., and Zargari, S., 2014, Porosity evolution in oil-prone source rocks: SEG Annual Meeting Conference.

Rickman, R., Mullen, M., Petre, E., Grieser, B., and Kundert, D., 2008, A practical use of shale petrophysics for stimulation design optimization: All shale plays are not clones of the Barnett shale: SPE Annual Technical Conference and Exhibition, No. 115258 p. 21-24.

Ruger, A., 2002, Reflection coefficients and azimuthal AVO Analysis in anisotropic media: SEG Geophysical Monograph Series, No. 10.

Ruiz, F., 2016, Rock-physics and 3C-3D seismic analysis for reservoir characterization: Marcellus shale, Pennsylvania: M.S. Thesis, University of Houston.

Russell, B., 2014, Prestack seismic amplitude analysis: An integrated overview: Interpretation, Vol. 2, No. 2, p. 19-36.

Russell, B., 2014, Guide to Emerge: Hampson-Russell software services limited.

Russell, B., and Hampson, D., 1999, AVO theory: Hampson-Russell software services limited, p. 69.

Russell, B., Hampson, D., Hirsche, K., and Peron, J., 2005, Joint simultaneous inversion of PP and PS angle gathers: Crewes Research Report, Vol. 17, p. 1-14.

Sarg, J.F., 2012, The Bakken – An unconventional petroleum and reservoir system: Final scientific/Technical report, Colorado School of Mines.

Savic, M., VerWest, B., Masters, R., Sena, A. and Gringrich, D., 2000, Elastic Impedance Inversion in Practice: SEG Expanded Abstracts.

Sayers, C. M., 2013, The effect of kerogen of the AVO response of organic-rich shales: The Leading Edge, Vol. 32, No. 12, p. 1514-1519.

Schmoker, J., 1979, Determination of Organic Content of Appalachian Devonian Shales from Formation-Density Logs: AAPG Bulletin, Vol. 63, No. 9, p. 1504-1537.

Schmoker, J.W., 1981, Determination of organic-matter content of Appalachian Devonian shales from gamma-ray logs: AAPG Bulletin, Vol. 65, p. 1285-1298.

Schmoker, J.W., and Hester, T.C., 1983, Organic carbon in Bakken Formation, United States portion of Williston Basin: AAPG Bulletin, Vol. 67, No. 12, p. 2165-2174.

Sharma, K. R., and Chopra, S., 2015, Determination of lithology and brittleness of rocks with a new attribute: The Leading Edge, Vol. 34, No. 5, p. 554.

Sorensen, J., Schmidt, S., Smith, S., Bailey, T., Mibeck, B., Harju, J., 2008, Final Report, in J. Terneus (project manager), Evaluation of key factors affecting successful oil production in the Bakken Formation, North Dakota: Prepared for the U. S. Department of Energy, 61 p.

Thomsen, L., 1986, Weak elastic anisotropy: Geophysics, Vol. 51, No. 10, p. 1954-1966.

Tsvankin, I., 2001, Seismic signatures and analysis of reflection data in anisotropic media: Elsevier Science.

Tsvankin, I., and Thomsen, L., 1994, Nonhyperbolic reflection moveout in anisotropic media: Geophysics, Vol. 59, p. 1290-1304.

Vernik, L., and Khadeeva, Y., 2013, Rock physics of organic shale and its implications: GeoConvention: Integration.

Vernik, L., and Landis, C., 1996, Elastic anisotropy of source rocks: implications for hydrocarbon generation and primary migration: AAPG Bulletin, Vol. 80, No. 4, p. 531-544.

Vernik, L., and Liu, X., 1997, Velocity anisotropy in shales: A petrophysical study: Geophysics, Vol. 62, No. 2, p. 521-532.

Vernik, L., and Nur, A., 1992, Ultrasonic velocity and anisotropy of hydrocarbon source rocks: Geophysics, Vol. 57, No. 5, p. 727-735.

Widess, M.B., 1973, How thin is a thin bed?: Geophysics, Vol. 38, p. 1176-1180.

Wild, P., 2011, Practical applications of seismic anisotropy: First Break, Vol. 29, p. 117-124.

Wiley, C., Barree, B., Eberhard, M., and Lantz, T., 2004, Improved horizontal well stimulations in the Bakken Formation, Williston Basin, Montana: Society of Petroleum Engineers annual technical conference and exhibition, SPE article, No. 90697.

Yang, Y., and Zoback, M.D., 2014, The role of preexisting fractures and faults during multistage hydraulic fracturing in the Bakken Formation: Interpretation, Vol. 2, p. SG25-SG39.

Yenugu, M., and Han, D.-H., 2013, Seismic characterization of kerogen maturity: An example from Bakken shale: SEG Technical Program Expanded Abstracts.

Zhu, J., Lovell, M., and Skidmore, C., 2016, Prestack seismic inversion in presence of anisotropic unconventional reservoirs: 86th Annual International Meeting, SEG Expanded Abstracts, p. 3533-3537.